AN ANALYTICAL, NUMERICAL, AND EXPERIMENTAL STUDY OF AUTOMATED DAMAGE ASSESSMENT FOR CONCRETE STRUCTURES

BY

SANGGOO KANG

DISSERTATION

Presented to the Faculty of the Graduate School of

The University of Texas at Arlington

in Partial Fulfillment of the Requirements

for the Degree of Doctor of Philosophy

THE UNIVERSITY OF TEXAS AT ARLINGTON

May 2021

ABSTRACT

This dissertation presents the automated damage assessment studies for concrete structure. Three major studies are performed to: 1) understand the theoretical wave scattering model to evaluate the internal vertical crack, 2) to validate the theoretical wave scattering model through FE simulations with experimental measurements, and 3) to advance practical automated crack evaluation (ACE) system for vertical crack and delamination detection.

Firstly, singular integral solutions are studied to investigate scattering of Rayleigh waves by subsurface cracks. Defining a wave scattering model by objects, such as cracks, still can be quite a challenge. The model's analytical solution uses five different numerical integration methods: (1) the Gauss–Legendre quadrature, (2) the Gauss–Chebyshev quadrature, (3) the Gauss–Jacobi quadrature, (4) the Gauss–Hermite quadrature and (5) the Gauss–Laguerre quadrature. The study also provides an efficient dynamic finite element analysis to demonstrate the viability of the wave scattering model with an optimized model configuration for wave separation. The obtained analytical solutions are verified with displacement variation curves from the computational simulation by defining the correlation of the results. A novel, verified model, is proposed to provide variations in the backward and forward scattered surface wave displacements calculated by different frequencies and geometrical crack parameters. The analytical model can be solved by the Gauss–Legendre quadrature method, which shows the significantly correlated displacement variation with the FE simulation result. Ultimately, the reliable analytic model can provide an efficient approach to solving the parametric relationship of wave scattering.

Secondly, the analytical model of internal vertical crack is validated through comparison with parametric studies based on dynamic finite element (FE) simulations and experimental measurement. The results of the study allow to demonstrate crack depth estimation understanding response variation curves, which are the wave response ratio of scattering waves to incident waves according to specific wave frequency and

crack geometry. In addition, the study advances the crack evaluation based on the SWS-IVC model leveraging relative wave energy attenuation obtained from arrayed air-coupled MEMS sensors.

Finally, the ACE system is proposed, developed and demonstrated for the rapid bridge deck inspection. The inspection includes detection of delamination, vertical crack, and corroded reinforcement by using flexural vibration mode of impact-echo testing, wave attenuation, and GPR, respectively. The ACE system has novelty in three main techniques: the advanced auto-impacting system, high-speed integrated scanning platform, and high-resolution data collecting system. The advanced auto-impacting system is validated through laboratory tests considering many parameters. Two field bridge inspection are performed with the developed ACE system. The 2-D interpolation colormaps present area of the delamination, vertical crack, and reinforcement corrosion.

ACKNOWLEDGEMENTS

Firstly, I would like to thank my advisor, Dr. Suyun Ham, for his support. I am honored to be his student for my lifetime, and I feel privileged to work with him in many projects, courses, and research, which provided invaluable experience. Without his supporting and mentoring, this study would not have been possible.

I also want to thank the committee members, Dr. Shih-ho Chao, Dr. Stefan A. Romanoschi, and Dr. Jay Rosenberger, for serving as my committee members and providing valuable feedback that has helped to shape this dissertation.

Finally, I would like to thank my parents for their continuous encouragement throughout my life. Last but not least, I wish to thank my wife, Yunjung Han, for her extraordinary effort and love during our six years at the University of Texas at Arlington.

TABLE OF CONTENTS

LIST OF FIGURES

LIST OF TABLES

CHAPTER 1 INTRODUCTION

1.1 Problem Statement

Concrete is the most widely used construction material due to its advantages such as low cost, considerable strength, and versatility. However, the deterioration in concrete is caused by a variety of environmental factors (e.g., freeze-thaw cycle, chemicals, abrasion, erosion). These damages also occur over time through different mechanisms through hydraulic and thermal shrinkage, swelling, deformation, and external load. In particular, cracks are typical and critical damages caused by several factors, including structural deformation or external load. Consequently, extensive damages result in degradation of material property, corrosion of reinforcement, and even structural failure. Thus, effective detection and evaluation of concrete cracks is required in a timely manner to better predict service life and monitor structural conditions at an early stage.

1.2 Objectives and Approach

The purpose of this study is to understand a theoretical wave scattering model to evaluate the internal vertical crack and to develop the crack evaluation system for crack detection. Two types of concrete crack are considered: vertical crack and internal horizontal crack. The internal horizontal crack is called as delamination. Several studies are performed for different objectives.

Study 1 is performed to understand the theoretical wave scattering model to evaluate the internal vertical crack. In Chapter 2, the analytical surface wave scattering model and finite element (FE) simulations are introduced. The study of an analytical model and FE simulation is to understand the surface wave scattering theory and verify the model with multiple FE simulations.

Study 2 is performed to verify the theoretical wave scattering model and FE simulation with the laboratory experiments. In Chapter 3, an analytical model, FE simulation, and experiments are introduced. Finally, Study 2 proposes the crack evaluation method using the response variation curve and energy attenuation method.

Study 3 is performed to develop the ACE system for vertical crack and delamination detection. The system is designed to inspect the flat concrete structure such as concrete slab or bridge deck. The ACE system uses impact-echo testing and wave attenuation to detect delamination and vertical crack.

CHAPTER 2 BACKGROUND

2.1 Chapter Overview

This chapter presents fundamental backgrounds to understand the studies performed in this dissertation. General concrete defects and fundamental theory of wave propagation are described. The section of wave propagation includes typical nondestructive testing (NDT) methods to identify and evaluate the concrete damages.

2.2 Concrete Defects

The typical concrete cracks can be classified by direction and location. Internal vertical crack, surface-opening crack, and delamination, which is an internal horizontal crack, can be considered as the critical types of concrete crack as described in Figure 2.1. This section will introduce the fundamental background of concrete crack and delamination.

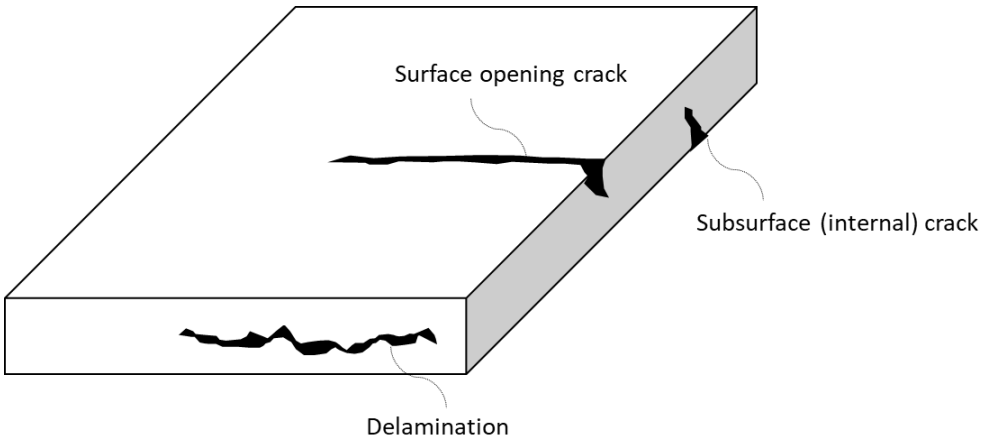

Figure 2.1. Typical cracks of concrete. Two types of vertical crack and delamination are the most critical crack for the concrete structure.

2.2.1 *Cracks*

Concrete is extensively used in construction material due to its high compressive strength but typically low tensile strength; therefore, a common design assumption is to neglect concrete tension strength outright. The low tensile strength of concrete leads to cracking. The cracking in reinforced concrete structures occurs when the tensile stresses due to internal or external effects exceed the concrete tensile strength. According to ACI committee 224, cracking can be classified into two main categories based on the time of crack occurrence: cracks occurring before concrete hardening or after concrete hardening (Committee 224 ACI 2007). In general, it is also acceptable classifications by concrete cracking causes, for example, structural cracks including flexural, shear, and internal micro cracking, or non-structural cracks, which are the result of the intrinsic properties of concrete and its ingredients.

2.2.2 *Delamination*

The most severe problem of slab-like reinforced concrete (e.g., bridge deck and slab) is delamination, mainly caused by corroded steel reinforcements. Generally, the corrosion of steel reinforcement in bridge decks is caused by penetrated chloride ions, moisture, oxygen, and temperature. The formation of the

corrosion products causes volume expansion of the reinforcement. Eventually, the delamination is formed by the tensile stresses induced by the expansion of corroded reinforcements. In addition, the produced delamination causes the additional vertical cracks from the delamination to rise to the surface. As the number of vertical cracks increases, the corrosion process accelerates. The further degradation (e.g., potholes) can be caused by these negative interactions between delamination, vertical crack, and reinforcement corrosion with external factors (e.g., traffic load, freeze-thaw cycle) (Hendricks et al. 2020). The produced degradations (e.g., potholes) due to delaminations are critical for the roadway safety and the service life of bridge decks (Tsai and Chatterjee 2018).

Figure 2.2. Delamination and spalling in a reinforced concrete wall (Harrer and Gaudette 2019).

2.3 Wave Theory and Nondestructive Testing

This section presents a fundamental theory of elastic wave propagation in elastic medium and NDT methods. Since the NDT methods use the propagated wave responses (e.g., amplitude, velocity, spectral magnitude), understanding the fundamental of wave propagation will be helpful to understand the studies performed in this dissertation.

2.3.1 *Wave Propagation*

In this section, fundamental wave propagation of stress waves in an elastic medium is introduced for understanding stress wave behaviors. The stress wave is classified to the body wave and surface wave. The body waves, P-wave (longitudinal wave) and S-wave (shear or transverse wave) travel into the medium. The wave velocities depend on the material property (mass density and elastic constants) of the propagating medium. The surface wave, known as a Rayleigh wave, travels along the surface of the medium with the motion amplitude decreasing rapidly with depth (effective depth of penetration). The polarization of Rayleigh waves lies in a plane perpendicular to the surface. The effective depth of penetration is less than a wavelength (Giurgiutiu 2012). Figure 2.3 depicts the different types of wave occurred from the single excitation source on the interface of two medium. The leaky wave can be generated from a fluid-solid interface to the fluid medium.

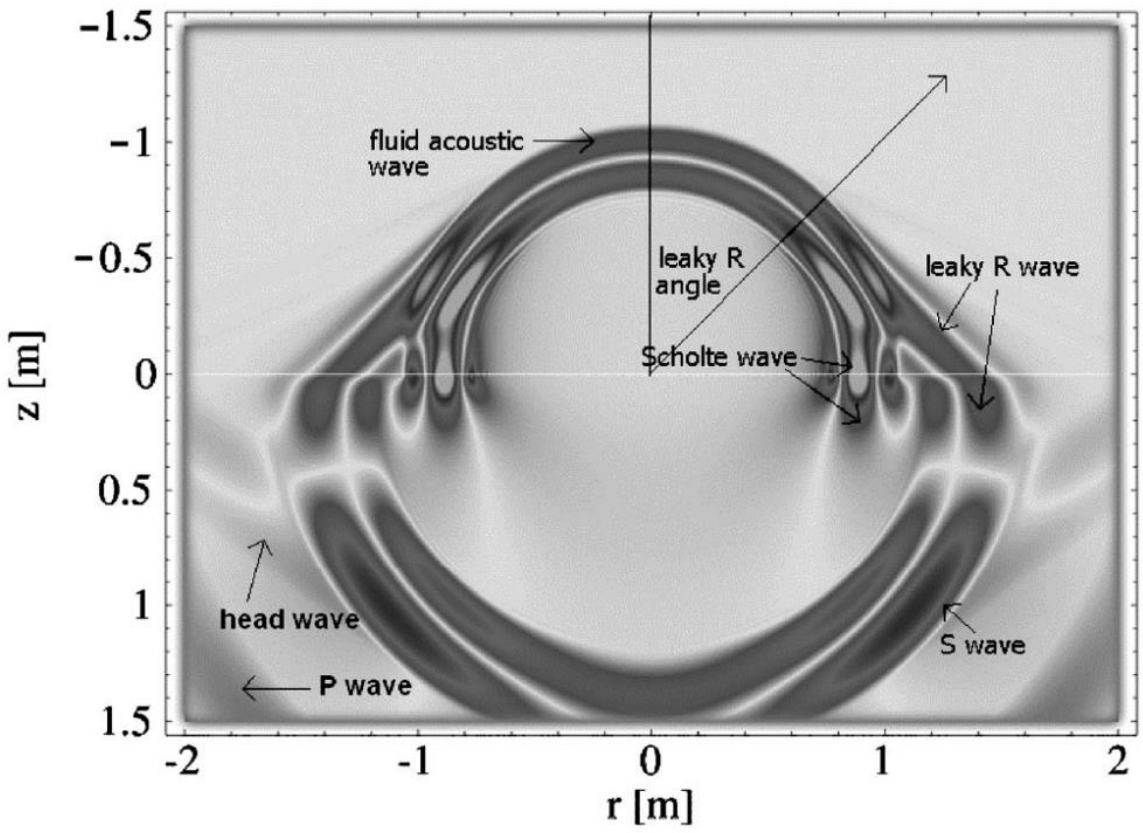

Figure 2.3. Detailed image of wave propagation from the excitation source (Zhu et al. 2004). P-wave, S-wave, surface wave (R wave), and leaky surface wave are shown in the single excitation source on the interface of two mediums (different material property)

2.3.2 *Wave Attenuation*

When a wave travels through a medium, its intensity diminishes with distance. In idealized materials, the wave amplitude is only reduced by the spreading of the wave. General materials, however, all produce an effect that further weakens the wave. This further weakening results from scattering and absorption. Scattering is the reflection of the wave in directions other than its original direction of propagation. Absorption is the conversion of the wave energy to other forms of energy. The combined effect of scattering and absorption is called attenuation.

In the following studies, wave scattering and attenuation will be used to evaluate and detect the vertical crack.

2.3.3 ***Impact-Echo***

Generally, an impact-echo test is used to detect delamination using two different analyses with thickness and flexural vibration modes. The thickness mode (f_{TM}) is normally dominated when body waves are reflected between the two parallel boundaries. Normally, thickness mode is used to estimate the thickness (h) of the medium with known longitudinal wave velocity (C_L). In the impact-echo test, the thickness is,

$$h = \beta_1 C_L / 2 f_{TM}, \quad (2.1)$$

where $\beta_1$is correction factor (Sansalone and Streett 1997).

Figure 2.4 shows the schematic testing configuration of the impact-echo method and frequency responses. Two frequency-domain graphs show the thickness mode of frequency components at 3.42 kHz and 7.32 kHz (note the Figure 2.4 (c) shows the thickness mode vibration with 0.25 m of thickness, not the flexural vibration mode)

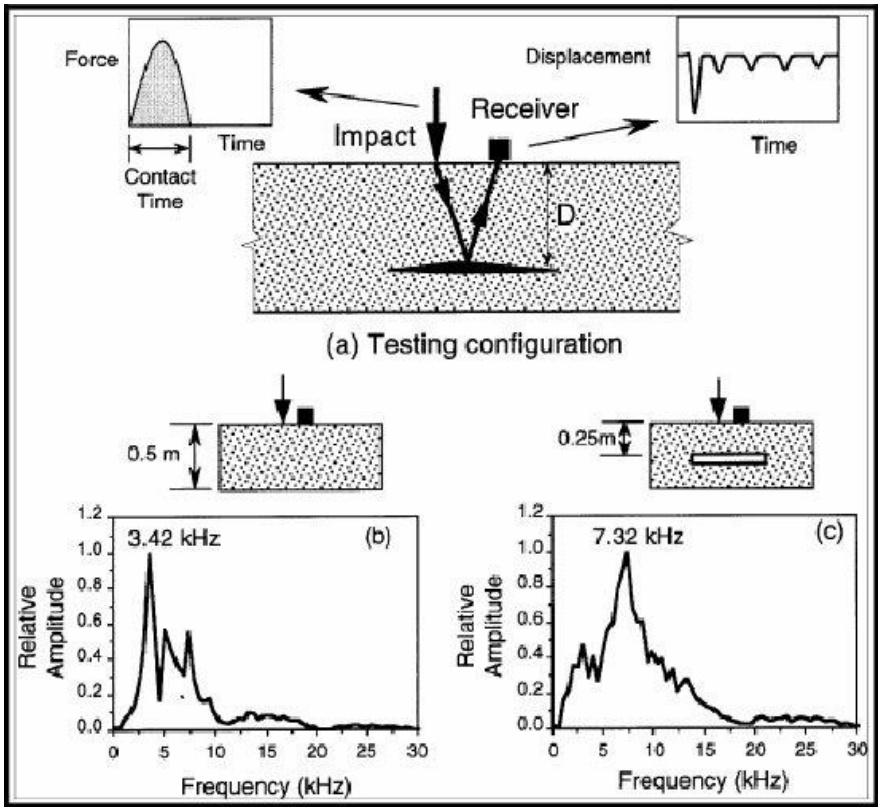

Figure 2.4. Schematic of an impact-echo method, (b) amplitude spectrum for a test of a solid wall; and (c) amplitude spectrum for test over the void in the wall (Medak et al. 2019)

On the other hand, the flexural vibration modes are normally detected when the impact-echo test is performed over the delamination. These flexural vibration modes occur by the out-of-plane vibration of the concrete above delamination. The fundamental flexural vibration mode (f_{FM}) of rectangular delamination can be expressed (Leissa 1973):

$$f_{FM} = \frac{k_{DF}^2 \pi}{2h^2} \sqrt{\frac{D}{\rho h}} \qquad (2.2)$$

where k_{DF} is a dimensionless frequency which is determined from the general natural frequencies in terms of the width-to-depth ratio of delamination; D is flexural rigidity, $D = Eh^3/12(1-\nu^2)$, with Young's modulus (E) and Poisson's ratio (ν), ρ is material density.

Figure 2.5 shows full-thickness mode, flexural vibration mode by the bottom reinforcement layer delamination, and flexural vibration mode by the top reinforcement layer delamination. The only top reinforcement layer delamination (shallow delamination) shows the flexural vibration mode.

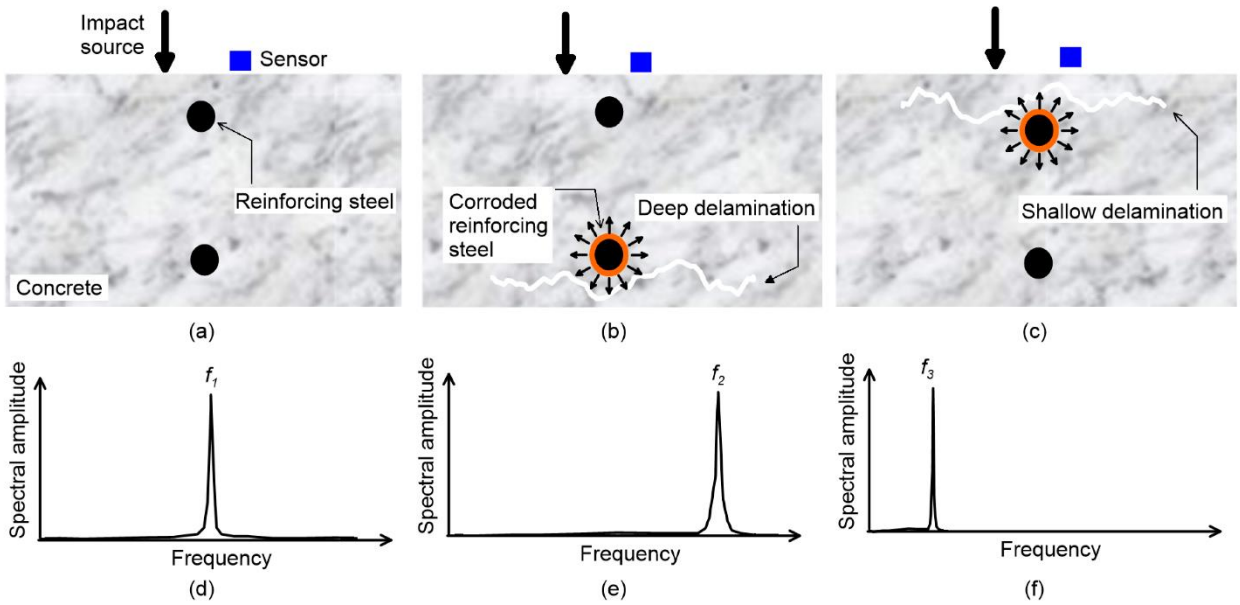

Figure 2.5. Typical source-and-receiver configuration and frequency signals of Impact-echo testing for condition assessment of concrete with delamination defects of various depths: the first column (a,d) represents solid (crack-free) concrete plates; and the second (b,e) and third (c,f) columns represent concrete plates with relatively deep and shallow delamination defects, respectively (Kee et al. 2020)

CHAPTER 3 ANALYTICAL WAVE SCATTERING MODEL

3.1 Motivation

The propagation of disturbances known as wave propagation in solids has been studied in many physical science and engineering branches. Wave propagation carries energy (e.g., kinetic and potential energies) through a solid medium, and energy transmission over a radiation pattern is through the motion of particles in the wave motion phenomenon. Although the wave motion in elastic solids is well-studied, adequately defining a wave scattering model by objects, such as cracks, can still be quite a challenge.

Over the past decades, crack evaluations using a wave scattering approach in nondestructive evaluations (NDEs) have gained much attention (Ham and Popovics 2015a; b). Many researchers in the early 1980s offered analytical solutions to define and explain the scattered surface waves caused by cracks (e.g., subsurface crack) (Achenbach et al. 1981, 1983; Achenbach and Brind 1981). The vertical sub-surface crack can cause a scattered field since the crack is one of the most influential damages of surface wave propagation. The analytical model of a vertical subsurface crack (Achenbach and Brind 1981) is obtained by establishing an integral representation for the scattered field expressed in terms of the fundamental potentials first introduced by Lapwood (Lapwood 1949). Furthermore, numerical methods have been devised to solve the singular integral equations of the analytical model. For example, the Gauss-Chebyshev quadrature rule as a numerical method was adopted by Erdogan and Gupta (Erdogan et al. 1973). Understanding the numerical solution of a singular integration is vital to providing an accurate and reliable solution to the analytical wave scattering model. Such studies have focused on scattered wave motions presented in relation to the displacement variations caused by different frequencies and geometrical crack parameters. Based on this approach, a well-defined relationship can be developed to evaluate causes and estimate behavioral patterns in cracks. Although using the relationship between displacement variations and frequencies can lead to evaluate cracks by solving the inverse problem, research is needed to verify displacement variations in the existing analytical solutions.

Meanwhile, high-performance computers and simulation software has facilitated efficient wave modeling studies [6, 7], which perform with experimental studies under the constraints of time, environment, sources, etc. Several methods have been conducted to simulate mechanical wave propagation in solid mediums. Among them, the finite element (FE) simulation is widely used for higher accuracy and adaptability. Hassan and Veronesi (Hassan and Veronesi 2003) performed a comparative study of the FE simulation of wave propagation and laser interferometry experiment with a cracked steel plate to show the reliability of FE simulation. The FE results allow simulation of waveform change between the incident wave and scattered wave based on the resultant crack(s). One challenge of the FE simulation of wave propagation is that it requires a large-sized simulation model to avoid wave reflection at the model's boundary.

Furthermore, the model should have enough distance between the wave source and listening nodes to obtain pure waveforms (e.g., surface wave). Typically, a minimized model has been designed to streamline computational efficiency. Oh et al. in 2012 conducted practical FE simulations using a damper and energy-absorbing element known as an infinite element to minimize the model size. They proposed a combination of damper and infinite element with a required absorbing thickness and damping factor, so dampers could prevent wave reflection.

Both analytical and simulation methods (e.g., FE) are powerful approaches for wave modeling, aiming to predict or provide a specific parametric relationship in a system (e.g., variations of a scattered wave amplitude by different frequencies and crack sizes). The simulation method is beneficial when a complex wave model is needed (e.g., complicated geometry and various incident waves). In addition, an analytical model has applicability limitations needing corrections of some factors (e.g., nonlinearity, wave amplitude-dependent) (Karathanasopoulos et al., 2019; Reda et al., 2018). However, an analytical method is still a powerful approach to calculate the wave model needs rapidity to provide computational efficiency. This is especially true when the simulation model has become too time-consuming and requires heavy computations. Thus, a reliable analytical model can significantly save efforts and provide an efficient approach to solving the parametric relationship of wave scattering. Furthermore, beyond the computational

benefit, an analytical method helps understand the fundamental wave propagation through a mathematical formulation derived from wave motion and elastodynamic theory (Pao and Chen 2009).

This study investigates the existing analytical model of the displacement variations of scattered surface waves and studies different numerical integration methods for the proposed analytical model. We also introduce an efficient dynamic FE analysis to demonstrate the viability of the wave scattering model with an optimized model configuration for wave separation. Finally, we verify the analytical model with the FE simulation results uniquely. To solve the singular integral equations in the analytical model, five different numerical integration methods of Gaussian quadrature are considered: the Legendre quadrature (GLEQ), the Gauss-Chebyshev quadrature (GCQ), the Gauss-Jacobi quadrature (GJQ), the Gauss-Hermite quadrature (GHQ), and the Gauss-Laguerre quadrature (GLAQ). The obtained displacement variation curves from the analytical models are compared and verified with FE simulation results by defining the correlation of the curves.

3.2 Analytical model

The analytical model of the wave scattering will be defined in this section. The aim of the theoretical study is to calculate the displacement variation subject to the crack geometry and incident wave frequencies in a homogeneous, isotropic, and linearly elastic solid medium on the half-plane condition defined as the set of points (x, y) in the Cartesian plane with $y \geq 0$. The sub-surface crack is formed, as shown in Figure 3.1, with varying a and b parameters.

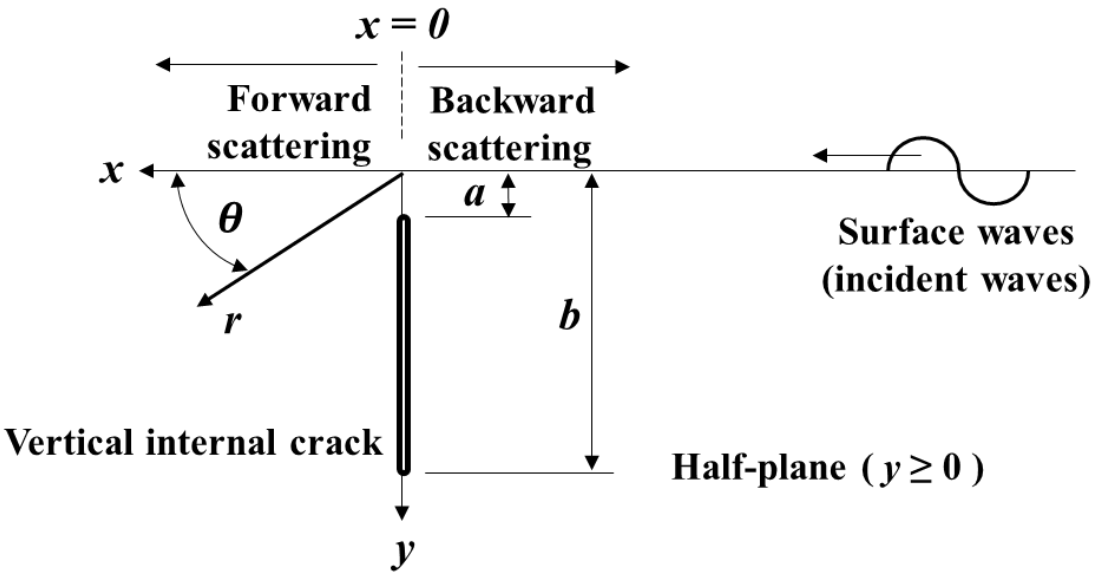

Figure 3.1 Illustration of sub-surface crack on the two-dimensional x-y half-plane. "a" is the distance between the ground and the top of the crack tip, b is the distance between the ground and the bottom of the crack tip, and r and θ are components of the polar coordinate. The image shows the directions of the incident waves and scattered waves influenced by different a and b distances.

3.2.1 *Derivation of displacement potentials*

The displacement field as the final theoretical model can be expressed as two potential functions, a scalar potential $\varphi(x, y)$ and a vector potential $\psi(x, y)$ by Helmholtz decomposition (Farwig et al. 2007):

$$\boldsymbol{u} = \boldsymbol{\nabla}\varphi + \boldsymbol{\nabla} \times \psi, \tag{3.1}$$

where $\boldsymbol{u}$ is the displacement field of scattered waves and $\boldsymbol{\nabla}$ is the Nabla or Del operator. Computing the displacement potentials is the main part of defining the theoretical scattering model. The displacement field is defined in the z-invariant condition. The waves in the half-plane are z-invariant waves where all functions are dependent on the z-direction. The displacement potentials are defined in the scattered field and satisfy a radiation condition of the elliptic boundary-value problem by Wickham (Wickham 1977) as the equation including the exponential and small 'o' functions:

$$\varphi = A_{\pm} e^{\pm i k_R x - \left(k_R{}^2 - k_L{}^2\right)^{1/2} y} + A(\theta)(k_L r)^{-\frac{1}{2}} e^{i k_L r} + o\left((k_L r)^{-1/2}\right),$$
$$\psi = B_{\pm} e^{\pm i k_R x - (k_R{}^2 - k_T{}^2)^{1/2} y} + B(\theta)(k_T r)^{-\frac{1}{2}} e^{i k_L r} + o((k_T r)^{-1/2}), \quad (3.2)$$

where A and B are constant; k_R, k_L, and k_T are the Rayleigh wavenumbers, longitudinal waves, and transverse waves, respectively. r and θ are the components of the polar coordinate (r, θ). The $\pm$ signs denote forward direction, +, and backward direction, $-$. The part including the polar coordinate in Eq. (3.2) is ignored since the incident wave angle is 90 degrees. The coefficient A and B satisfy the equation and are given as:

$$A_+/B_+ = -A_-/B_- = \left(2k_R{}^2 - k_T{}^2\right)/2ik_R(k_R{}^2 - k_L{}^2)^{1/2}. \quad (3.3)$$

The constant B can be obtained by Eq. (3.3)) when the constant A can be calculated as an explicit formula given Achenbach's approach (Gregory 1975), which can be expressed as:

$$A_{\pm} = \frac{\left(2k_R{}^2 - k_T{}^2\right)^2 k_R}{2k_T{}^2 S} \int_a^b dy \left\{\pm d_y(y) R(y) + i d_x(y) Q(y)\right\}, \quad (3.4)$$

where

$$R(y) = 2k_R \left\{ e^{-\left(k_R{}^2 - k_L{}^2\right)^{1/2} y} \left(k_R{}^2 - k_T{}^2\right)^{1/2} - e^{-\left(k_R{}^2 - k_T{}^2\right)^{1/2} y} \left(k_R{}^2 - k_L{}^2\right)^{1/2} \right\}, \quad (3.5)$$

$$Q(y) = e^{-\left(k_R{}^2 - k_L{}^2\right)^{1/2}} \frac{\left(2k_R{}^2 - 2k_L{}^2 + k_T{}^2\right)\left(k_R{}^2 - k_T{}^2\right)^{1/2}}{\left(k_R{}^2 - k_L{}^2\right)^{1/2}} - e^{-\left(k_R{}^2 - k_T{}^2\right)^{1/2} y}\left(2k_R{}^2 - k_T{}^2\right), \quad (3.6)$$

$$S = \left(4k_R{}^2 - k_T{}^4\right)\left(k_R{}^2 - k_L{}^2\right)^{1/2}\left(k_R{}^2 - k_T{}^2\right)^{1/2} - 2k_R{}^4(2k_R{}^2 - k_L{}^2 - k_T{}^2). \quad (3.7)$$

The components of integration in Eq. (4) are given as:

$$\int_a^b dy\{\pm d_y(y)P(y) + id_x(y)Q(y)\}, \quad (3.8)$$

where, $d_y(y)$ and $d_x(y)$ are the displacement functions in *y*-direction and *x*-direction, respectively. The displacement functions can be obtained by Hooke's law, $\boldsymbol{d} = \boldsymbol{F}/\boldsymbol{K}$, where $\boldsymbol{d}$ is a displacement matrix, $\boldsymbol{F}$ is a force matrix, and $\boldsymbol{K}$ is a stiffness matrix. The force matrix can be computed by the stress field given by Achenbach (Achenbach and Brind 1981) as:

$$\sigma_{xx} = -2\mu A_R ik_R \left\{ \frac{\left(2{k_R}^2 - 2{k_L}^2 + {k_T}^2\right)e^{-\left({k_R}^2 - {k_L}^2\right)^{1/2} y}}{2{k_R}^2 - {k_T}^2} - e^{-\left({k_R}^2 - {k_T}^2\right)^{1/2} \mathrm{y}} \right\},$$

$$\sigma_{xy} = \mu A_R \frac{\left(2{k_R}^2 - {k_T}^2\right)}{\left({k_R}^2 - {k_T}^2\right)^{1/2}} \left\{ e^{-\left({k_R}^2 - {k_L}^2\right)^{1/2} \mathrm{y}} - e^{-\left({k_R}^2 - {k_T}^2\right)^{1/2} \mathrm{y}} \right\}, \quad (3.9)$$

where μ is Poisson's ratio.

The stiffness matrix is obtained by the equations representing the Hankel function, which is a Bessel function of the third kind.

$$G^I = \frac{ik_L{}^2}{4}\left(H_3^{(1)}(k_L r')\sin 3\theta' + (3 - 4K^2)H_1^{(1)}(k_L r')\sin\theta'\right) -$$

$$\frac{ik_T{}^2}{4}\left(H_3^{(1)}(k_T r')\sin 3\theta' - H_1^{(1)}(k_T r')\sin\theta'\right) + \frac{ik_T{}^3 K}{4}H^*(k_L r', \theta'),$$

$$G^{II} = \frac{ik_L{}^2}{4}\left(H_3^{(1)}(k_L r')\sin 3\theta' + H_1^{(1)}(k_T r')\sin\theta'\right) \quad + \quad (3.10)$$

$$\frac{ik_T{}^3}{4}(H_3^{(1)}(k_T r')\sin 3\theta' - H_1^{(1)}(k_T r')\sin\theta') + \frac{ik_T{}^3}{4}H^*(k_L r', \theta'),$$

where $H_3^{(1)}$ is the third order of the first kind of Hankel function, $H_1^{(1)}$is the first order of the first kind of Hankel function, and

$$H^*(\rho, \pm\pi/2) = \pm\sum_{k=0}^{\infty} \frac{\rho(-\rho^2/4)^k}{(2k+1)(k!)^2}\left[1 + \frac{2i}{\pi}\left\{\ln|\rho/2| - \psi(k+1) - \frac{1}{2k+1}\right\}\right], \quad (3.11)$$

where ρ is a density and $\psi(k+1)$ is a digamma function of a complex variable obtained by differentiating the logarithm of a gamma function.

3.2.2 *Numerical integral solutions of an analytical model*

The ultimate objective of this study is to calculate and verify displacement variations, which is defined by the ratio of displacements as scattered wave and incident wave occurrences. The displacements are calculated from the potentials derived by the singular integral equation (see (3.4)). Notably, numerical integration methods are key to solve the analytical model to provide reliable and accurate displacement variation. Five Gaussian quadrature numerical integration methods are employed: GLEQ, GCQ, GJQ, GHQ, and GLAQ.

The key to the Gaussian quadrature method is to define the node (*x*) and weight (*w*), which is the additional coefficient known as "weight" at the element and given by the weight function, to calculate integration numerically as described in (3.12). The rule of integration is stated as

$$\int_{-1}^{1} f(y)dx \approx \sum_{i=1}^{n} f(y_i)w_i, \quad (3.12)$$

where $f(y)$ is a continuous function, $f(y_i)$ is a dependent variable at a discrete node x_i, and w_i is the weight function at the discrete node y_i.

To define the node or the reference point in the *x* coordinate, an orthogonal polynomial is utilized. Depending on the applied orthogonal polynomial, the five numerical integration methods are classified. The Gauss-Legendre quadrature is the simplest integration problem by Legendre polynomials on [-1, 1], and the weight function is:

$$w_i = \frac{2}{(1 - y_i{}^2)[P'_n(y_i)]^2}, \quad (3.13)$$

where $P_n(x)$ is the Legendre polynomial, which is the solution of the Legendre differential equation. The Gauss-Chebyshev quadrature uses Chebyshev polynomials with respect to the weight function, which is given as:

$$w_i = \sqrt{(1 - y^2)}. \quad (3.14)$$

The Gauss-Jacobi quadrature is for an approximate integral with the Jacobi polynomials and weight function expressed as:

$$w_i = (1 - y)^{\alpha}(1 + y)^{\beta}. \quad (3.15)$$

where f is a smooth function on [−1, 1] and α, β > −1. The interval [−1, 1] can be replaced by any other interval by a linear transformation. The Gauss–Hermite quadrature is a form of Gaussian quadrature for approximating the value of integrals of the following kind, $\int_{-\infty}^{+\infty} e^{-x} f(y)dx$, and the weight function is given as:

$$w_i = \frac{2^{n-1} n! \sqrt{\pi}}{n^2 [H_{n-1}(y_i)]^2}, \quad (3.16)$$

where $H_n(x)$ is a Hermite polynomial, which is the solution to Hermite's differential equation. The Gauss–Laguerre quadrature is an extension of the Gaussian quadrature method for approximating the value of integrals for the following kind $\int_0^{+\infty} e^{-x} f(y)dy$, and the weight function is:

$$w_i = \frac{x_i}{(n + 1)^2 [L_{n+1}(y_i)]^2}, \quad (3.17)$$

where $L_n(y)$ is the Laguerre polynomial, which gives the solution to Laguerre's equation of a second-order linear differential equation. Weight functions of each numerical integration method are described in Table 3.1.

Table 3.1. Weight function of integral methods

Integral method	Weight function
Gauss-Legendre quadrature	$w_i = \frac{2}{(1-y_i{}^2)[P'_n(y_i)]^2}$,
Gauss-Chebyshev quadrature	$w_i = \sqrt{(1-y^2)}$.
Gauss-Jacobi quadrature	$w_i = (1-y)^\alpha(1+y)^\beta$.
Gauss–Hermite quadrature	$w_i = \frac{2^{n-1}n!\sqrt{\pi}}{n^2[H_{n-1}(y_i)]^2}$,
Gauss–Laguerre quadrature	$w_i = \frac{x_i}{(n+1)^2[L_{n+1}(y_i)]^2}$,

3.3 Computational simulations model

Computational simulations, especially finite element (FE) analysis, is the most widely used method to solve field problems using a numerical approach. In this paper, the FE modeling is performed to verify analytical models solved with different numerical integral methods. The model will simulate the wave propagation in the solid media, including the vertical sub-surface crack with different frequencies of incident waves. In detail, the cracks are designed by the different 'a' values and a/b ratios. Three values of the parameter 'a' to simulate subsurface crack in those depths are 12 mm, 18 mm, and 24 mm crack, as denoted in Table 2. The selected parameters are typical sizes in the field area. And two a/b ratios with 0.1 and 0.2 are considered to design the internal crack. The increase in the a/b ratio indicates a decrease in crack sizes. These ratios are selected to compare with the existing analytical solution (Achenbach and Brind 1981). Also, the proposed analytical model will be verified with the FE simulation. Each case has a different wavenumber range. A total of 177 FE models are simulated. 150 FE models are designed for 6 different crack geometry cases simulated varying different frequency ranges. For example, there are 27 models for the C12-0.1 case for simulating different frequencies described in Table 3.2. 27 FE models out of 177 are designed for no crack case.

Table 3.2. Designed crack geometry and simulation numbers by the wavenumber range.

Case	*a* (mm)	a/b	Crack size, *b-a* (mm)	# of model
C12 - 0.1	12	0.1	108	27
C12 - 0.2	12	0.2	48	27
C18 - 0.1	18	0.1	162	25
C18 - 0.2	18	0.2	72	25
C24 - 0.1	24	0.1	216	23
C24 - 0.2	24	0.2	96	23

3.3.1 *Model description*

Typically, an FE simulation requires a large-sized simulation model to avoid unexpected waves reflected from the boundary; otherwise, it will show considerable computation time. Several researchers (Oh et al. 2012) have conducted the FE simulation with damper and energy-absorbing elements (i.e., infinite elements) to reduce the size of the model. The study of FE simulation with damper and infinite element recommends 10 damping zones in an 0.4-0.6/length (distance between wave source and boundary) with 1000 to 2000 of step damping factor increase. Since the simulation model of this paper has a shorter distance between the wave source and boundary, 1000 of the initial damping factor and 5000 of the incremental damping factor are chosen. The FE models in this paper compose of three groups: the solid medium group, damper group, and wave absorbing infinite element group. The solid medium size is 4000 mm (width) × 1000 mm (height). The 500 mm damper zone is at the boundary of the solid medium group and is represented in the rainbow color of Figure 3.2. The infinite element is placed at the dampers' end. The

applied material properties are assumed for the typical solid material (ρ= 2400 kg/m3, E = 35 GPa, and υ = 0.2), which is the largest component in the model. Both the analytical model and the FE model have applicability limitations for typical material cases having material nonlinearities that may affect wave propagation. We assume linear elastic wave propagation. The explicit FE simulation does not enforce the structural equilibrium (Kandil et al. 2014). Therefore the structural boundary condition is not necessary for the structural equilibrium of the internal structure forces under the external load. The model of the ABAQUS solver is designed using a 2D four-node plane strain element (CPE4R) with 2 mm mesh size for the solid medium group and dampers.

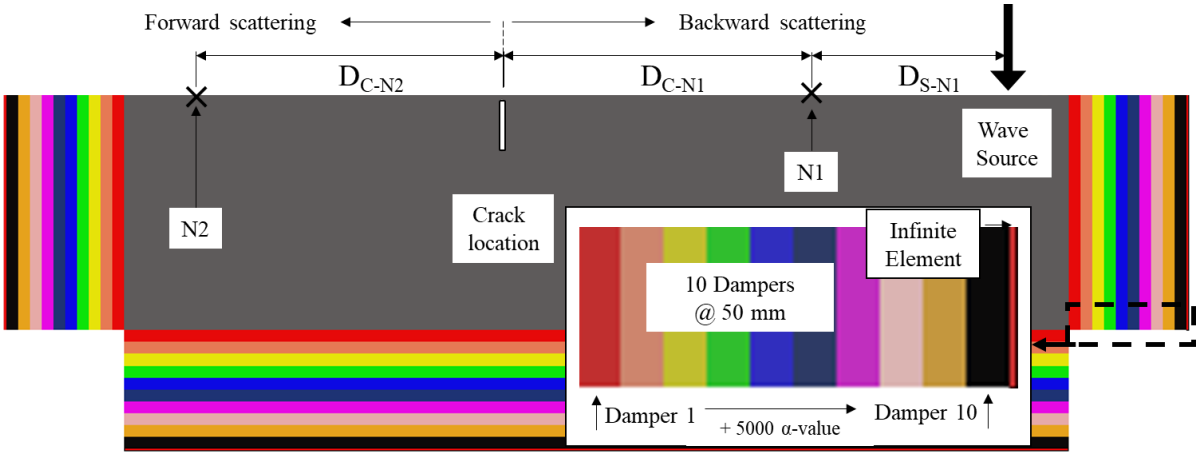

Figure 3.2. Details of FE model: N1 is the listening node for the backward scattered waves, N2 is the listening node for the forward scattered waves, D_{C-N1} and D_{C-N1} are the distances between the crack and nodes, N1 and N2, respectively, D_{S-N1} is the distance between the wave source and N1. The figure also includes ten dampers in rainbow colors on the three sides of the solid medium and an infinite element in the thin red layer at the end of dampers. The illustration shows the required component and geometry to simulate the wave propagation in the cracked model.

Table 3.3. Damping factors for optimum damping gradient of FE model.

Damper 1	Damper 2	Damper 3	Damper 4	Damper 5	Damper 6	Damper 7	Damper 8	Damper 9	Damper 10
1000	6000	11000	16000	21000	26000	31000	36000	41000	46000

The artificially attenuated dampers are designed by gradually increased alpha mass-proportional damping factors, as described in Table 3.2. Typically, the damper zone allows attenuating low-frequency waves, while the infinite element absorbs high-frequency waves (Oh et al. 2012). The infinite element is CINPE4.

3.3.2 ***Discussion of the wave separation in FE simulation***

The model based on the wave separation in the P-wave and surface waves is studied in this section. As illustrated in Figure 3.2, the $D_{C\text{-}N1,\,N2}$ represents a distance between the crack location and listening nodes in the *x*-direction. In contrast, D_{N1} represents the distance between the source point and the backward listening node in the *x*-direction. Typically, each propagated wave (e.g., P-wave, S-wave, and surface wave) has a different arrival time due to each wave's different speed. For example, in the simulation with given material property, the speed of the P-wave (C_P) and surface wave (C_R) are 4084 m/s and 2265 m/s, respectively. However, the model requires a minimum distance between the wave source and the listening nodes to obtain the pure waveforms (e.g., surface wave) so as to avoid overlapped waves.

Figure 3.3 shows four different wave groups excited by an incident sine wave. The two-wave groups (P-wave and surface wave) are incident waves in the time range between 0.2 and 0.8 x 10^{-3} seconds, while the other two-wave groups are the reflected waves at the crack in the time range between 1.2 and 1.6 x 10^{-3} seconds. The three following groups must be considered to obtain a clear P-wave and surface wave separation: i) Reflected P-waves by the crack should not pass when the incident surface waves pass through at *N1*, as $\frac{D_{S-N1}+D_{C-N1}+D_{C-N2}}{C_P} \neq \frac{D_{S-N1}}{C_R}$. ii) the distance, $D_{C\text{-}N1}$ should be enough to have a wave separation in P- and Surface-waves at *N1* (see Region A in Figure 3), $\frac{D_{S-N1}}{C_P} - \frac{D_{S-N1}}{C_R} > T$, where *T* is period of the incident wave. $D_{C\text{-}N1,\,N2}$ should be enough to have a wave separation between the reflected P- and Surface-waves by the crack at the *N1* and *N2* (see region B in Figure 3), $\frac{D_{C-N1,N2}}{C_P} - \frac{D_{C-N1,N2}}{C_R} > T$. In addition, the simulations are designed to avoid the S-wave effect to obtain the pure surface wave by receiving only the horizontal displacement, which is in a longitudinal direction. Thus the S-wave was eliminated.

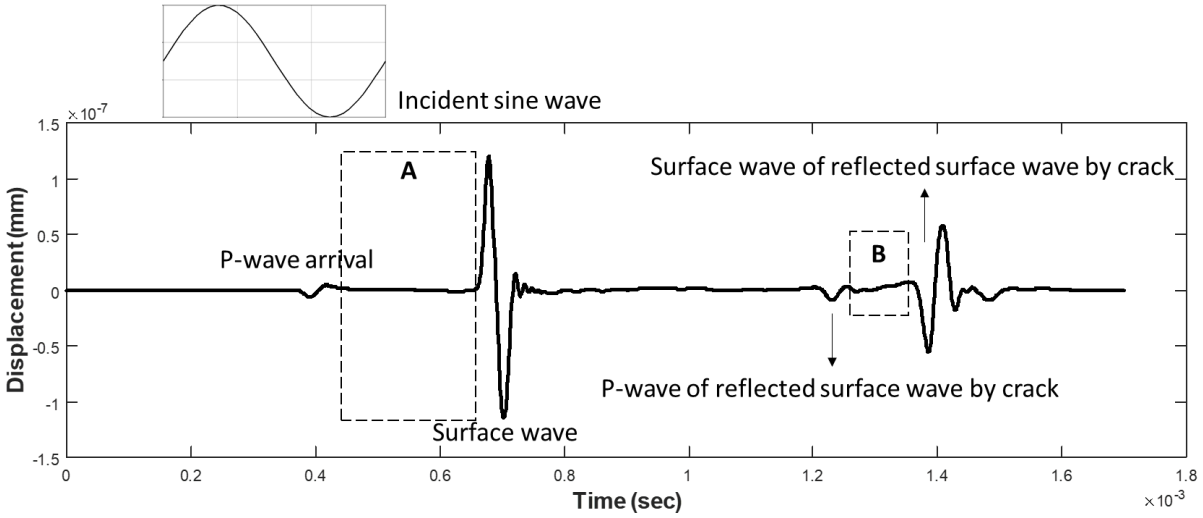

Figure 3.3. FE simulation results of the time-domain waveform at the node N1 in horizontal x-displacement: Waves from the incident wave and reflected waves by the crack are calculated. Both Region A and B show different arrival times as wave separations of the P-wave and surface waves. Region A is associated with the incident waves, and B is associated with the reflected waves by crack. The image explains the waveform in the time domain and the required distance of $D_{C-N1,N2}$ and D_{S-N1} to obtain a pure waveform of the surface waves.

3.4 Results and discussions

The FE simulation is performed to verify the analytical model introduced in Section 3.2. The numerically calculated analytical model and FE simulation results are described to the displacement variation of the ratio of the backward scattered wave and incident wave, u^{bs}/u^{in} and the ratio of the forward scattered wave and incident wave u^{fs}/u^{in} by two parameters of 'a' and 'k_R', which is related to the frequency ($k = 2\pi f/C$: k is a wavenumber, f is a frequency, and C is the wave speed).

3.4.1 *Results of the analytical model and FE simulation*

The analytical model with five different integral methods is computed using MATLAB in accordance with the procedures of Section 3.3. The FE simulation is designed based on the details described in this section. The analytical model and FE simulation results are normalized with the highest magnitude of the variation

ratio to compare each case's shape and tendency. The wavenumbers are considered to have the displacement variation curves in the $k_R a < 4$ range by the given 'a' values (e.g., 12 mm, 18 mm, and 24 mm). In the simulation result of the forward scattered case, the pure scattered waves are obtained at a higher frequency range than 10 kHz. Since the lower frequency (e.g., 10 kHz or below) has a longer wavelength, the scattered P-wave overlaps the scattered surface wave.

Figure 3.4 includes two graphs of the backward and forward scattered cases of the C18-0.2 model, which has a 72 mm crack size. In this geometry, the higher amplitude of scattered energy variation shows in the forward scattered direction (see the amplitude of the u^{fs}/u^{in} in Figure 3.4) than in the backward direction (see the amplitude of the u^{bs}/u^{in} in Figure 3.4).

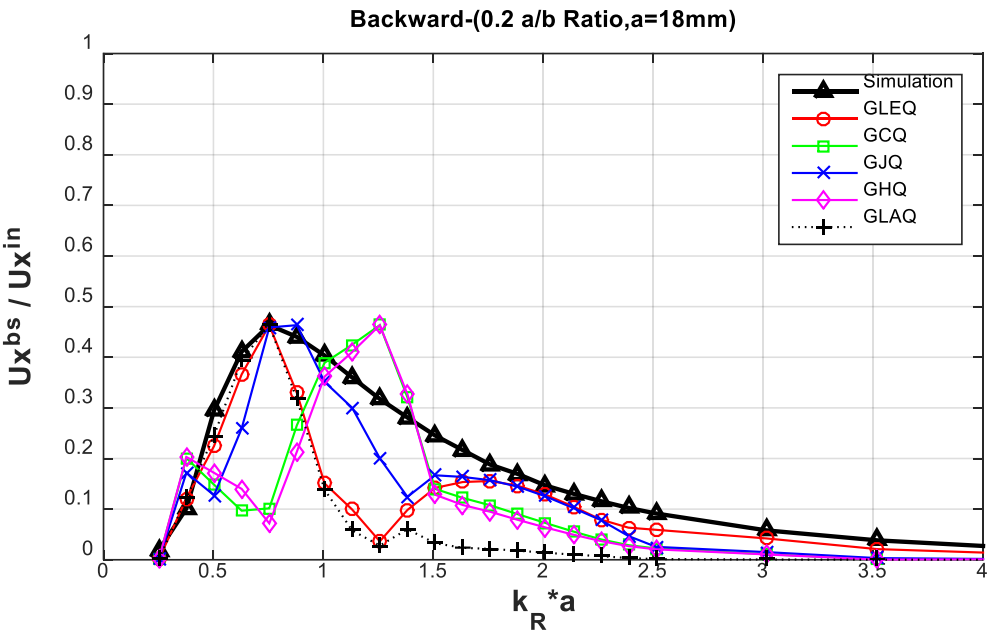

(a)

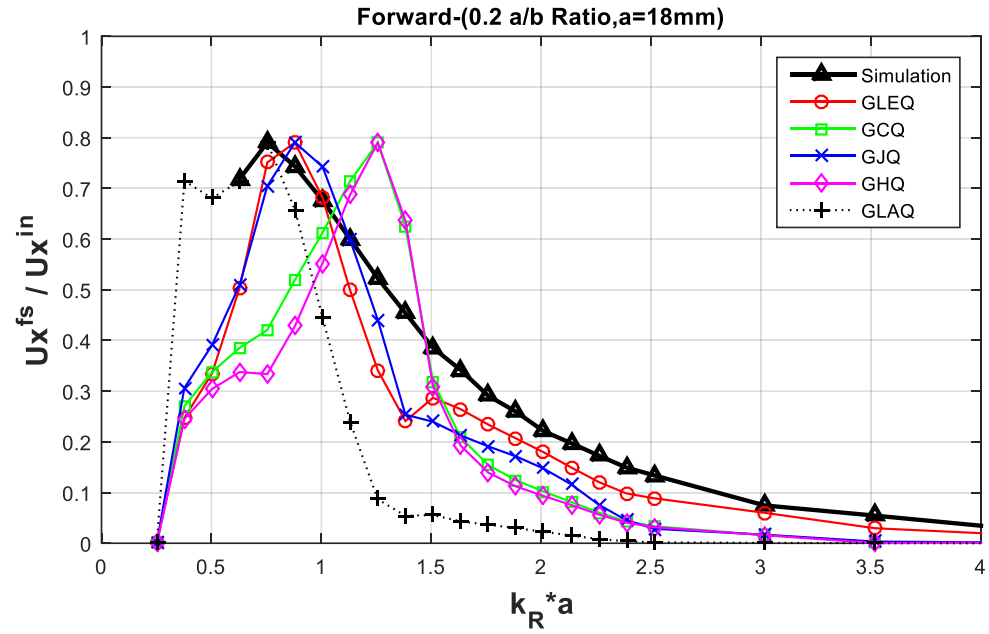

(b)

Figure 3.4. Displacement variation curves from the analytical model and FE simulation by the different direction of the C18-0.2 model: (a) backward scattering and (b) forward scattering result. The curves show the shape of the displacement variation denoted as u^{bs}/u^{in} and u^{fs}/u^{in} in the analytical model and simulation result. The results indicate that the analytical models solved by different internal methods show a shape similar to that of the FE simulation in both the forward and backward case.

The displacement variation changes depending on the distance between the ground and top crack denoted as *'a',* and the crack size are described in Figure 3.5. The three models considered are C12–0.2, C18–0.2, and C24–0.2, which have depths of 12 mm, 18 mm, and 24 mm respectively and a crack size of 48 mm, 72 mm, and 96 mm. The models have the same *a/b* ratio, 0.2. Regardless of the crack depth and size, a similar amount of wave scattering occurs in the same *a/b* ratio.

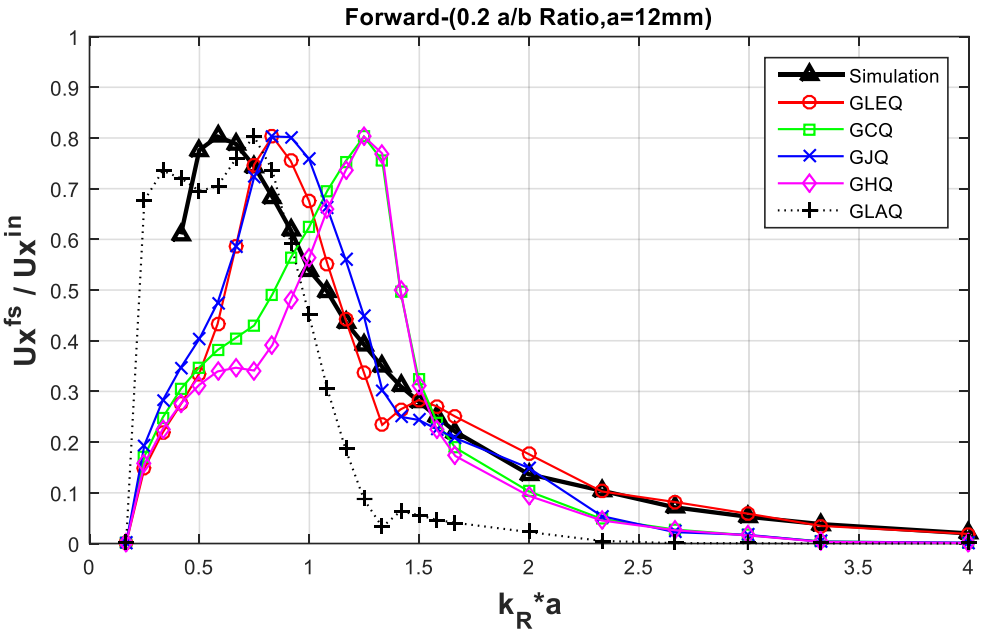
Forward-(0.2 a/b Ratio,a=12mm)
Simulation
GLEQ
GCQ
GJQ
GHQ
GLAQ
Ux^fs / Ux^in
k_R*a

(a)

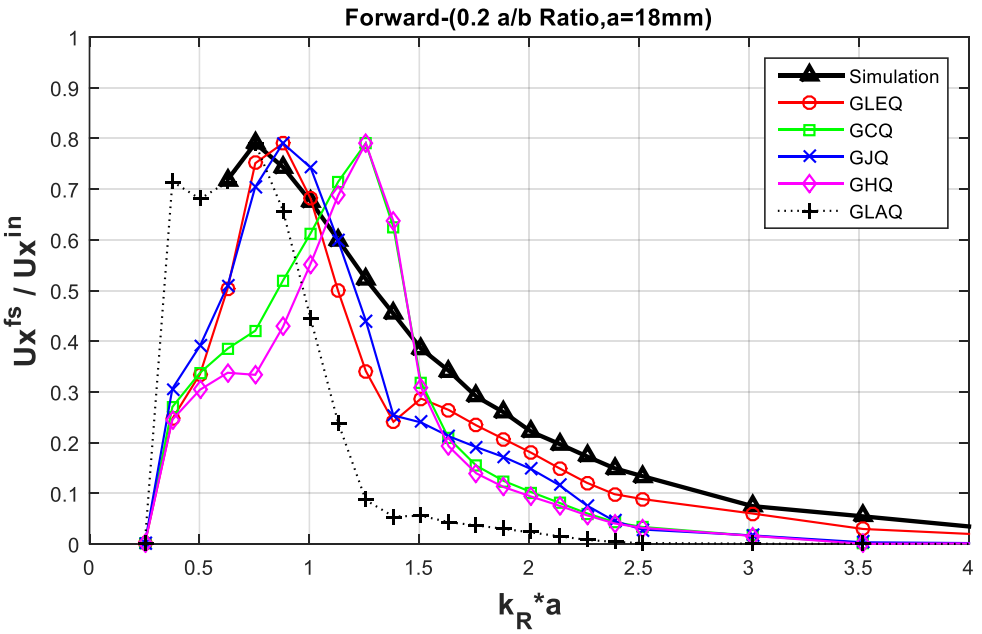
Forward-(0.2 a/b Ratio,a=18mm)
Simulation
GLEQ
GCQ
GJQ
GHQ
GLAQ
Ux^fs / Ux^in
k_R*a

(b)

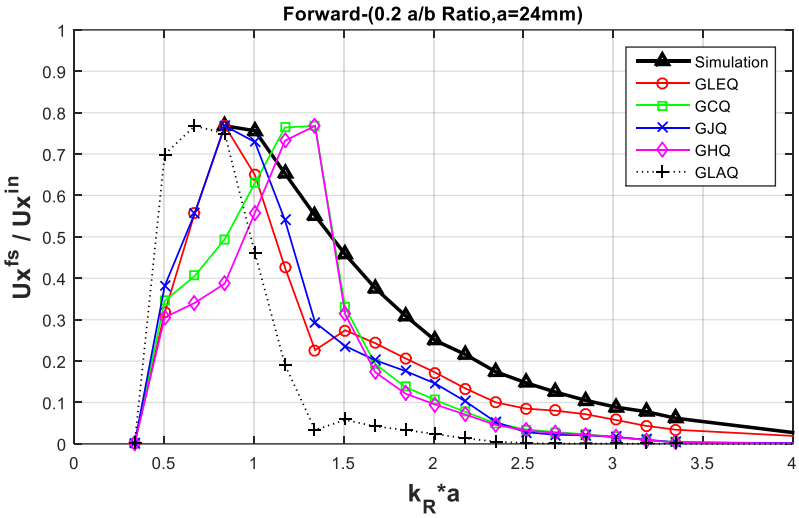

(c)

Figure 3.5. Displacement variation curves of analytical model solving five different integral methods and FE simulation shown with different crack depths, 'a' of the forward scattered models: (a) result with a 12 mm a and a 0.2 a/b ratio model (C12–0.2), (b) results with an 18 mm a and 0.2 a/b ratio model (C18–0.2), and (c) results with 24 mm of a and a 0.2 a/b ratio model (C24–0.2). The figure implies the deeper crack depth which is a higher 'a' result shows the peak point at the higher $k_R a$ value.

The displacement variations based on crack size change is described in Figure 6, including C12–0.1 and C12–0.2 case, which have a 108 mm and 48 mm crack size. The graph result showing 0.1 of the a/b ratio (see Figure 6 (a)) is obtained by a longer crack than the 0.2 cases (see Figure 3.6 (b)), and the model shows a sharper triangular shape of curves in the lower $k_R a$ value. The small crack size case has its peak value at the relatively higher $k_R a$. Since the lower frequency waves can pass through the smaller length or size of the crack, it shows lesser wave scattering energy in the lower $k_R a$. Thus, the peak displacement variation is formed in the higher $k_R a$ as part of a smaller crack model.

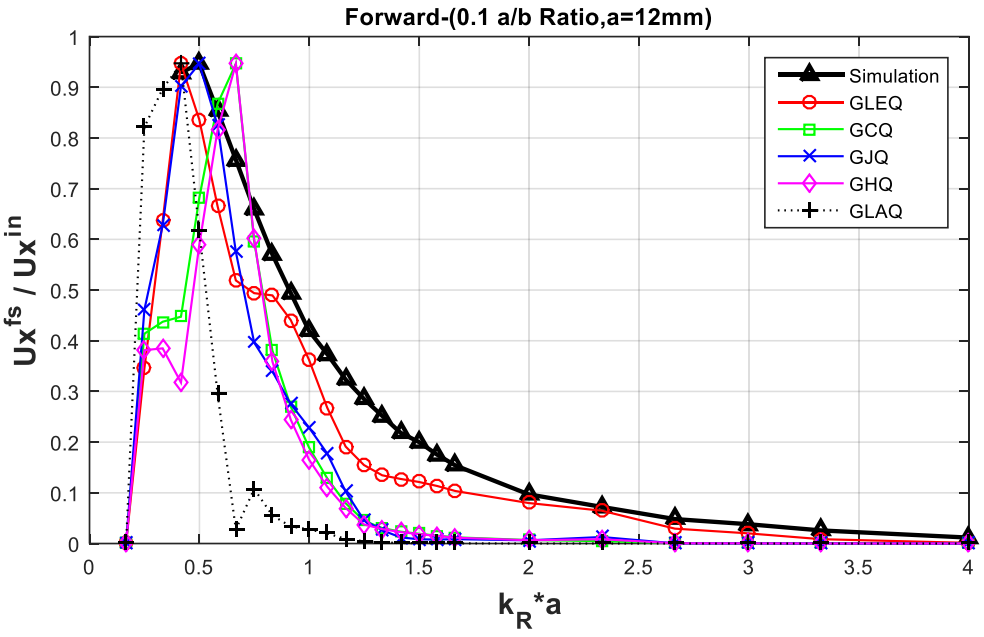

(a)

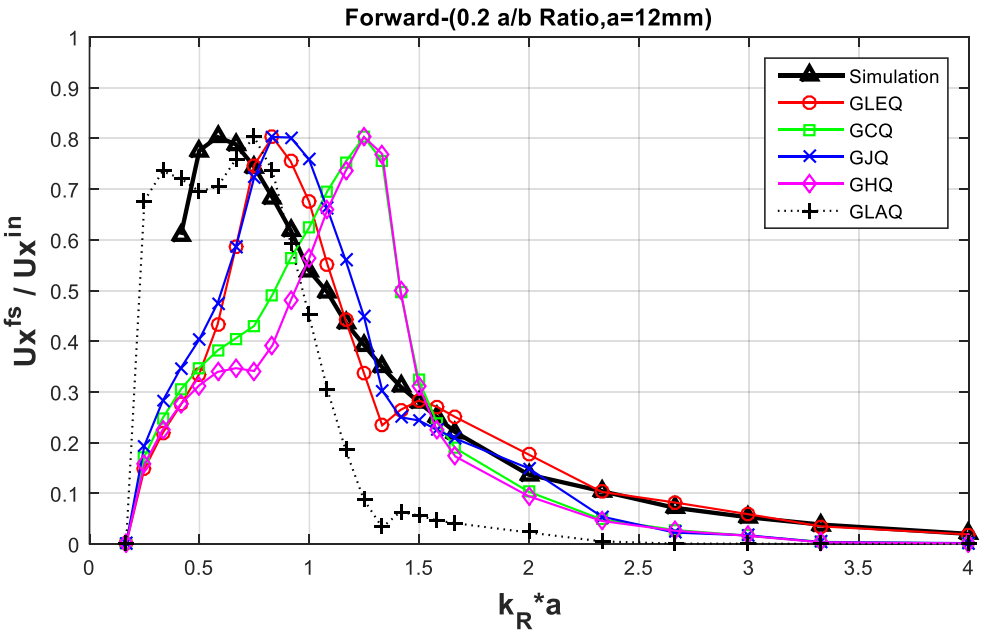

(b)

Figure 3.6. Displacement variation curves of the analytical model and FE simulation by different a/b ratio of the forward scattering models: (a) result from 0.1 a/b ratio model (C12–0.1), (b) result from 0.2 a/b ratio model (C12–0.2). The figure implies that the longer crack model represents the higher wave scattering energy and narrow distribution curve. The peak displacement variations of the shorter crack model are obtained at the relatively higher $k_R a$ value.

3.4.2 *Representative correlation values of curves*

The correlation coefficient is used for quantifying the similarity between two variables. In this paper, Pearson's correlation coefficient is adopted to evaluate the similarity of the displacement variation curves. The method of Pearson's correlation coefficient gives the coefficient (r) value between −1 and 1 to define the similarity of the two curves. When $r > 0$, it means that the two variables are positively correlated, and when $r < 0$, the two variables are negatively correlated. When $|r| = 1$, it means that the two variables are completely and linearly correlated, that is, they have a functional relationship. When $r = 0$, it refers to the nonlinear correlation between the two variables. When $0 < |r| < 1$, it means there is a certain degree of linear correlation between the two variables, as described in Table 3.4. The closer $|r|$ is to 1, the closer the linear relationship is between two variables. If r is closer to 0, the weaker the linear correlation is between two variables, as described in

Table 3.5.

Table 3.4. Condition of correlation coefficient and its relationship between variables.

Condition of correlation coefficient	Relationship between variables
$r > 0$ or $r < 0$	Positive correlation or negative correlation
$\|r\| = 1$	Completely linear correlation (functional relationship)
$r = 0$	Nonlinear correlation
$0 < \|r\| < 1$	Certain degree of linear correlation

Table 3.5. Criteria for a correlation coefficient.

Rank of correlation coefficient	Meaning
$\lvert r \rvert < 0.4$	Low linear correlation
$0.4 \leq \lvert r \rvert < 0.7$	Significance correlation
$0.7 \leq \lvert r \rvert < 1.0$	Highly linear correlation

The Pearson's correlation coefficient (r) is calculated by (Egghe and Leydesdorff 2009):

$$r = \frac{\sum_{i=1}^{n}(X_i - \mu_X)(Y_i - \mu_Y)}{\sqrt{\sum_{i=1}^{n}(X_i - \mu_X)^2 \sum_{i=1}^{n}(Y_i - \mu_Y)^2}} \quad (3.18)$$

where μ_X and μ_Y is the mean of variables X and Y. In the discussion section, the results of the FE simulation will be compared with the analytical models using five different numerical integration approaches.

The calculated correlation coefficients are described in Table 3.6. The averages of the obtained correlation coefficients from the five integral methods range from 0.79 to 0.94. Therefore, all five integral methods are in the highly linear correlation condition in

Table 3.5. Among the applied integration methods, the Gauss-Legendre quadrature method shows a higher correlation, e.g., 0.94, and obtained an averaged correlation coefficient.

The distance of the correlation coefficient between the analytical model and FE simulation can be explained with considerable limitations: 1) the assumption of the analytical model, which is not considered in FE simulation and 2) methodological difference between the analytical solutions and FE simulation.

The analytical model is derived based on many assumptions to make the mathematical logic simple. For example, the analytical model uses Green's function expressed in terms of the Hankel functions to obtain the stiffness function (see G^I and G^{II} in (3.10)). Since Green's function adopts a point source effective solution based on the Dirac delta function in mathematical terms, the analytical model limits the non-localized explicit solution. Thus, the results show a difference from the FE simulation results, which is the explicit time variable solution. In addition, the FE simulation results are affected by the distance ($D_{C-N1,N2}$ and D_{S-N1}) and incident waveform; however, the analytical model has no variables pertaining to the horizontal distance and incident waveform.

Table 3.6. The calculated correlation coefficient results between FE simulation and analytical solution by five different numerical methods; the Gauss-Legendre quadrature method (GLEQ) shows the highest similarity.

	GLEQ	GCQ	GJQ	GHQ	GLAQ
A12 - 0.1	0.98	0.90	0.95	0.86	0.73
A12 - 0.2	0.84	0.63	0.86	0.56	0.93
A18 - 0.1	0.98	0.86	0.89	0.86	0.83
A18 - 0.2	0.96	0.85	0.96	0.80	0.86
A24 - 0.1	0.95	0.83	0.86	0.82	0.80
A24 - 0.2	0.92	0.89	0.93	0.86	0.75
Similarity	0.94	0.83	0.91	0.79	0.82

Furthermore, mean absolute error (MAE) is calculated to perform the comparative study by calculating the errors as:

$$MAE = \frac{\sum_{i=1}^{n} |Y_i - X_i|}{n}. \qquad (3.19)$$

The analytical solution using the Gauss-Legendre quadrature method also shows the lowest MAE as an average MAE of 0.87.

Table 3.7. The calculated MAE between FE simulation and analytical solution by five different numerical methods; the Gauss-Legendre quadrature method (GLEQ) shows the lowest MAE.

	GLEQ	GCQ	GJQ	GHQ	GLAQ
A12 - 0.1	0.15	0.16	0.17	0.18	0.22
A12 - 0.2	0.50	0.60	0.65	0.62	0.47
A18 - 0.1	0.05	0.05	0.06	0.06	0.16
A18 - 0.2	0.08	0.13	0.10	0.06	0.07
A24 - 0.1	0.02	0.02	0.02	0.04	0.15
A24 - 0.2	0.07	0.09	0.08	0.04	0.07
Similarity	0.87	1.06	1.09	1.00	1.14

CHAPTER 4 VERIFICATION OF THE WAVE SCATTERING MODEL

4.1 Motivations

Concrete is extensively used in construction material due to its high compressive strength but typically low tensile strength. Deterioration in concrete is caused by a variety of environmental factors (e.g., freeze-thaw cycle, chemicals, abrasion, erosion). These damages also occur over time through different mechanisms through hydraulic and thermal shrinkage, swelling, deformation, and external load. In particular, vertical cracks perpendicular to concrete surfaces are typical and critical damages caused by several factors, including structural deformation or external load. Consequently, extensive damages result in degradation of material property, corrosion of reinforcement, and even structural failure. Thus, effective detection of concrete cracks is required in a timely manner to better predict service life and monitor structural conditions at an early stage.

There are two types of vertical cracks: surface-opening and subsurface cracks. The surface-opening crack (or surface crack) grows or extends from a surface boundary into an internal medium and vice versa; thus, the crack can be visible on the surface. Several nondestructive evaluations (NDEs) have been developed to detect surface-opening concrete cracks: visual inspection, radiography (Gooch 2007), infrared images (Wang et al. 2018), thermography (Jang and An 2018), and stress wave-based NDE (Aggelis et al. 2010; Brockhaus et al. 2014; Çam et al. 2005; Ham and Popovics 2015a; In et al. 2017; Li et al. 2020; Schmerr 2001; Zhu and Popovics 2005). Stress wave-based methods generally present highly accurate and sensitive crack detection results (Jang and An 2018). One of these approaches uses ultrasonic pulse velocity (UPV) to estimate depths of surface-opening cracks by measuring a time of flight (TOF) of ultrasonic waves. The accuracy of the crack depth estimation is often influenced by the shape of crack tips and debris-filled in the crack (Kee et al. 2011). The other stress wave-based approach uses surface waves that tend to be beneficial in the inhomogeneous medium, presenting higher wave energy than body waves (Hévin et al. 1998; Miller and Pursey 1955). The mechanical wave-based study, which utilizes pulse propagation characteristics such

as wave velocity or attenuation, has demonstrated sensitivity to cracks (Ham and Popovics 2015c). The wave attenuation or wave energy loss is typically defined as a physical attenuation caused by scatterer (e.g., cracks) (Lou et al. 2019). Hévin et al. (1998) introduced a method using a spectral ratio that is changing by a depth of surface-opening crack (Hévin et al. 1998). Popovics et al. (2000) proposed a surface wave transmission (SWT) method that is performed across the discontinuities or surface-opening crack. The crack is located in between these sensors (Popovics et al. 2000). The result presents spectral response variation between the incident surface wave and the transmitted surface wave in the frequency domain. There are also recent advances in vertical crack detection, including diffuse ultrasonic waves and leaky surface waves. Zhu and Popovics (2005) utilized surface waves to detect and to image surface-opening cracks by measuring leaky surface waves from air-coupled sensors (Zhu and Popovics 2005). On the cracked region, a low wave energy ratio is obtained, presenting less transmission energy and higher attenuation. In et al. (2017) investigated the vertical surface crack to estimate the crack depth using time delays of the peak energy arrival time of diffuse ultrasonic waves and provided significant agreements with the core test results (In et al. 2017). Despite these efforts, they may present certain limitations and challenges for in-depth understanding and monitoring of internal vertical cracks.

An internal vertical crack is formed beneath the medium surface and possibly started from internal damage areas, including the high-level stress concentrated zone, corroded reinforcements, and delamination between successive layers. These cracks caused by structural deformation or external loads in thick plate-like structures (e.g., concrete pipe, slab) are critical; the subsurface crack can be located in a medium or to the opposite surface where being likely inaccessible. Consequently, it results in the discontinuity of the entire thickness and possibly causes structural collapse. In addition, the crack is invisible until it extends to an accessible surface allowing moisture and other chemicals to penetrate and deteriorate the concrete. Thus, detecting and evaluating the damage is still challenging not only because of crack invisibility on the surface but also the inapplicability of current advanced approaches. In theory, both surface-opening cracks and subsurface cracks can be evaluated using a Rayleigh wave or surface wave of which amplitude decreases

by a distance from the surface to wave penetration depth, so-called effective depth. The effective depth is, in general, influenced by the incident wave frequency (Achenbach 2000). Aggelis et al. (2011) performed experiments and wave simulations to identify the relationship between wave parameters (e.g., velocity, amplitude, frequency) and depth to the internal vertical crack from the surface (Aggelis et al. 2011). They concluded that the elastic wave parameters are influenced by the geometrical characteristic of the internal vertical crack.

Analytical models of surface wave scattering by an internal vertical crack (SWS-IVC) have been studied over the past decades (Achenbach et al. 1981, 1983; Achenbach and Brind 1981; Mendelsohn et al. 1980; Visscher 1985). The established elastic wave equation of forward and backward scattering is affected by variables of material property, incident wave frequency, and crack tip depth (depth-to-crack) which is a distance between the surface and top crack tip—the analytical solutions of the model present the relation between scattered surface waves and crack sizes presenting as "response variation". Kang et al. (2020) solved singular integrals of the analytical model with a comparative study of various numerical integral solutions including, Gauss–Legendre quadrature, Gauss–Chebyshev quadrature, Gauss–Jacobi quadrature, Gauss–Hermite quadrature, and Gauss–Laguerre quadrature (Kang et al. 2020). They also conducted finite element (FE) simulations with different crack geometries and incident wave frequencies to validate the analytical model. In their study, Gauss-Legendre quadrature to solve the integral representations of the SWS-IVC model show the highest correlation based on FE simulation results. In spite of these efforts, further studies of SWS-IVC are needed for in-depth understanding (i.e., the relation between the surface wave scattering and crack geometry) that requires additional experimental verification with actual cracks utilizing various testing protocols such as wave parameter studies.

This paper focuses on studying internal vertical crack evaluations, conducting verification of analytical, numerical, and experimental results, and establishing a relationship between Rayleigh wave scattering and subsurface crack geometry related to crack size depth-to-crack. The experimental study will be conducted on a concrete pipe sample with various induced cracks. A surface wave is induced in the concrete samples

with low-frequency (10 to 20 kHz) mechanical wave source operating by proposed automatic impactors. Non-contact MEMSs located 10 mm above the concrete surface are used to detect leaky Rayleigh waves emanating from concrete. The numerical study is also conducted with dynamic FE simulations to obtain the response variation of SWS-IVC with various models. The FE simulation models are designed with the specific pipe geometry and its concrete material properties that are similar to the prepared concrete sample in the experimental study. The analytical study aims to advance the SWS-IVC model solving by the most relevant singular integral solution. The analytical model is validated through FE simulations and experimental measurement. A comparative study is then conducted between the obtained response variation curves from analytical, numerical, and experiment results by calculating multiple correlation coefficients. Finally, we suggest a physical meaning/basis for observed wave parameters in the response variations in order to detect the internal cracks. These contributions represent advances to evaluate the existing internal crack by using the response variation approach of SWS-IVC with the supplementary energy attenuation-based crack profile.

4.2 Methodology

Wave scattering is generally categorized as weak scattering and strong scattering. Strong scattering likely occurs in higher impedance mismatch between scatterers and the background material (e.g., air- or liquid-filled crack vs. concrete) and in relatively large scatterer compared to a wavelength of the incident wave (Ham et al. 2017). Here, this study focuses on the investigation of "response variation" of strong SWS-IVC in the analytical model, FE simulations, and experiments. In this study, the response variations are key to understand SWS-IVC and to detect these cracks. The response variations curve is obtained from the wave response (e.g., velocity, displacement) ratio of a forward scattering wave to an incident wave with respect to the incident wave frequency and crack geometry. In this study, the incident wave frequency and crack geometry is expressed as wavenumber, k and distance between the surface and the top of the crack tip so-called depth-to-crack, a (i.e., $k_R a$, where $k_R = 2\pi f/C_R$, k_R is the wavenumber of surface waves, f is the

incident wave frequency, and C_R is the surface wave velocity). The schematic diagram in Figure 4.1 illustrates Rayleigh wave propagation across a single internal vertical crack in a medium. Forward transmitted waves and backward and forward scattering waves by the crack are propagated through the medium.

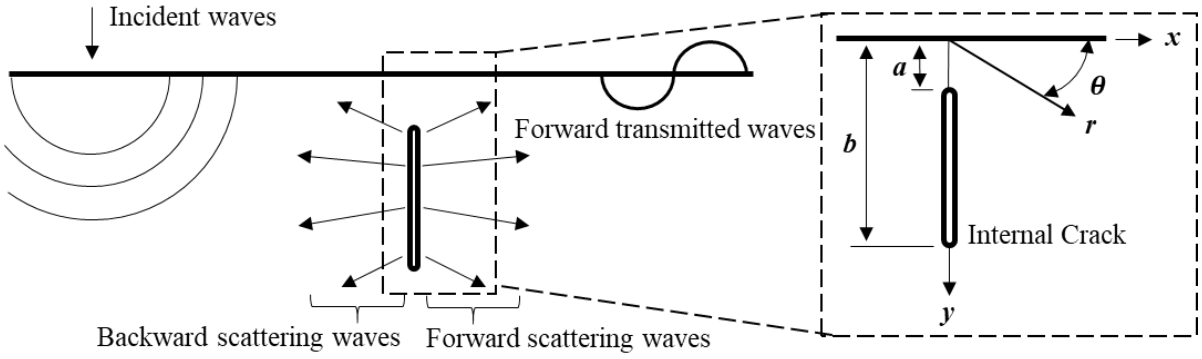

(a) (b)

Figure 4.1. Schematic diagram of wave propagation and internal crack details: (a) wave propagation at the internal vertical crack in two-dimensional (2-D) half-plane and (b) details of internal vertical crack. Backward scattering, forward scattering, and forward transmitted waves are propagated in the given geometry. Crack tips are characterized as y = a and y = b. r and θ are components of the polar coordinate. a is the distance between the surface and the top of the crack tip referred to as depth-to-crack.

4.3 Analytical SWS-IVC model

The analytical SWS-IVC model is assumed in a homogeneous, isotropic, and linearly elastic solid medium occupying the half-plane ($y \geq 0$), which is *z*-invariant in (*x*, *y*, *z*) coordination. An internal vertical crack has tips located at $y = a$ and $y = b$, as shown in Figure 4.1 (b). The main purpose of the analytical solution is to provide a response in scattered fields (e.g., displacement of scattering wave) by the internal vertical crack, satisfying the two-dimensional (2-D) boundary value problem (Achenbach et al. 1987; Achenbach and Brind 1981; Gregory 1975). The displacement is obtained from the analytical SWS-IVC model as a final solution to calculate the wave response. The response variation (e.g., displacement variation) curve is created based on the relation between the wave response ratio and $k_R a$. The anlyatical curve, ultimately is

compared with results from the FE simulations and experiments. Detailed procedures to obtain analytical response variation with forward scattering waves and incident waves are introduced in this section.

The equations of constant *A* and *B* from Eq. (3.3) and Eq. (3.4) are substituted into the displacement potential of Eq (3.2). Ultimately, the displacement field of forward scattering waves can be expressed as a key equation to get the response variation as follows:

$$u_x^{fs} = \partial \frac{\left(2k_R{}^2 - k_T{}^2\right)^2 k_R e^{ik_R x - \left(k_R{}^2 - k_T{}^2\right)^{\frac{1}{2}} y}}{2k_T{}^2\left\{\left(4k_R{}^2 - k_T{}^4\right)\left(k_R{}^2 - k_L{}^2\right)^{1/2}\left(k_R{}^2 - k_T{}^2\right)^{1/2} - 2k_R{}^4\left(2k_R{}^2 - k_L{}^2 - k_T{}^2\right)\right\}} M(y) \Big/ \partial$$
$$+ \partial \frac{2ik_R\left(k_R{}^2 - k_L{}^2\right)^{\frac{1}{2}} e^{ik_R x - \left(k_R{}^2 - k_T{}^2\right)^{\frac{1}{2}} y}}{2k_T{}^2\left\{\left(4k_R{}^2 - k_T{}^4\right)\left(k_R{}^2 - k_L{}^2\right)^{1/2}\left(k_R{}^2 - k_T{}^2\right)^{1/2} - 2k_R{}^4\left(2k_R{}^2 - k_L{}^2 - k_T{}^2\right)\right\}} M(y) \Big/ \partial y, \quad (4.1)$$

where

$$M(y) = \int_a^b dy\left\{d_y(y)R(y) + id_x(y)Q(y)\right\}, \quad (4.2)$$

It is noted that since Eq. (4.2) has the singular integral equation, various numerical integration methods can be applied to solve the final forward scattering displacement. For example, Kang et al. (2020) solve the singular integral with Gauss-Legendre quadrature as the most relevant solution (Kang et al. 2020).

4.4 Numerical simulations

Numerical FE simulations are performed to obtain the response variation with respect to $k_R a$. The simulation result is ultimately compared with analytical and experimental results. Various outputs (e.g., velocity, displacement, acceleration) from simulations are obtained to create the response variation curve. In particular, the velocity response is mainly focused on comparing with experimental response variations that are obtained from non-contact velocity sensors, micro-electromechanical systems (MEMSs) (Ham and Popovics 2015b). Thus, the velocity response ratio of a forward scattering wave to an incident wave is

computed. To create response variation curves, various frequencies of input excitation are designed in the simulation model at a specific location indicated as an arrow on the red node in Figure 4.2 (a). These designed frequency values are already applied in the analytical model to provide the same scale of $k_R a$ on the x-axis of the variation curve for a comparative study. A total of 18 FE simulations are conducted with 18 different input excitation frequencies (see Figure 4.2 (b)). In our study, ABAQUS/EXPLICIT is used to formulate the dynamic FE simulations of the concrete structure, where an anisotropic, elastic plate with density ρ, Young's modulus E, Poisson's ratio υ, is modeled. The applied material properties (ρ= 2400 kg/m^3, E = 35 GPa, and υ = 0.2) are used for the typical concrete that is the same material in the analytical model. 2-D four-node plane strain reduced integration elements (CPE4R) are used through the model with a 2 mm-mesh for the solid medium. Reduced time integration, which uses fewer Gaussian coordinates, is employed in the software to minimize the computation time. The concrete pipe model has a diameter of 61 cm (24 in.) and a thickness of 7.5 cm (3in.). The model includes a crack depth, b-a (see Figure 4.1 (b)), of 5 cm from the outer surface. In this model, the fixed crack depth indicates a depth-to-crack, a of 2.5 cm. The model simulates an internal vertical crack from the inner surface where is the only accessible side in a real-world field test. In general, the outer surface cannot be accessible, as shown in Figure 4.2 (a). In the model, four different node outputs are selected to obtain wave signals (note green circled nodes in Figure 4.2 (a)). Node 1 is placed before the crack to capture the incident waves, while Node 2 to Node 4 is placed after the crack to obtain forward scattering waves. The dynamic response of velocity is obtained from the FE simulations as shown in Figure 4.2 (b). To calculate the wave response ratio, a first negative peak of the surface wave amplitude is selected. These different listening points are investigated in Result section.

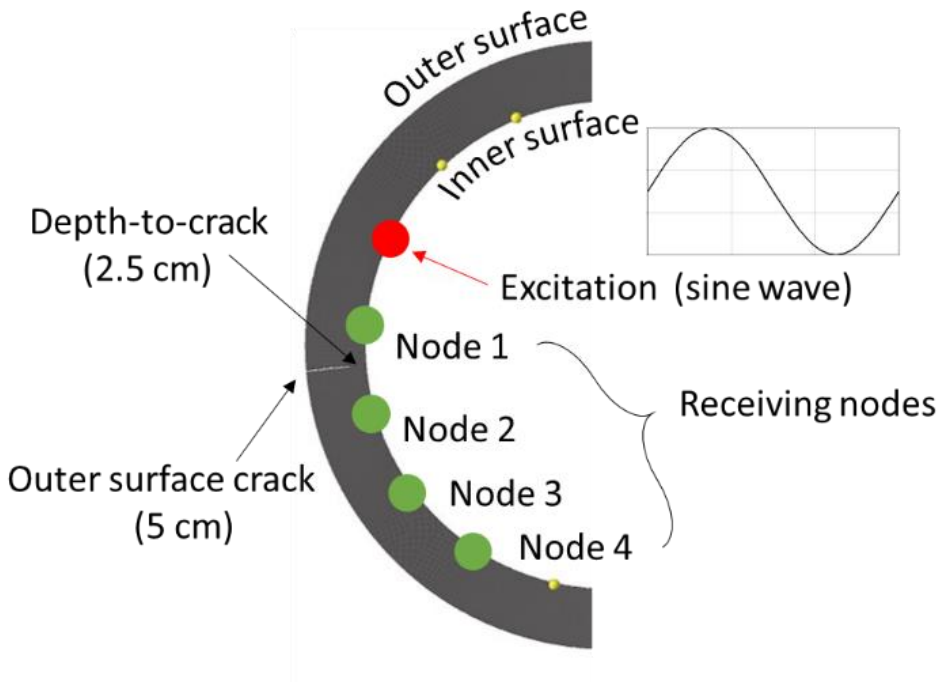
Outer surface
Inner surface
Depth-to-crack
(2.5 cm)
Excitation (sine wave)
Node 1
Receiving nodes
Node 2
Outer surface crack
(5 cm)
Node 3
Node 4

(a)

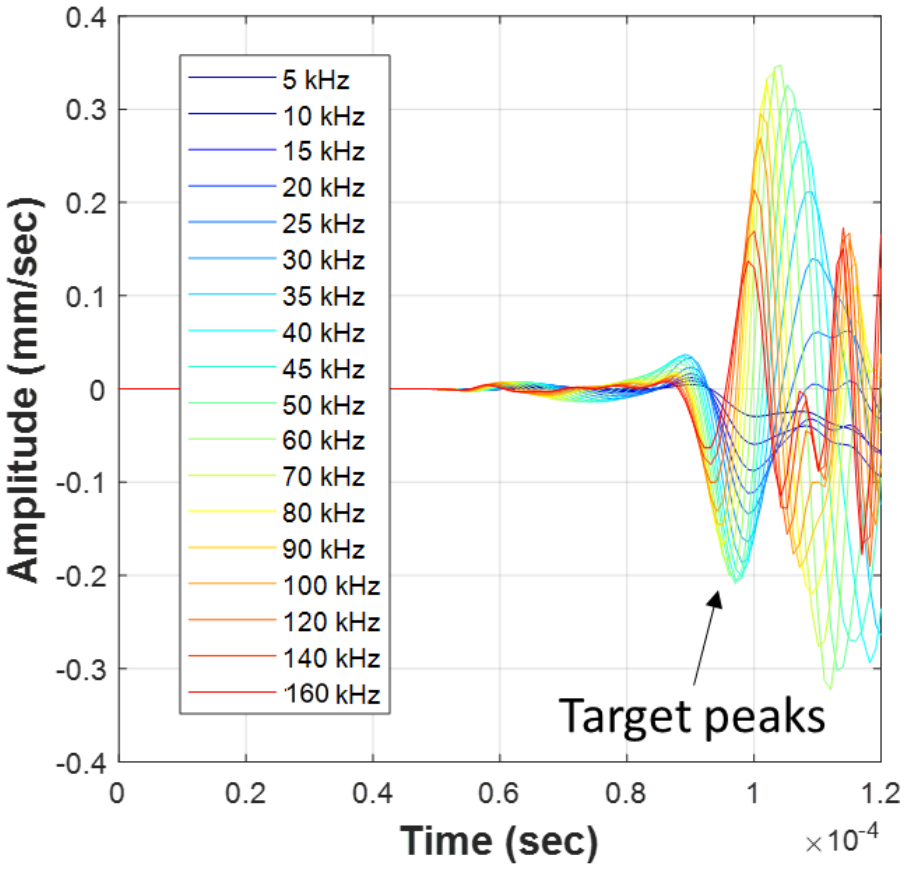
Amplitude (mm/sec)
Time (sec)
×10^-4
5 kHz
10 kHz
15 kHz
20 kHz
25 kHz
30 kHz
35 kHz
40 kHz
45 kHz
50 kHz
60 kHz
70 kHz
80 kHz
90 kHz
100 kHz
120 kHz
140 kHz
160 kHz
Target peaks

(b)

Figure 4.2. FE simulation details and waveforms: (a) 5 cm cracked concrete pipe model and (b) FE simulation results by different wave frequencies, 5, 10, 15, 20, 25, 30, 35, 40, 45, 50, 60, 70, 80, 90, 100, 120, 140, and 160 kHz. The artificial vertical crack is invisible in terms of the surface of input excitation and receives. First negative pecks of surface waves are considered for the calculation of the response ratio.

4.5 Experiments

A concrete pipe sample with a diameter of 61 cm (24 in) and a thickness of 7.5 cm (3 in) is prepared for experiments. Multiple cracks are formed in the concrete sample by performing a structural test called a three-edged bearing test or D-load test. The test applies distributed line loads along the longitudinal direction of a pipe (Park et al. 2014). From the loading test, two types of cracks are formed: inner surface cracks, which represent surface-opening cracks, and outer surface cracks, representing internal cracks because only the inner surface is accessible in the field test. In this paper, we focus on internal crack detection. A scanning system is developed and deployed to monitor these cracks accessed on the inner surface of the pipe. The fundamental concept and testing configuration are described in Figure 4.3. The testing configuration is designed to provide and obtain consistent mechanical wave composing of the auto-impactor, sensor array, and a digital data acquisition system (NI USB-6366, Austin, TX, USA).

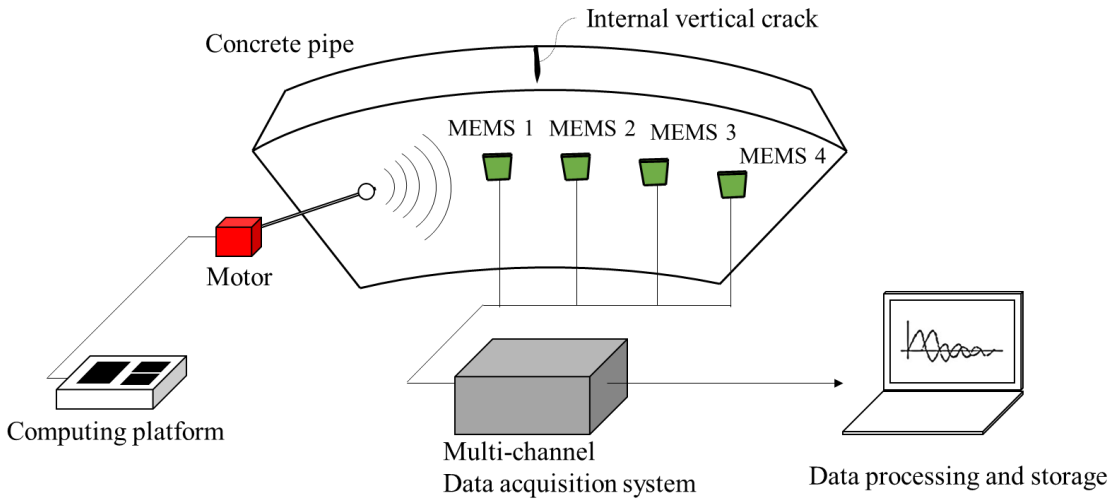

Figure 4.3. Testing configuration for SWS-IVC detection. The auto-impactor is described in Figure 4.4 in detail.

The developed scanning system composes an auto-impacting system, sensors, wheels, and shock absorbers, as shown in Figure 4.4 (a). The shock absorber and wheels are designed to provide consistent distances between sensors and the concrete surface (lift-off distance), of which the diameter is slightly changed within ± 5 cm. The auto-impacting system operated by a DC motor is designed to generate consistent and maximized mechanical wave amplitude in the inhomogeneous medium. Impacting motions by DC motor are described in Figure 4.4 (b). The DC motor generates impact with more than 180 degrees of rotation and 1000 RPM speed, providing a double-sided bounce impacting system. It should be understood this system is called double-sided because the impactor shape in Figure 4.4 (a) can be swung from one side to the other using a DC motor, and then back again. The 3-D image of Figure 4.4 (b) illustrates the double-sided nature of the impact system. The impactor allows to switch back and forth around a common rotational axis at least partly by bouncing the impactor against the underlying surface and utilizing the rebounding force to change the direction of movement of the impactor. The advantages of the system are providing high impact force to increase a signal to noise ratio on inhomogeneous concrete and allowing a rapid and consistent pulse repetition rate (PRR) for high-speed inspection. The impacting ball is designed with a 12 mm low-carbon steel ball and high elastic stainless-steel wire, preventing additional resonance frequency noises.

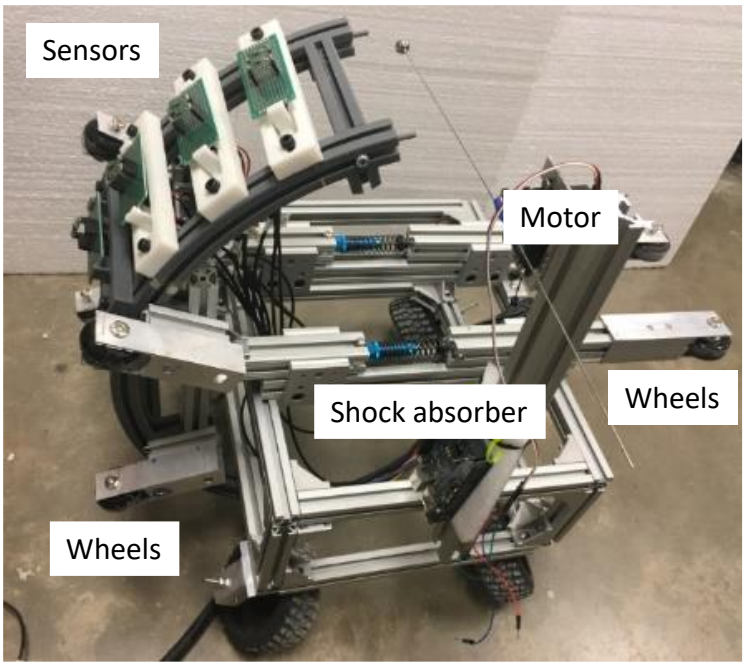

(a)

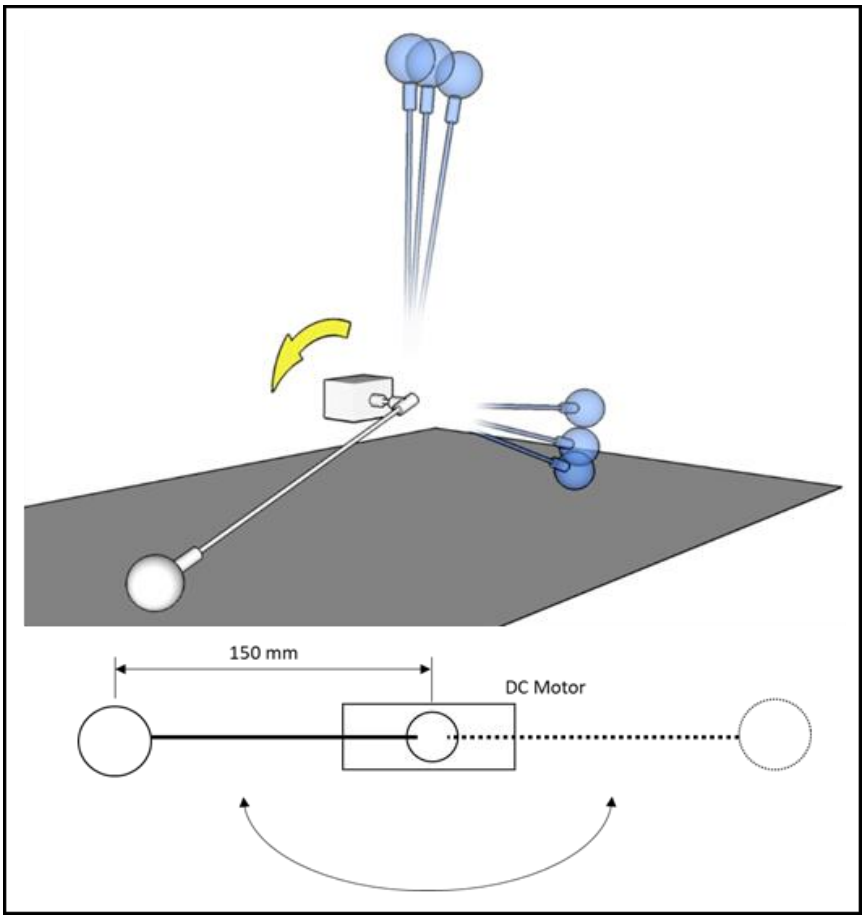

(b)

Figure 4.4. Developed scanning system: (a) perspective view of the scanning body, and (b) illustration of the double-sided bounce impacting system from the side view. The developed inspection system consists of an auto-impacting system, sensors, wheels, and shock absorbers. The impacting motion of the DC motor shows a large radius of rotation and long rotational trajectory. It allows to generate a strong impact in order to obtain high amplitude mechanical waves in the heterogeneous medium.

In this experiment, a surface wave is induced in the concrete samples with a low-frequency (10 to 20 kHz) mechanical wave source operating by the proposed automatic impactors. Non-contact MEMSs located 10 mm above the concrete surface are used to detect leaky Rayleigh waves emanating from concrete (Ham et al. 2017; Ham and Popovics 2015b). The potential of contactless MEMS sensors for reliable wave amplitude (attenuation) measurements is free from sensor coupling and surface condition variations that are expected with contact sensors (Ham and Popovics 2015a). Thus, it allows to perform rapid scanning and to provide a reliable amplitude of obtained signals. The experimental results provide the response variations with various testing protocols. Four MEMS are deployed to detect the surface wave: one sensor (MEMS 1) is placed before the crack from the impacting point and the other three sensors (MEMS 2 – MEMS 4) are placed after the crack every 11 cm described in Figure 4.5. Thus, the incident waves are obtained from MEMS 1, while forward scattering waves are obtained from MEMS 2, 3, and 4. To obtain the response variations, the Set 1 experiment shown in Figure 4.5 (a), which presents a wave excitation location at T4, is conducted first. Ultimately, the obtained experimental response variations are used to compare with the response variation curves from the analytical model and FE simulation of SWS-IVC leveraging correlation coefficients.

In this study, another test, Set 2, is conducted with a different wave sending and receiving location, as shown in Figure 4.5 (b). These two symmetry tests provide the same wave propagation distance between the excitation point and crack, but investigate different wave directions across the crack and different receiving positions. These tests are designed to check repeatability and verify the influence of obtained response variation curve with different wave propagation directions. The experimental data set is obtained from ten different scanning positions in the transverse direction and ten different scanning positions along

the pipe's longitudinal direction where have different depth-to-cracks, as shown in Figure 4.5 (c). Five repeated measurements are conducted for each set. Thus, a total of 100 data points are obtained with two testing setups (two sets × ten depth-to-cracks × five repeated measurements and collections).

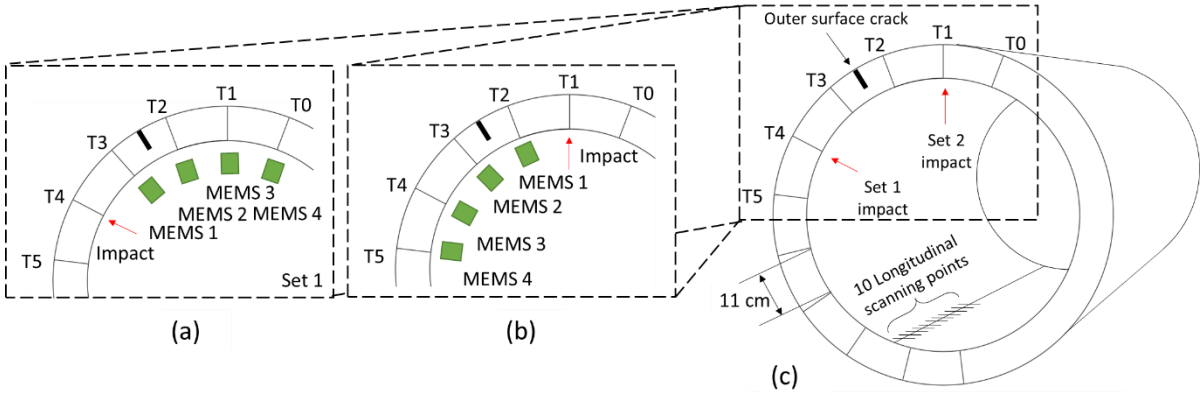

Figure 4.5. Testing configurations providing sensor and impacting position: (a) Set 1 configuration, (b) Set 2 configuration of the SWS-IVC experiment, (c) details of longitudinal scanning points. The prepared concrete sample has the internal vertical crack in between T2 and T3 points. Two testing configurations are designed with the same distance between wave excitation point and crack but with an opposite wave direction to the crack.

A preliminary test is conducted on the non-cracked or intact region to understand the mechanical wave propagation without cracks. Preliminary test results present in Figure 4.6. The results show the typical attenuation behavior on a concrete sample in heterogeneity, as shown in Figure 4.6 (a). Figure 4.6 (b) shows results for estimated surface wave speed obtained from MEMS 1 to 4. The first peaks of each surface wave show reliable results with the consistent result of 2083 m/s. The obtained wave velocity is also within the typical surface wave velocity range on concrete.

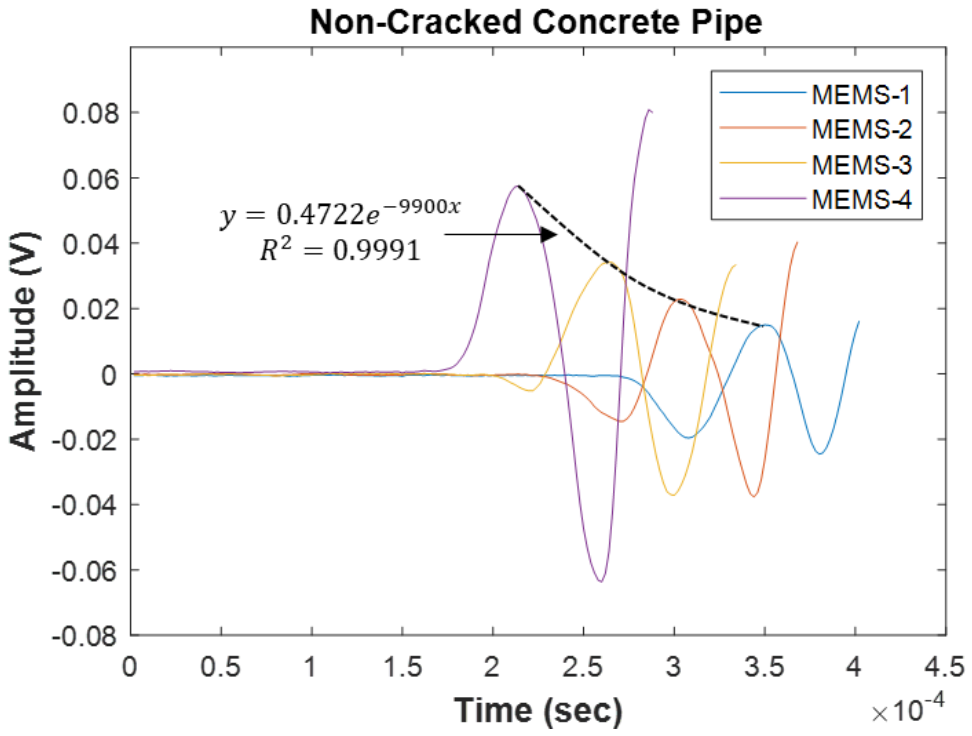
Non-Cracked Concrete Pipe
MEMS-1
MEMS-2
MEMS-3
MEMS-4
$y = 0.4722e^{-9900x}$
$R^2 = 0.9991$
Amplitude (V)
0.08
0.06
0.04
0.02
0
-0.02
-0.04
-0.06
-0.08
0
0.5
1
1.5
2
2.5
3
3.5
4
4.5
Time (sec)
$\times 10^{-4}$

(a)

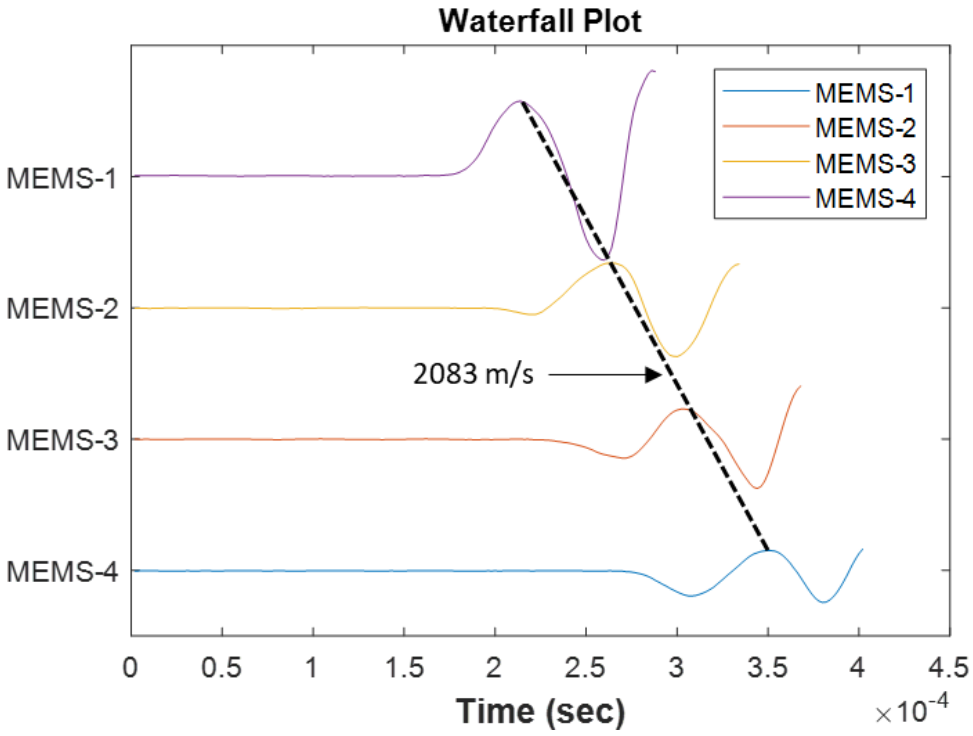
Waterfall Plot
MEMS-1
MEMS-2
MEMS-3
MEMS-4
MEMS-1
MEMS-2
MEMS-3
MEMS-4
2083 m/s
0
0.5
1
1.5
2
2.5
3
3.5
4
4.5
Time (sec)
$\times 10^{-4}$

(b)

Figure 4.6. Detected waves from the MEMS array on the intact region: (a) detected waveforms and the exponential regression curve of first peaks and (b) waterfall plot and the linear connecting line of the peaks with the estimated wave velocity. The result implies that the concrete pipe sample shows typical concrete attenuation by propagating distance.

Ultimately, the results and finds allow to advance developing new crack detection approach based on the response variation leveraging the analytical SWS-IVC model so-called response variation-based analysis (RVA). In general, energy attenuation approaches by cracks have been used to evaluate cracks (Ham et al. 2017). Thus, an additional signal processing will be performed to estimate the relative energy attenuation tendency varied by depth-to-crack. For practical in-situ evaluation, multiple sensors are used to compute the relative energy attenuation so-called multi-sensor-based attenuation analysis (MSA). The result will provide the attenuated wave energy by calculating the relative loss of wave energy between two adjacent MEMS sensors. The response variation in RVA will be discussed and compared with the MSA results. The wave energy (E) is calculated by the sum of time windowed signal as expressed:

$$E_n = \int_{c_1}^{c_2} (S)dx = \left| \frac{c_2 - c_1}{2N} \sum_{i=1}^{N-1} (S_i) + (S_{i+1}) \right| \quad (4.3)$$

where E_n is wave energy of n^{th} MEMS; S_i is wave amplitude at i^{th} data point; c_1 and c_2 are first data point and end data point in the designed time window. The energy loss (EL) between two adjacent sensors is obtained by the percentage decrease calculation as:

$$EL_n = \frac{E_n - E_{n+1}}{E_n} \times 100 \quad (4.4)$$

4.6 Result and discussion

Figure 4.7. shows for three different sensor locations with response variation curves from dynamic FE simulation data. A fixed depth-to-crack, a of 2.5 cm, is used for the simulation data of SWS-IVC. The response variation curves are calculated as the ratio of the first negative peaks of forward scattering surface

waves to incident waves with different frequency inputs. In a previous study, Kang et al. (2020) already validated the simulation result of SWS-IVC under different crack geometry through an analytical solution. As described in Section 4.4, each node location is illustrated in Figure 4.2 (a), including Node 1 for capturing the incident wave signal and Node 2, 3, and 4 for obtaining the forward scattering wave signal. Among the results from the three different receiving nodes, overall, Node 3's response presents the most relevant result to analyze the wave scattering behavior. In general, wave response can be influenced by a spatial location of receiving node, wave velocity, incident wave frequency, and geometrical boundary. For example, the Node 2 location is too close to the crack. Forward scattering wave is not sufficiently and clearly obtained due to the low-frequency transmitting wave (i.e., long wavelength). In addition, considering the pipe geometry and thickness, the location of Node 4 is subject to obtain multiple wave reflections due to boundary conditions. Thus, to obtain proper surface scattering signals, the response variation curve from Node 3 is utilized to compare the results from FE simulation and the analytical SWS-IVC model.

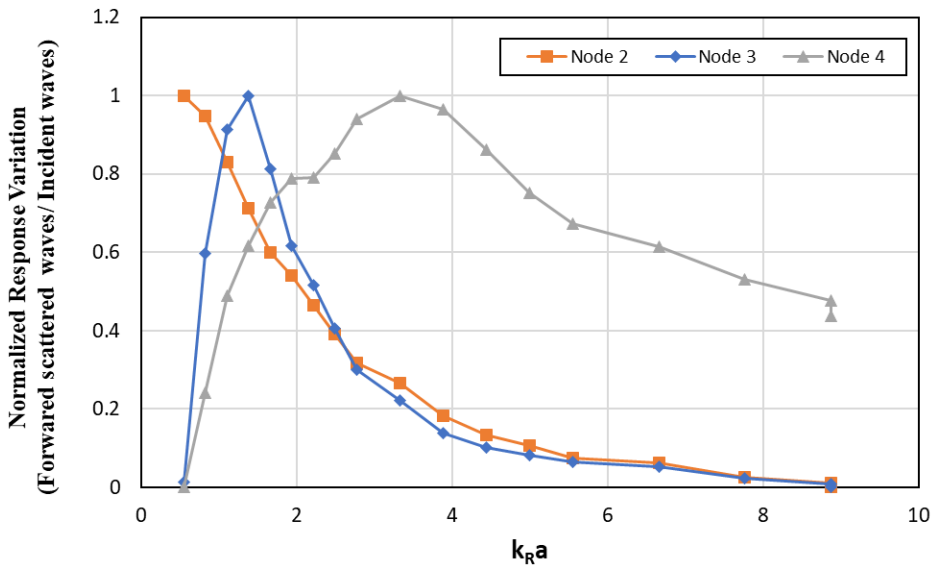

Figure 4.7. FE simulation results from 3 nodes in the forward direction by the crack. The result implies Node 3 shows clear amplitude change by the change of incident wave frequency.

In the analytical SWS-IVC model, to construct response variation curves with respect to $k_R a$, the key parameters, 2.5 cm of a and 18 different incident wave frequencies, are selected. Five different numerical integration methods (Kang et al. 2020) are used to solve the singular integral equation of the analytical model as described in section 4.3. The obtained analytical response variations of five different integration methods and FE simulation results are shown in Figure 4.8. To identify the highest correlated integration solution, multiple correlation coefficients are computed for a pair of a data set. Four response variation curves from analytical SWS-IVC model solving by different numerical integration methods are validated through a FE simulation result. The final calculations of multiple correlations are provided in Table 4.1. The Gauss–Legendre quadrature integration method shows the highest correlation coefficient values of 0.97 compared to all considered models. This result accords with the conclusion by Kang et al. (2020). Thus, the analytical solution using Gauss-Legendre quadrature is considered as the result representing the analytical SWS-IVC model. Furthermore, the analytical solution using the Gauss-Legendre quadrature method shows the lowest MAE as 0.058.

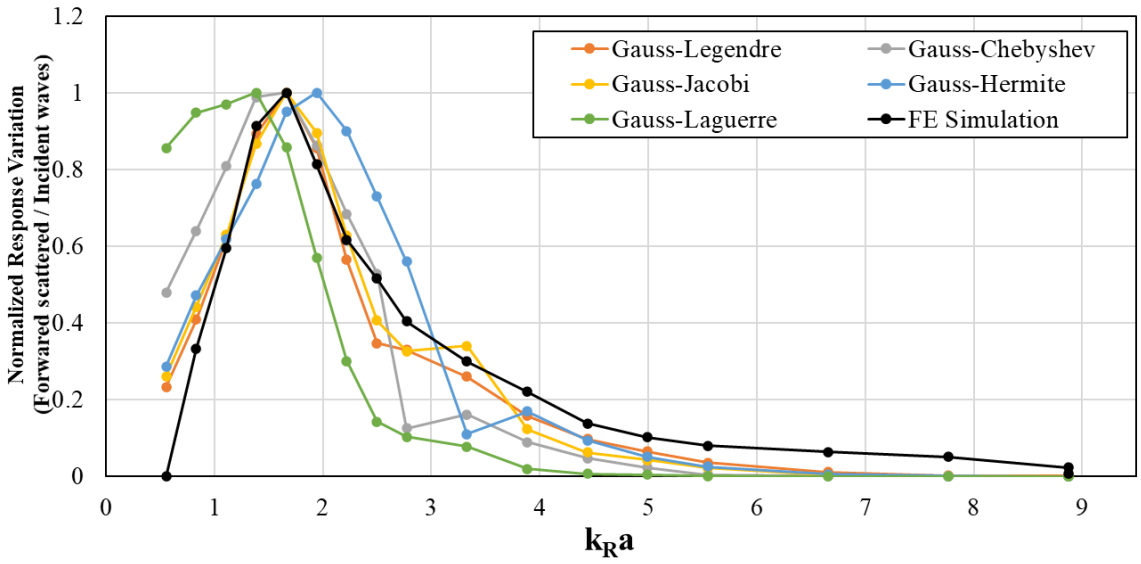

Figure 4.8. Normalized response variation curve of FE simulation and analytical solutions. It indicates that the analytical model and FE simulation results show a similar tendency of response variation influenced by the incident wave frequency changes.

Table 4.1. Correlation coefficients and MAE of FE simulation and Analytical solutions

	FE simulation	Gauss-Legendre	Gauss-Chebyshev	Gauss-Jacobi	Gauss-Hermite	Gauss-Laguerre
Correlation Coefficient	1.0000	0.9700	0.8911	0.9645	0.9244	0.6331
MAE	0	0.058	0.119	0.067	0.112	0.232

Overall, we explore experimental response variation results influenced by various actual cracks and compare them with analytical results. In the first experiment described in Section 2.3, the ratio of a forward transmission wave first positive peak to an incident wave first positive peak is computed. The forward transmission wave and incident wave are obtained from MEMS 3 and MEMS 1, respectively, as illustrated in Figure 4.6 (a). The selection of the MEMS 3 sensor for the forward scattering wave detection is based on the FE simulation result from Figure 4.7. Five repeated measurements of scanning ten different regions along the longitudinal are presented by boxplots shown in Figure 4.9 (a). The height of the blue box indicates the range of values within which 75% of the data are contained, the red bar median value, the point mean value, and the end bars extreme value. Each box plot represents results from five signals at different crack depths. Each longitudinal data point has a different crack depth which is measured by 0.2~3 mm steel wire validated through actual crack depth in the cutting sample. Thus, the response variation is observed to change with different depth-to-crack, a. The overall short length of boxes indicates that the five repeated measurements present a considerable agreement regardless of crack geometry at each testing location. Thus, the response variation curve of the averaged value (note the solid line in black on the box plot) can be used as experimental data.

Figure 4.9 (a) and (b) shows averaged experimental response variation curves from two symmetric testing setups, Set 1 and Set 2 (illustrated in Figure 4.6 (b)). The correlation coefficient of 0.8556 is calculated between Se1 and Set 2 results. The correlation result indicates that both the response variation and the scattered waves obtained from two different receiving positions have a similarity. In addition, the

experiment results imply consistent response variation under various crack geometry conditions regardless of wave path (different receiving point but the same distance between sending and receiving point. Consequently, from the symmetric SWS-IVC experimental result, we observe reliable experimental data with repeatability and consistency to present the internal crack corresponding to proper wave scattering behavior.

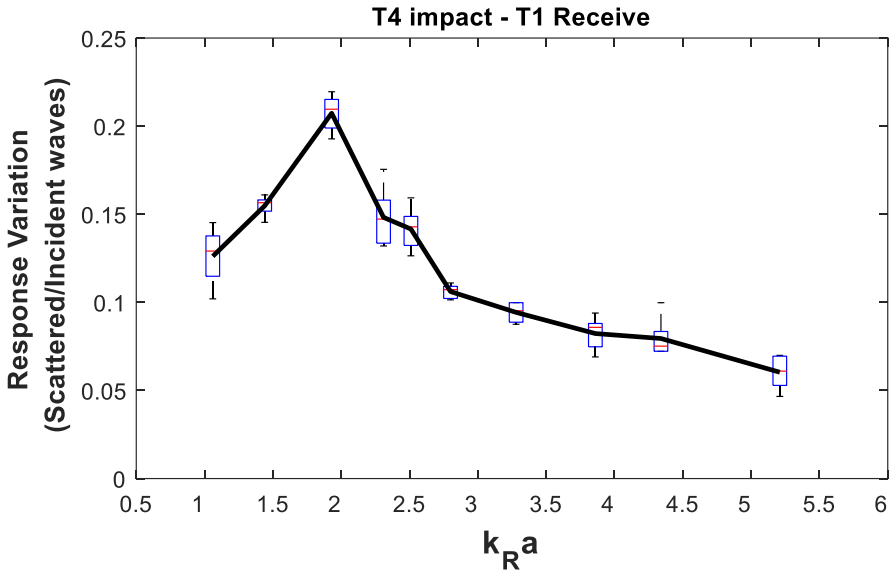

(a)

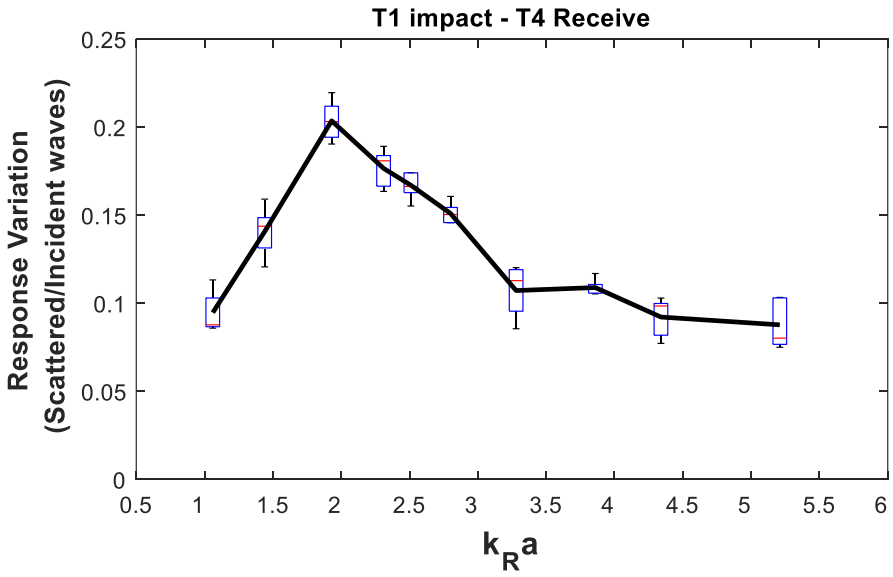

(b)

Figure 4.9. Symmetric experimental results with unique response variations of forward scattering wave: (a) experiment result of Set 1 (impacting at T4 and receiving T1) and (b) experiment result of Set 2 (impacting at T1 and receiving T4). Solid lines indicate the averaged response variation from five repeated experiments. The results show the consistent SWS-IVC behavior toward in-situ monitoring.

Figure 4.10 presents the final response variation curve verification obtained from the analytical solutions, FE simulations, and experiments. Experiment results present with ten data points obtained by randomly

scanning on ten different regions that have various depth-to-cracks. Analytical solution and FE simulation shows 18 data points obtained by 18 different k_R. Thus, the data points of experiment results in $k_R a$ are slightly different from the analytical solution and FE simulation data points. All response variation curves show a similar tendency as shown in Figure 4.10. To check similarity, multiple correlation coefficients are also calculated as described in Table 4.2. Analytical solution and experiment result of Set 1 shows significance correlation, and all cases show highly linear correlation as the criteria for a correlation coefficient (Kang et al. 2020).

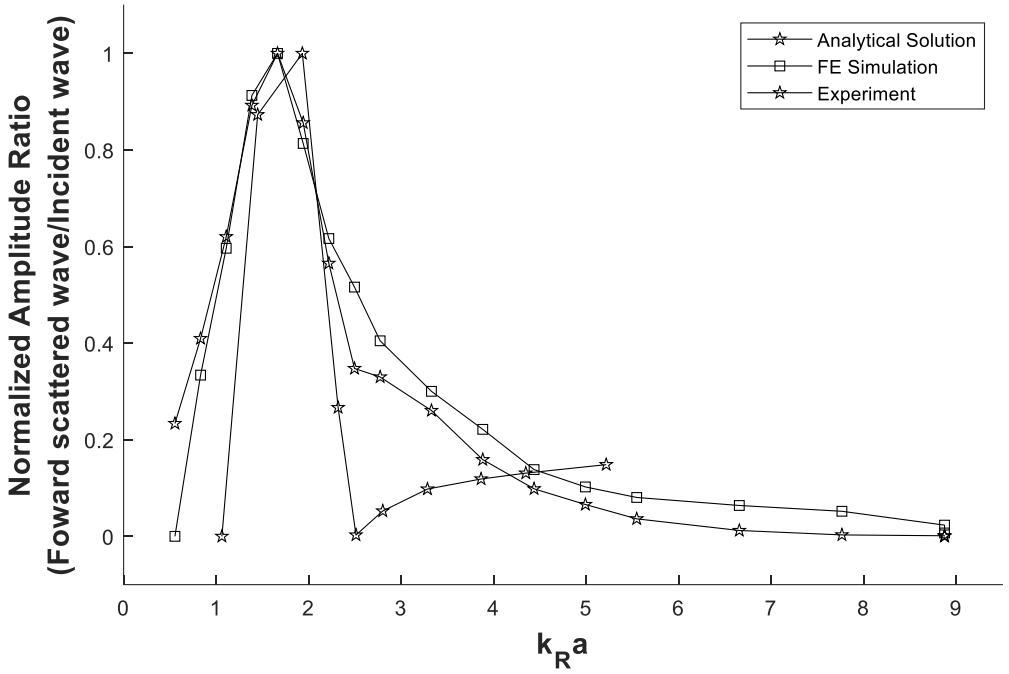

Figure 4.10. All normalized response variation of SWS-IVC from analytical solution, FE simulation result, and experimental results.

Table 4.2. Correlation matrix

	Analytical Solution	FE Simulation Result	Experiment Result
Analytical Solution	1.0000		
FE Simulation Result	0.9700	1.0000	

Experiment Result	0.8968	0.8987	0.8556

Figure 4.11. Present the results of MSA presents. As described in Section 2.3, relative energy loss is computed when a crack is placed between two MEMS sensors. The wave energy is calculated with time period as the duration of (~ 0.34-millisecond) to avoid wave reflection from geometry and the direct acoustic wave in the air. Five repeated measurements of scanning ten different regions along the longitudinal are presented by boxplots shown in Figure 4.11. The solid line indicated the average value of each boxplot. The energy loss, EL shows a clear increasing trend with increasing crack depth or decreasing depth-to-crack, *a*.

It is noted that trends of the response variation curve (velocity variation curve) of SWS-IVC in RVA (see Figure 4.9) do not match and follow with the energy loss tendency in MSA in Figure 4.11. In MSA, we compute the relative energy loss by subtracting the second sensor wave energy from the first sensor wave energy (before the crack). The obtained first wave and second wave include backward and forward scattering for crack, respectively. Despite reasonable trends of energy loss according to crack size, the "relative" energy loss results in MSA do not provide actual crack depth or depth-to-crack. It is hard to provide theoretical relation between relative energy loss and internal geometry. In addition, it is too complicated to remove both forward and backward scattering energy clearly to compute energy loss due to the large wavelength of the low frequency.

On the other hand, in RVA, we demonstrate the theoretical SWS-IVC model representing forward scattering waves corresponding to experimental results. In the model, the forward scattering wave is influenced by the Rayleigh wave effective depth of penetration, incident wave frequency, crack location, and geometry. Based on the analytical SWS-IVC model and experiment result, the RVA method can provide quantified depth-to-crack information.

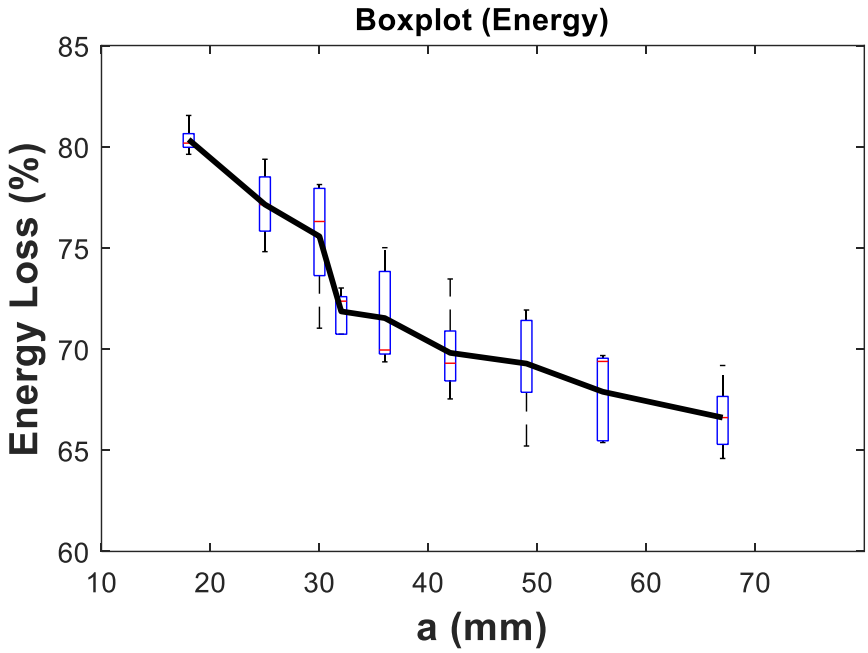

Figure 4.11. A tendency of wave energy loss with respect to a. The energy loss tendency result implies the wave energy decreases as the inverse proportion curve by depth-to-crack , a.

Although the MSA test result does not provide actual crack depth, the result shows decreased wave energy linearly with respect to crack depth, unlike the RVA result. On the other hand, based on Figure 4.10 results, RVA enables to provide absolute amplitude value to estimate depth-to-crack based on the analytical SWS-IVC model. However, use of RVA may have challenges when $k_R a$ are extremely low or high (note the parabolic shape of variation from). Thus, if feasible, MSA may help to evaluate the internal vertical crack by RVA approach leveraging MSA trend. Figure 4.12 presents the conceptual figure for a practical and effective internal crack detection. The proposed approach is used with the variation curve based on the analytical and experimental SWS-IVC measurement in RVA leveraging energy loss tendency in MSA. In this proposed approach, so-called three-point hybrid method, there are three steps: experiment, patternation, and matching/estimation.

- In Step 1, experimental measurements are conducted to obtain the wave response of SWS-IVC at least three different locations in possible damaged areas presenting large energy loss (EL). EL and response variation (RV) values are calculated.
- In Step 2, the calculated values are plotted in the EL-RV graph. By three data points, three patterns are classified (from Pattern 1 to Pattern 3).
- In Step 3, based on the EL-RV graph pattern, the region of interest can be defined (note red dashed are). The actual depth-to-crack can be chosen from the matched depth-to-crack with experimental RV to the analytical solution of RVA. (e.g., a_{P1-A}, a_{P1-B}, a_{P1-C} from Pattern 1 process)

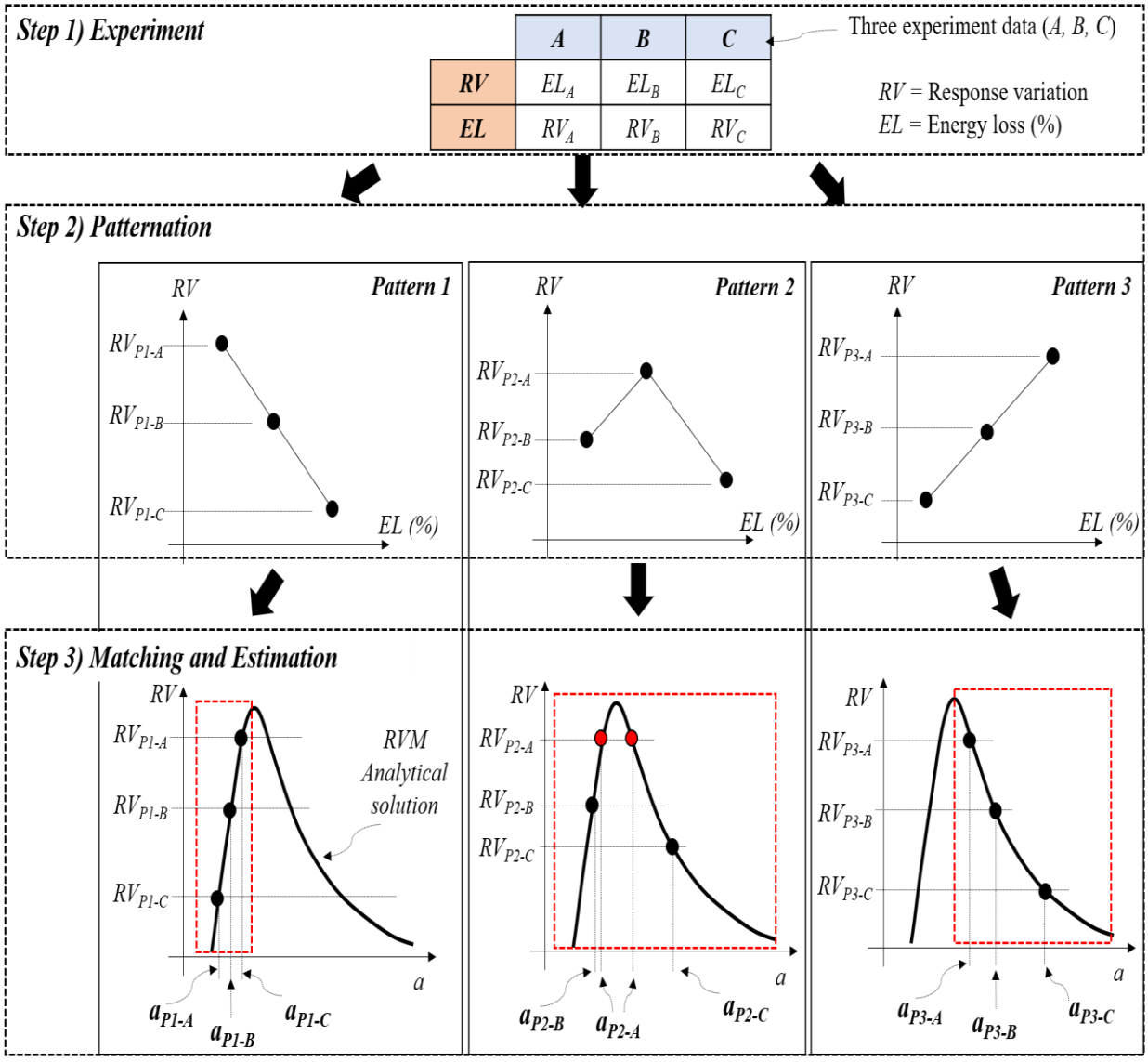

Figure 4.12. A conceptual process for detecting the internal vertical crack. The depth-to-cracks are estimated through three steps.

Since the analytical solution does not consider the wave energy attenuation by the heterogeneity of medium, the supplementary factor between the analytical solution and experiment response variation curves can improve the analytical solution to have the unique model for the specific case of the SWS-IVC. Thus, further study of the supplementary factors for the analytical model can be performed to improve the RAV crack evaluation.

CHAPTER 5 CONCRETE STRUCTURE SCANNING SYSTEM

5.1 Motivation

National Bridge Inspection program regulations require States to inspect highway bridges persistently. Bridges are critical components of transportation infrastructure. Bridge decks, in particular, are the most susceptible components in a bridge due to the direct exposure to traffic and environmental factors (e.g., snow, rain). Their service life is commonly shorter than other components. Thus, monitoring the degree of deterioration of bridge decks is important for determining appropriate maintenance and rehabilitation strategies.

The most severe problem in bridge monitoring is internal damages such as delamination. Delamination is an internal horizontal crack, mainly caused by corroded steel reinforcements. Generally, reinforcement corrosion in bridge decks occurs due to environmental conditions such as migrated moisture and chemical reactions (e.g., chloride ions). The formation of the corrosion products causes volume expansion of the reinforcement. Eventually, the delamination is formed due to the mechanism. In addition, the produced delamination causes the vertical cracks extended from the delamination to rise to the surface. Increased number of or levels of vertical crack damage even accelerate the corrosion process. The further degradation (e.g., potholes) can be caused by these negative interactions among delamination, vertical crack, and reinforcement corrosion with external factors (e.g., traffic load, freeze-thaw cycle) (Hendricks et al. 2020). The produced degradations (e.g., potholes) due to delamination are critical for the roadway safety and the service life of bridge decks (Tsai and Chatterjee 2018). Therefore, the delamination monitoring of vertical cracks and corroded reinforcement is significant to maintaining the bridge deck in the early-stage deterioration.

Detection of the bridge deck delamination has been studied for several decades. Unfortunately, delamination is invisible unless potholes or significant vertical cracks present. Thus, visual inspections to

identify the delamination are challenging. Core extraction – a destructive test – can identify the delamination, but it may cause damages on the bridge deck (Oh et al. 2013). Nondestructive testing (NDT) techniques have been developed to detect these damages. Among them, flexural vibration modes (e.g., chain dragging, hammer sounding, impact-echo) have been widely utilized to identify the delamination. In particular, the application of air-coupled sensors has gained attention to improve the impact-echo approach (Guthrie et al. 2019; Ham and Popovics 2015a; Kee et al. 2020; Scherr and Grosse 2020; Zhu and Popovics 2007). Consequently, advanced impact-echo techniques using flexural vibration mode and air-coupled sensing have been studied and utilized toward efficient detection by exploring various mechanical wave excitation, collection, and interpretation: ice sphere impact (Mazzeo et al. 2014), chain drag data collection from micro-electromechanical systems (MEMSs) (Sun et al. 2018b), deep learning model analysis (Dorafshan and Azari 2020)).

For vertical crack detection, Rayleigh mechanical wave, which utilizes pulse propagation characteristics such as wave velocity or attenuation, has demonstrated sensitivity to cracks (Ji et al. 2019; Li et al. 2020; Wang et al. 2020). The surface wave is propagated along the concrete with the effective depth of penetration. This depth is approximately defined as half the wavelength (Xia et al. 2004). Thus, the surface wave is affected by both surface-opening and internal crack in a certain range of the incident wavelength. The attenuated wave energy is estimated from the difference of wave responses (e.g., maximum amplitude, time-windowed wave energy, spectral magnitude from two receivers placed on either side of a vertical crack (Aggelis et al. 2011; Kee et al. 2011; Zhu and Popovics 2005).

For the corroded reinforcement detection method, a ground-penetrating radar (GPR) technique is commonly used (Dinh et al. 2019; Robison et al. 2020; Sun et al. 2018a). GPR technique is based on transmitting pulsed electromagnetic (EM) waves into the medium and measuring the reflected EM waves from conductive materials (e.g., steel reinforcement). The EM wave response includes the information of degrees of concrete degradation and reinforcement corrosion.

Significant advances have been achieved from the studies for field detection of these damages, such as the delamination, vertical crack, and reinforcement corrosion detection. Most technologies have been designed to be used on foot in the field, which requires traffic control for lane closures (Larsen et al. 2020; Scherr and Grosse 2020; Sun et al. 2018b). To improve scanning speed, there are several studies, including a rapid bridge scanning system using tire chains for detecting delamination (Hendricks et al. 2020). The proposed scanning system comes with tire chains as the impacting source. Although the study shows promising results with high speed, a chain-based system has some possible challenges due to the nature of chains (e.g., direct acoustic wave in the air between chains, multiple excitations simultaneously, frictions between chains and surface) (Sun et al. 2018a). To overcome these challenges, the ball impacting-based impact echo tests have been studied with continuous bridge scanning (Larsen et al. 2020; Scherr and Grosse 2020). Electric motors and solenoids are utilized for repeatable impacts to generate mechanical waves. Despite these efforts, these scanning speeds are still limited, presenting relatively low pulse repetition frequency (PRF) due to the nature of a typical mechanical impactor. The PRF indicates the number of pulses of a repeating signal (i.e., generating a repeating mechanical wave by an impactor). Important scanning qualities (e.g., data collection resolution, wave energy, and consistent wave source) are influenced by several factors such as PRF, scanner design, wave generator design, and scanning speed. The higher PRF and multi-sensors allow the scanning quality like data collection resolution. Wave energy or wave amplitude can be varied by PRF and design of wave source or generator. The high PRF and proper impactor design provide sufficient impact energy (e.g., high signal-to-noise ratio (SNR)) and high resolution at high speed to detect damage in the heterogeneous medium. The efficient design of wave generator (e.g., automatic impactor) is required to enhance PRF, SNR, consistent source. Unfortunately, there is a lack of study for continuous mechanical wave-based testing (e.g., impact-echo test, surface wave detection) in terms of the auto-impacting and multichannel acoustic scanning system high-speed.

This paper presents work conducted to overcome key technical barriers to automated and traffic disruption-free crack detection implementation in infrastructure elements in the field. In particular, we demonstrate

and advance a practical ACE system. We introduce and optimize an ACE system configuration to identify the damage of delamination, vertical crack, and reinforcement corrosion by developing a high-speed auto-impacting system, integrated scanning platform, multichannel acoustic scanning system for high-resolution data collecting. Impact-echo, surface wave attenuation, and GPR methods are used to detect these defects. The paper provides a description of the development traffic disruption-free ACE system, the post-processing algorithm, the results of field bridge inspection, and conclusions about the implementation of the new ACE system to monitor the bridge deck in the early-stage deterioration.

5.2 Development Traffic Disruption-Free ACE System

The design of the ACE system aims to perform the rapid traffic disruption-free bridge inspection with the integrated scanning platform deploying an advanced impacting system and a multichannel acoustic sensing system to obtain the higher scanning qualities. This section provides the description of an advanced auto-impacting system (double-sided bounce impact system), the design of a multichannel acoustic scanning frame, and the details of an integrated scanning platform (automated height-adjustable platform).

5.2.1 *Advanced Auto-Impacting Technique: Double-Sided Bounce Impact System*

The design of the scanning platform aims to perform the detection at high speed, high IRR with consistent impact motion. Thus, it is important for generating higher impact energy and accurate and reliable wave response which is pure mechanical waves undisturbed by the unintended noise. Thus, a double-sided bounce impacting (DSBI) system is developed as described in Figure 5.1. The DSBI mainly consists of a ball, wire, and motor: 12 mm low-carbon steel ball, high elastic stainless-steel wire, and DC motor, as shown in Figure 5.1 (a). The DC motor generates impact with more than 180 degrees of rotation and 1000 RPM speed, providing a double-sided bounce impacting system. It should be understood that this system is called double-sided because the impactor is swung from one side to the other, in both the clockwise and

counterclockwise direction, as described in Figure 5.1 (a). The 3-D image of Figure 5.1 (b) illustrates the double-sided nature of the impact system. The mechanism causes the impactor to switch back and forth between a left configuration and a right configuration around a common rotational axis, at least partly by bouncing the impactor against the underlying surface and by utilizing the rebounding force to change the direction of movement of the impactor. For example, motor movement is assisted by the bouncing force (or vice versa) or bouncing force is an alternative to actuator movement). Advantages of the system include a wide angle of motion (for generation of a strong impact signal such as a high amplitude mechanical wave) and/or a high rate of impact as the combination of actuator force and bouncing impactor force, instigating movement in the opposite direction of the double-sided system, results in an extremely rapid and consistent IRF. The system provides up to 3-4 impacts/second in operation.

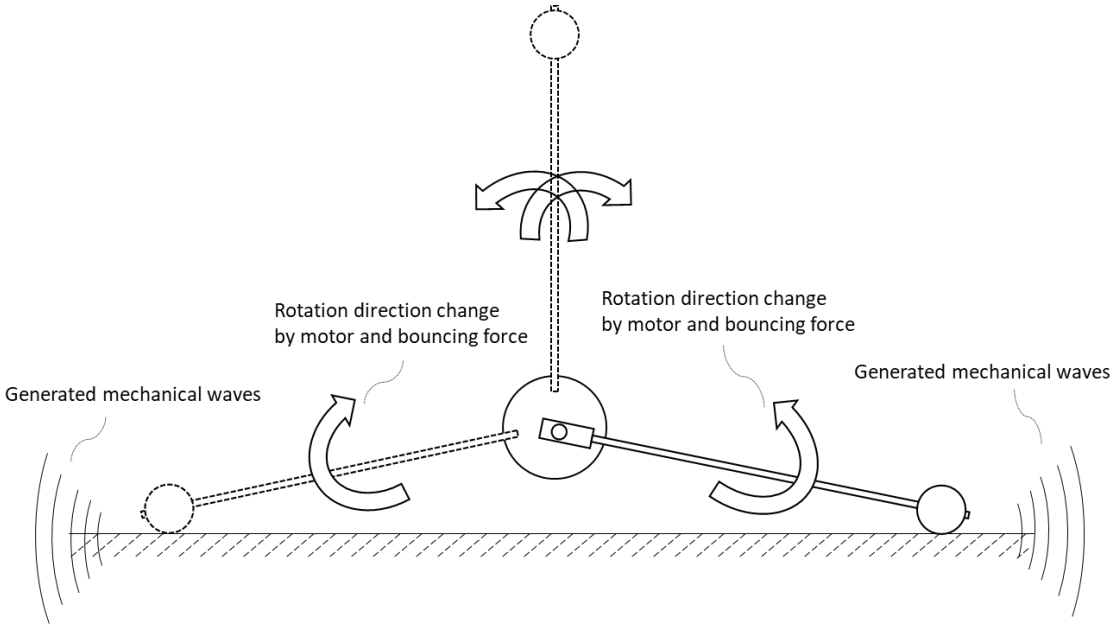

(a)

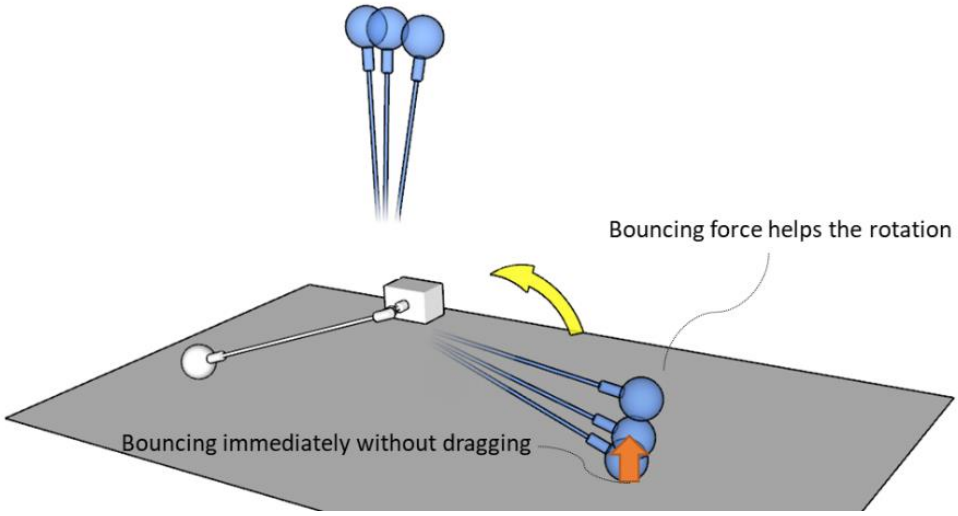

(c)

Figure 5.1. DSBI system: (a) conceptual figure of DSBI system in side-view, and (c) 3-D view of DSBI system. The impacting motion operated by the motor shows more than 180 degrees of rotation and consistent rotational trajectory. The bouncing force of the ball impacting enhances the following impact, which is on the opposite side impact. It allows to generate a strong and consistent impact.

5.2.2 *Multichannel Acoustic Scanning Unit*

The developed DSBI system is deployed to the ACE system to provide the higher incident wave energy and generate constant and higher PRF impact. The deployment of wave generator and receiver is significant along with the DSBI system design to obtain a proper data collection resolution. The higher data collection resolution implies more measurements in unit time and unit area. This section focuses on the deployment design of the DSBI system and MEMS. The deployment design is to provide a higher data collection resolution by using a multichannel acoustic scanning (MAS) unit, including the impactor frame and sensor frame, as illustrated in Figure 5.2. MAS unit deploys 9 DSBI systems and 22 MEMSs with 30 cm and 10 cm spaces, respectively. The 9 DSBI systems operate with a 20 ms time delay to avoid wave interference. The 9 DSBI systems are also installed in zigzag order to avoid interference between the adjacent motors. The three consecutive impacts can be defined ($x_{i,}$ t_i), ($x_{i+1,}$ t_{i+1}), and ($x_{i+2,}$ t_{i+2}) by time (t) and distance (x) with the impact number (i). *IP* is an impacting point, which is the location of MEMS 1, 4, 7, 10, 13, 16, 19, and 22. s_m is section between m^{th} MEMS and $(m+1)^{\text{th}}$ MEMS. The impact point and sections, *IP* and

s, will be used for delamination detection and vertical crack detection and will decide their data collection resolution. Therefore, the data collection resolution in the transverse direction is defined to 30 cm and 10 cm for delamination detection and vertical crack detection, respectively.

The data collection resolution in longitudinal direction depends on the longitudinal position changes of impacts, which is decided by vehicle speed and PRF (note it is constantly defined by DSBI system). The PRF of the one set (9 motors) of the DSBI system in the MAS unit is designed to 3 impacts/sec. The system provides an even faster rate with the additional set of MAS unit. A double-MAS system can allow 6 impacts/second, which indicates 64 km/h (40 mph) speed with 2.8 m longitudinal resolution.

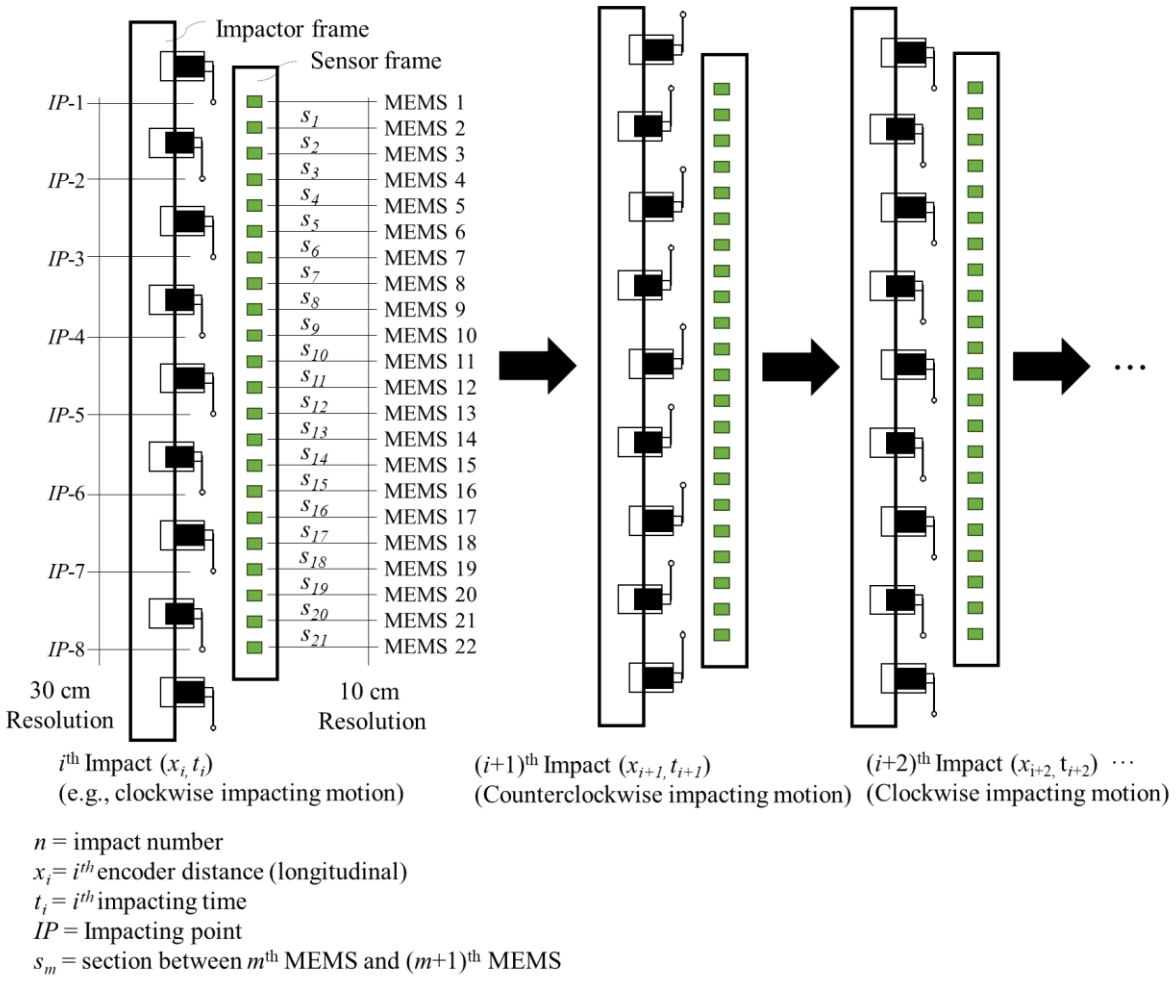

Figure 5.2. Deployment design of MAS unit with three consecutive impacts. The IP and MEMS distance show the 30 cm and 10 cm data collection resolutions in transverse for delamination detection and

vertical crack detection, respectively. Time interval and longitudinal distance, t and x, decide the data collection resolution in the scanning direction.

5.2.3 *Integrated Scanning Platform: Automated Height-Adjustable Scanning Platform*

To perform the rapid traffic disruption-free bridge inspection, the automated height-adjustable scanning (AHAS) platform is developed, as shown in Figure 5.3. The AHAS platform mainly consists of a frame elevation system, DSBI system mounted the MAS unit (impactor frame and sensor frame), GPR antennas, and control box. This AHAS platform can move at highway speed with van type of vehicles.

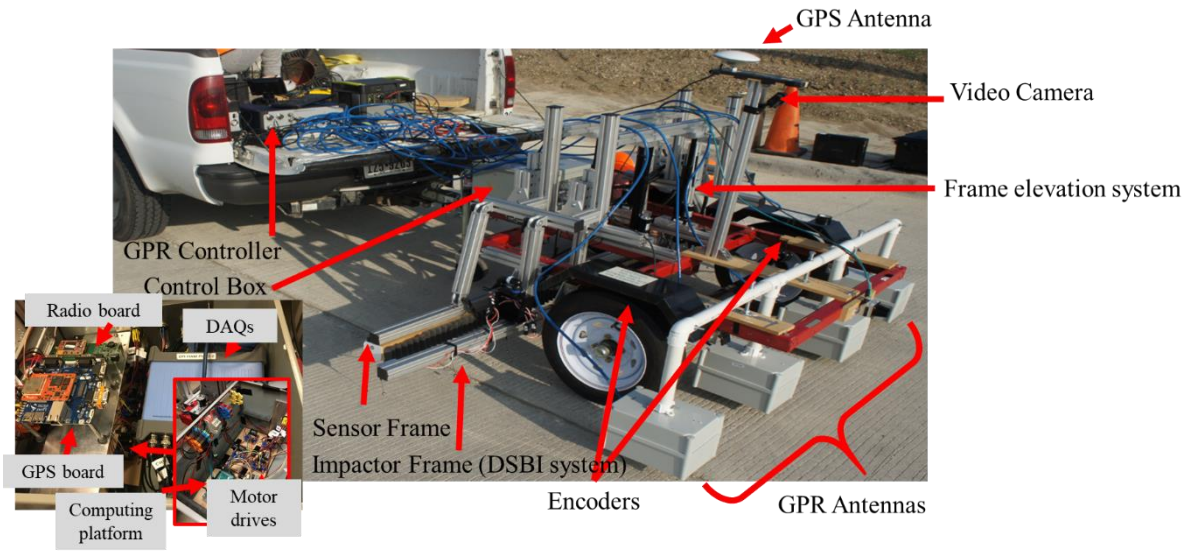

Figure 5.3. Device deployment of AHAS platform with truck and van. The device deployment allows mechanical wave, electromagnetic wave, video image, position data collection simultaneously.

The frame elevation system is designed for the ACE system to perform a nonstop inspection until finish the entire bridge scans (multiple paths or lanes) by controlling the MAS unit at different heights during the bridge scanning and after scanning. The frame elevation system consists of four linear actuators, which are remotely controlled with a 20 cm stroke length and 1 cm/s speed, as shown in Figure 5.4 (a). Figure 5.4 (b) and (c) show the different MAS unit heights before and after bridge scanning (high position) and during the scanning (low position), respectively. The nonstop bridge inspection is described with different start and end times of devices in the repetitive scannings, as shown in Figure 5.4 (d). The frame elevation system is remotely controlled to a lower position before the ACE system reaches the bridge starting point. DSBI

system starts impacting while the MAS unit reaches the lower position. After the MAS unit reaches the lower position, encoders, DAQs, and GPR start collecting data. When the ACE system passes the end of the bridge, DSBI, encoders, DAQs, and GPR stop their operations. The frame elevation system lifts the MAS unit after the scanning devices stop recording data. The ACE system then proceeds to inspect the next lane with the same procedure. The GPS and video camera runs the entire inspection time without interruption. Therefore, the ACE system with the AHAS platform inspects the bridge deck with nonstop and non-delay multiple scanning.

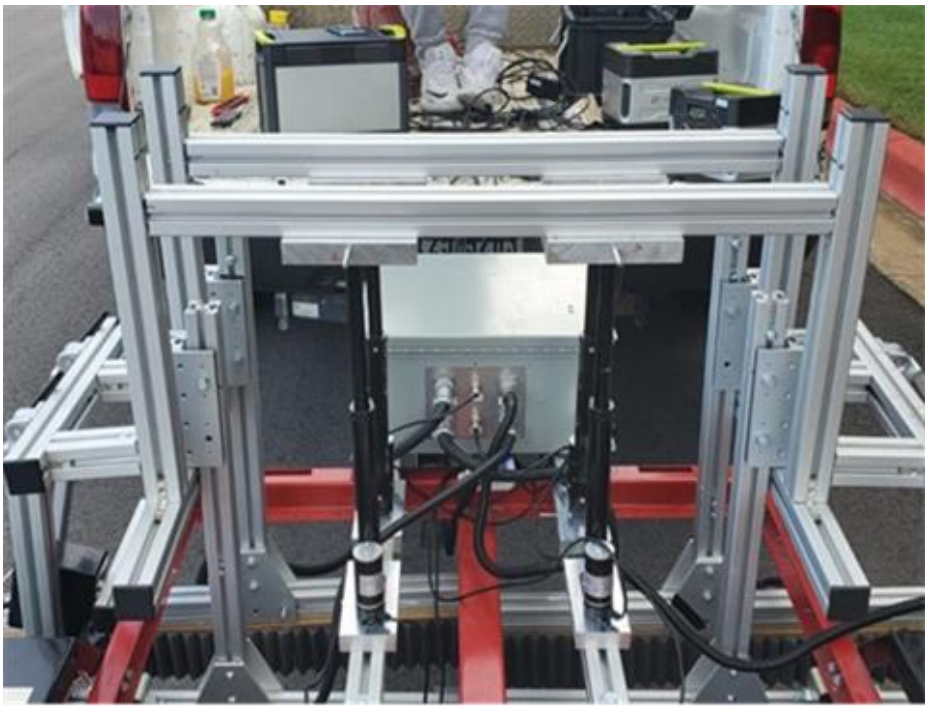

(a)

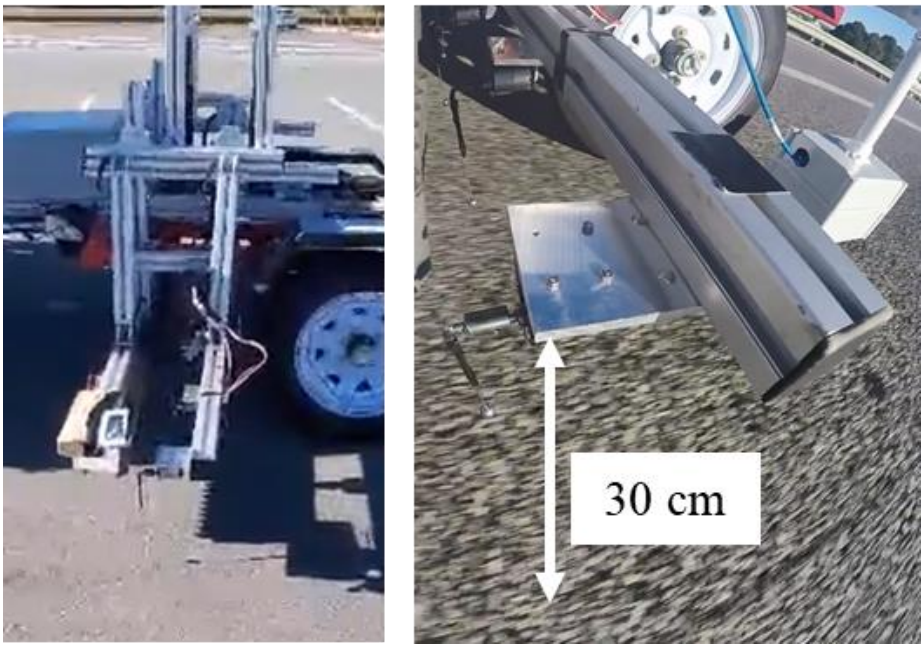

(b)

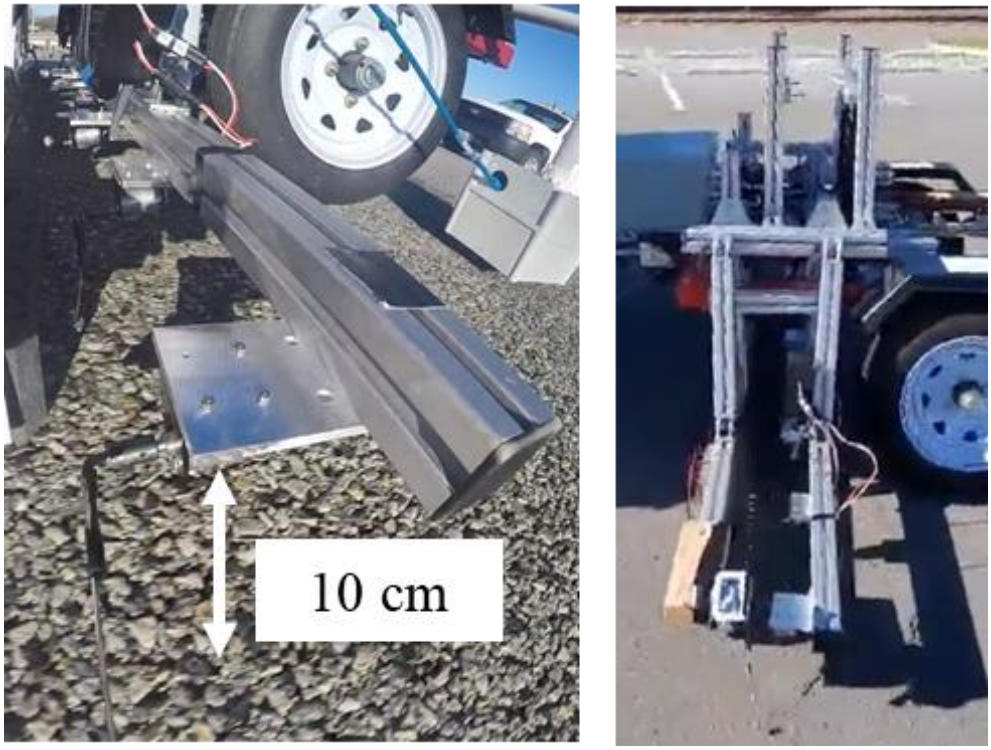

(c)

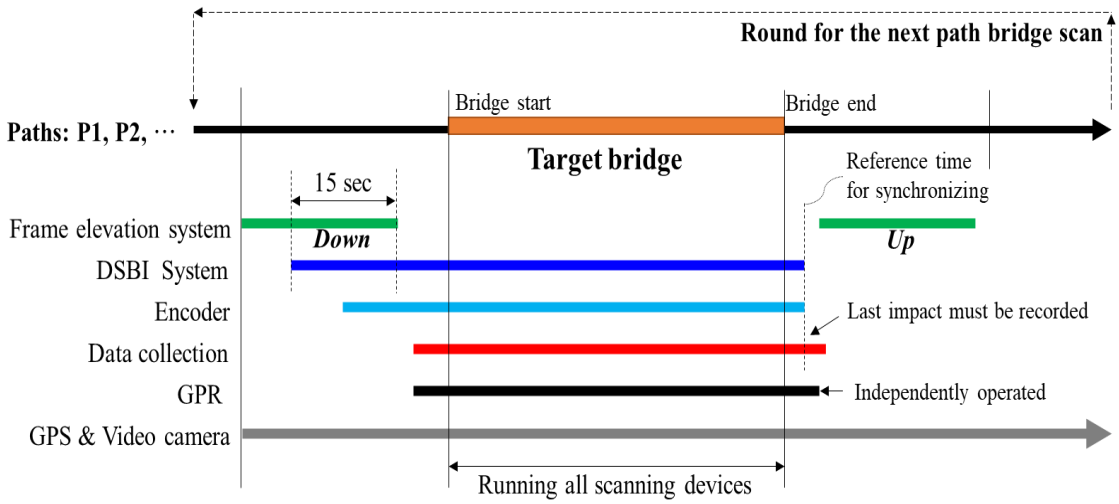

(d)

Figure 5.4. Frame elevation system and scanning procedure: (a) four remotely controlled linear actuators for the frame elevation system, (b) high position of the MAS unit before/after bridge scan, (c) low position of the MAS unit during the bridge scan, (d) multipath bridge scanning procedure in different operation times. Based on this design of inspection procedure, the ACE system can perform the nonstop multipath bridge inspection.

To understand the multiple processes, the system representation diagram is presented in Figure 5.5. The function in the system can classify the processes of the ACE system: wave measuring process, wave generating process, GPR process, and positioning process. In detail, process-1 (green components) consists of a MEMS sensor, DAQs, and laptops to measure the acoustic wave from the bridge deck. process-2 (orange components) consists of a DSBI system including motor, motor drive, and computing platform to generate the mechanical wave on the bridge deck. process-3 (blue components) consists of GPR antennas and a GPR to collect the EM waves. process-4 (gray components) consists of GPS and radio antennas, GPS board, encoder, computing platform, and laptop to record the position of the ACE platform. Real-time kinematic (RTK) GPS provides a centimeter-level accuracy by correcting the position with the reference from the stational base station.

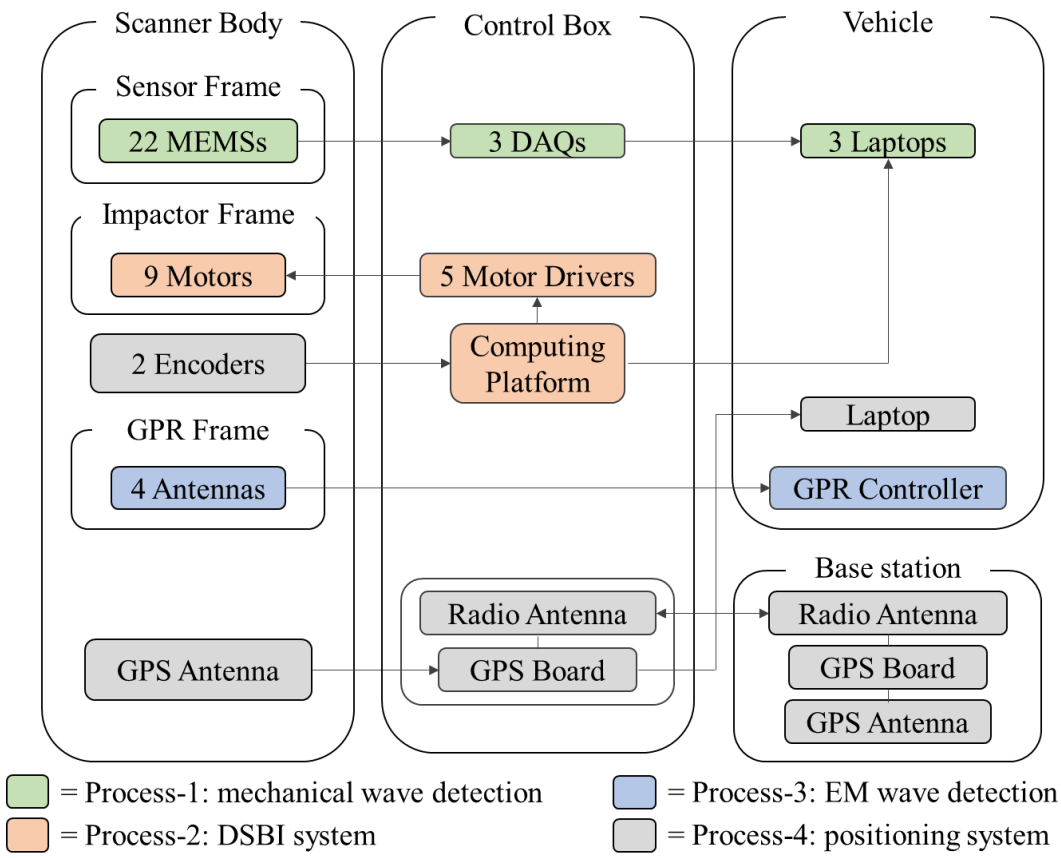

Figure 5.5. System representation diagram of the ACE system. The processes of the ACE system are categorized by the functions and placed locations.

The testing configuration of the ACE system for the delamination and vertical crack detection, which is mainly process-1 and process-2 (see Figure 5.5), is depicted in Figure 5.6. 22 MEMS sensors are deployed in the sound insulation forms. The forms surround the sensor frame to prevent the sound noise from the outside of the frame. The additional form is in between the sensor and frame to reduce the vibration from the frames. The arrows in the testing configuration figure indicate the target acoustic waves for delamination and vertical crack detection. Red and blue arrows represent the surface waves. The green arrow represents the acoustic wave on the delamination. The detailed concept and post-processing procedure from the targe acoustic wave will be introduced in the next section.

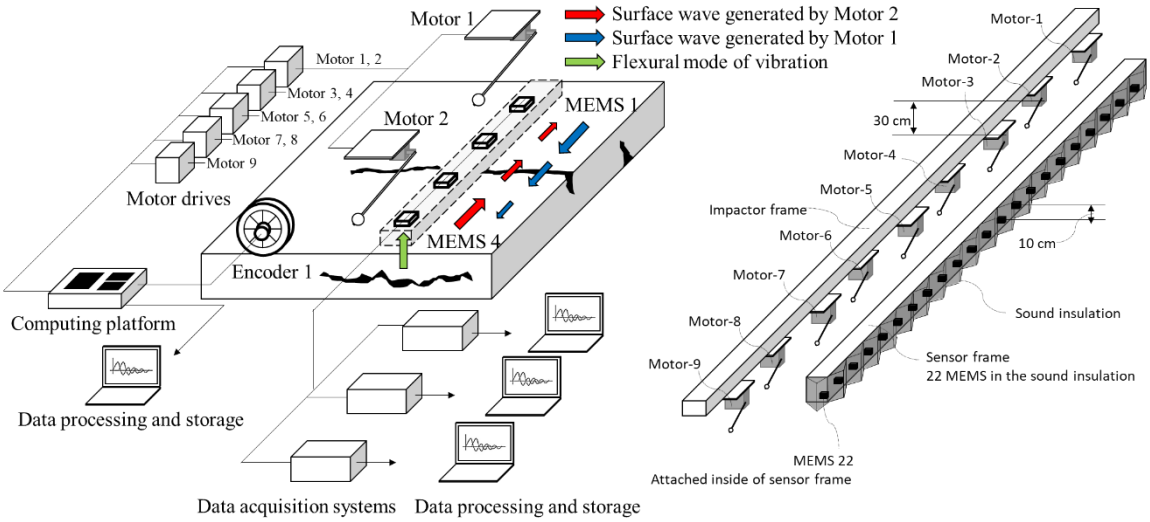

Figure 5.6. Main testing configuration for delamination and vertical crack detection. This testing configuration allows the delamination and vertical crack detection by measuring the target waves (red, blue, and green arrows in the figure)

5.3 Concept and Post-Processing Algorithm of Damage Identification

This section introduces the damage identification concept and algorithm of the ACE system for delamination, vertical crack, and corroded reinforcement. MAS-based and GPR-based detections are addressed with fundamental concepts and post-processing algorithms. The algorithm includes post-

processing procedure, details of data status (e.g., size or format), parameters (e.g., cutoff frequency, processed targe range), and expected outputs.

5.3.1 *MAS-Based Detection for Delamination and Vertical Cracka*

MAS-based detection uses different techniques: impact-echo for delamination detection and surface wave attenuation for vertical crack detection.

Generally, impact-echo tests have two different families of frequency modes: thickness mode and flexural vibration mode. The thickness mode (f_{TM}) is normally dominated when body waves are repetitively reflected between the two parallel boundaries. The thickness mode is commonly used to estimate the thickness (h) of the medium with known longitudinal wave velocity (C_L). In the impact-echo test, the thickness is estimated,

$$h = \beta_1 C_L / 2 f_{TM} \quad (5.1)$$

where $\beta_1$is correction factor (Sansalone and Streett 1997). Thus, the thickness mode of frequency in a typical concrete bridge deck (h = 0.18 m, C_L = 4000m/s, and β_1 = 0.95) is in near 10 kHz.

On the other hand, the flexural vibration mode can present the delamination since it occurs by the out-of-plane vibration of the concrete above delamination. In this study, we will mainly use flexural vibration mode to detect delamination by implementing the impact-echo test. Figure 5.7 depicts the concept of the impact-echo test using ball impact and air-coupled MEMS sensor to measure the flexural vibration mode. MEMS sensor (Ham and Popovics 2015b) is used to measure the leaky wave by using noncontact MAS.

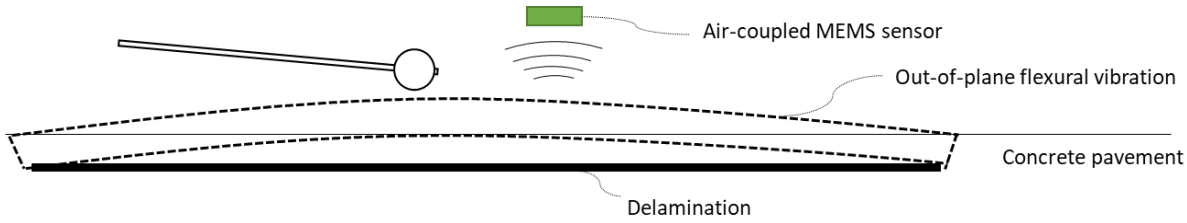

Figure 5.7. Conceptual figure of the flexural vibration in impact-echo testing. The delamination detection can be performed with a single air-coupled sensor (e.g., MEMS sensor) by measuring the flexural vibration.

The details of flexural vibration mode can be explained by the equation of the fundamental flexural vibration mode (f_{FM}) (Leissa 1973):

$$f_{FM} = \frac{k_{DF}^2 \pi}{2h^2} \sqrt{\frac{D}{\rho h'}} \quad (5.2)$$

where k_{DF} is a dimensionless frequency which is determined from the general natural frequencies in terms of the width-to-depth ratio of delamination; h is a depth of delamination; D is flexural rigidity, $D = Eh^3/12(1-\nu^2)$, with Young's modulus (E) and Poisson's ratio (ν), ρ is material density. Based on Eq. (5.2), the flexural vibration mode relies on the geometrical property of k_{DF} and h by given material properties. Thus, the shape of delamination (e.g., width, depth) is the critical factor to determine the frequency of the flexural vibration mode. Since it is hard to specify the frequency of the flexural vibration mode by unknown delamination, many studies use a sum of spectral magnitude, or energy intensity, in a different range (e.g., 1.5 to 3 kHz (Hendricks et al. 2020), 1 to 4 kHz (Larsen et al. 2020), 0.5 to 5 kHz (Kee and Gucunski 2016; Sun et al. 2018a)). Fortunately, the flexural vibration mode in bridge deck delamination presents in a lower frequency range (lesser than 5 kHz) which is distinguishable from thickness mode (higher 10 kHz). In our ACE system, we measure the flexural vibration mode by calculating the energy intensity 1 kHz to 6 kHz frequency range. The energy intensity (*EI*) can be expressed,

$$EI_n(f) = \int_{f_l}^{f_h} \Psi_n(f)\, df = \sum_{i=1}^{N} \Psi_n(f_i)\,,\ (f_1 = f_l, f_N = f_h), \quad (5.3)$$

where $EI_n(f)$ is energy intensity of nth MEMS sensor; $\Psi_n(f)$ is a spectral energy density of n^{th} MEMS sensor, $\Psi_n(f) = |X_n(f)|^2$, with a magnitude of the frequency component ($X_n(f)$); f_l and f_h are the low- and high-boundary frequencies (i.e., 1 kHz and 6 kHz in our system). The spectral signal is obtained by a 4096-point FFT. The obtained *EI* of flexural vibration mode is processed to create a two-dimensional (2-D) scanning image, or 2-D colormap, presenting the delaminations. The 2-D colormap is obtained by interpolating for 2-D matrix (obtained *EI*s) in a spatial meshed grid by *x* and *IP* (see Figure 5.2). All post-processing is performed with MATLAB mathematical computing software (MathWorks, Natick, MA, USA).

The second MAS-based detection technique is the surface wave attenuation for vertical crack detection. The wave attenuation is one of the characteristics of the mechanical wave propagation using the wave response changes by the damage (e.g., vertical cracks). The surface wave attenuation can be obtained from multiple receivers by calculating the wave energy difference between two adjacent receivers. The ACE system uses multiple MEMS sensors to detect the attenuated surface waves, as described in Figure 5.8.

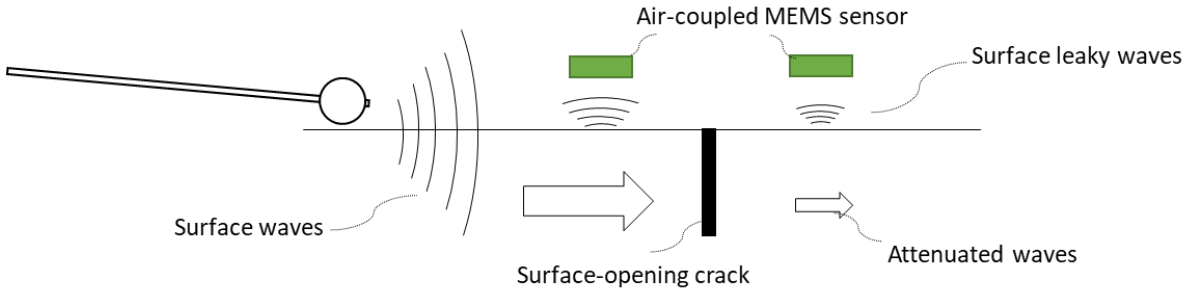

Figure 5.8. Conceptual figure of the wave energy attenuation in multi-sensor-based surface wave detection. The vertical crack can be detected with multiple air-coupled sensors by calculating the attenuated wave energy.

The attenuated wave can be calculated from the wave energies of the adjacent MEMS sensor. The time windowed wave energy of n^{th} MEMS (E_n) can be expressed,

$$E_n(T) = \int_{T_s}^{T_e} w_n(T)^2 \, dT = \sum_{i=1}^{N} w_n(T_i), \qquad (T_1 = T_s, T_N = T_e) \tag{5.4}$$

where $w_n(t)$ is an acoustic signal of n^{th} MEMS; T_s and T_e are start and end of the time window. The wave energy is calculated with time period as the duration of (~ 0.3-millisecond), to avoid wave reflection from geometry and the direct acoustic wave in the air. The attenuated wave energy can be expressed by the percentage decrease equation between two energies calculated from two adjacent MEMS sensors: E_{n1} represents the wave energy of the $n1^{th}$ MEMS sensor from the impacting point; E_{n2} represents the wave energy of the $n2^{th}$ MEMS sensor from the impacting point. The *n1* MEMS should be closer to the IP than *n2* to obtain the positive energy loss value. The attenuated wave energy (EL_{n1-n2}) is expressed,

$$EL_{n1-n2} = (E_{n1} - E_{n2})/E_{n1} \times 100. \tag{5.5}$$

Since the surface roughness, which is a deviation in the direction of the normal vector of the surface, is smaller than the wavelength (note that the wavelength is about 20 cm in 10 kHz incident wave frequency and 2000 m/s wave speed), it can be ignored (Cao and Sendur 2019).

The obtained attenuated wave energy also will be processed to a 2-D colormap, presenting the vertical cracks.

The detailed post-processing algorithm is presented in the flowchart as described in Figure 5.9. Since the prepared DAQs are 8 channel, the 22 MEMS data are collected by three DAQs: DAQ 1 (MEMS 1-8), DAQ 2 (MEMS 8-15), and DAQ 3 (MEMS 15-22). The shared MEMS data (MEMS 8 and MEM 15) between DAQs are to synchronize the acoustic data from three DAQs. Data collecting and storing is processed by LabView software. Data collection is performed with a 0.5 M/s sampling rate in the “streaming” mode of data collection and storing function. The streaming mode is the continuous data collection mode of DAQ by recording and storing it simultaneously to the processer (e.g., laptop). The obtained acoustic data are combined to one matrix data which is inspection time-by-22 channel size. The inspection time is converted to the impact numbers by picking the acoustic impact data. The separated impact data is filtered by a band

pass filter with 0.5 and 20 kHz cutoff frequencies. The processed data is selectively used for creating the colormaps based on the target defect. The post-processing for the delamination detection is performed with the wave response from the MEMS sensor at the impact points, *IP*s, as described in Figure 5.2. For vertical crack detection, wave response from all MEMS sensors is used. The primary process of delamination detection is to present the delamination 2-D interpolated colormap by calculating the sum of the power spectrum as the band energy (1 kHz to 6 kHz band) as described in Figure 5.7. The 2-D colormap of vertical crack detection is presented from the calculated wave attenuation of each section, s_1 to $s_{21,}$ in Figure 5.2.

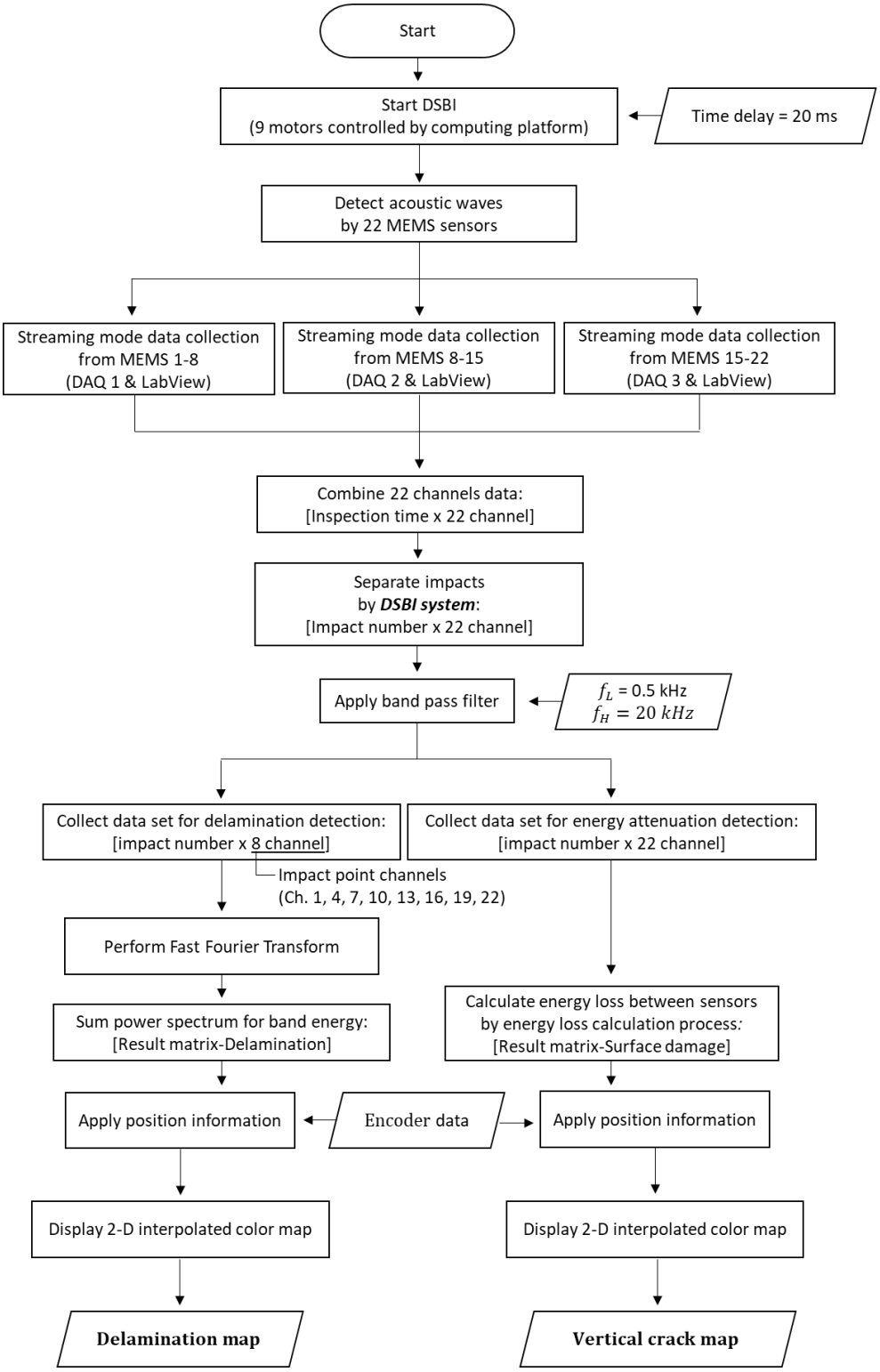
Start
Start DSBI
(9 motors controlled by computing platform)
Time delay = 20 ms
Detect acoustic waves
by 22 MEMS sensors
Streaming mode data collection
from MEMS 1-8
(DAQ 1 & LabView)
Streaming mode data collection
from MEMS 8-15
(DAQ 2 & LabView)
Streaming mode data collection
from MEMS 15-22
(DAQ 3 & LabView)
Combine 22 channels data:
[Inspection time x 22 channel]
Separate impacts
by DSBI system:
[Impact number x 22 channel]
Apply band pass filter
f_L = 0.5 kHz
$f_H = 20\ kHz$
Collect data set for delamination detection:
[impact number x 8 channel]
Collect data set for energy attenuation detection:
[impact number x 22 channel]
Impact point channels
(Ch. 1, 4, 7, 10, 13, 16, 19, 22)
Perform Fast Fourier Transform
Sum power spectrum for band energy:
[Result matrix-Delamination]
Calculate energy loss between sensors
by energy loss calculation process:
[Result matrix-Surface damage]
Apply position information
Encoder data
Apply position information
Display 2-D interpolated color map
Display 2-D interpolated color map
Delamination map
Vertical crack map

Figure 5.9. Flowchart for the mechanical wave-based damage detection of an automated crack evaluation system. The obtained mechanical waves are processed to present the delamination map and vertical crack map.

5.3.2 *GPR-Based Detection for Reinforcement Corrosion*

The corroded reinforcement is detected with GPR. GPR technique uses the EM wave responses from the steel reinforcement. Two wave responses are considered to evaluate the reinforcement corrosion: the peak wave amplitude of the reflected EM wave from the reinforcement and its arrival time. The arrival time is mostly converted to depth by using the two-way travel time (TWTT). The collected EM wave is normalized by a direct coupling wave. The direct coupling is the first pulse on the GPR signal. Since the direct coupling wave influence the entire wave response, the obtained wave amplitude is normalized by the direct coupling wave amplitude (A_{dc}) (Pashoutani and Zhu 2020),

$$A_{norm} = 20 \log\left(\frac{A}{A_{dc}}\right) \quad (5.6)$$

where $A_{norm}$is the normalized amplitude of reinforcement. A in the raw amplitude of reinforcement. From the normalized A-scan data, the normalized peak amplitude of reinforcement reflection and TWTT of the peak point are obtained. The TWTT is converted to depth with the EM wave speed. The obtained normalized amplitude and depth of the reinforcements are presented in the scatter plot. 90th percentile linear regression line is calculated from the scattered data to perform the depth correction. The depth correction is performed to eliminate the depth-dependent amplitude effects by subtracting the regression line from the amplitudes (Barnes et al. 2008). The depth-corrected amplitude presents the reinforcement corrosion and concrete deterioration. The obtained depth-corrected amplitudes will be presented by 2-D interpolation colormap as described in the section of delamination detection. The main procedure for the corroded reinforcement detection is described in Figure 5.10.

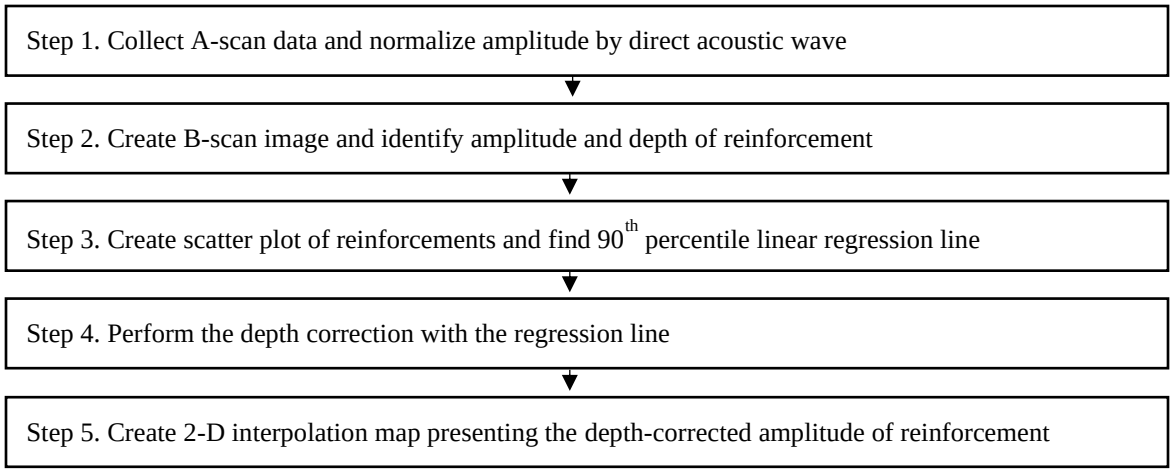

Figure 5.10. Procedure for corroded reinforcement detection. The EM wave data is converted to a 2-D interpolation colormap with a normalization and depth correction process.

5.4 Laboratory Verification of DSBI System-Based Detection System

Before deploying the DSBI system on the ACE platform, laboratory tests are performed to verify the performance of the system with different parameters to detect delamination and vertical crack. For the delamination detection, the bridge deck sample is fabricated, including various sizes and depth of artificial delaminations as described in Figure 5.11. Three different sizes of thin plastic plates, 46 × 46, 30 × 30, and 20 × 20 cm^2, are placed at two different depths, 4 cm and 10 cm.

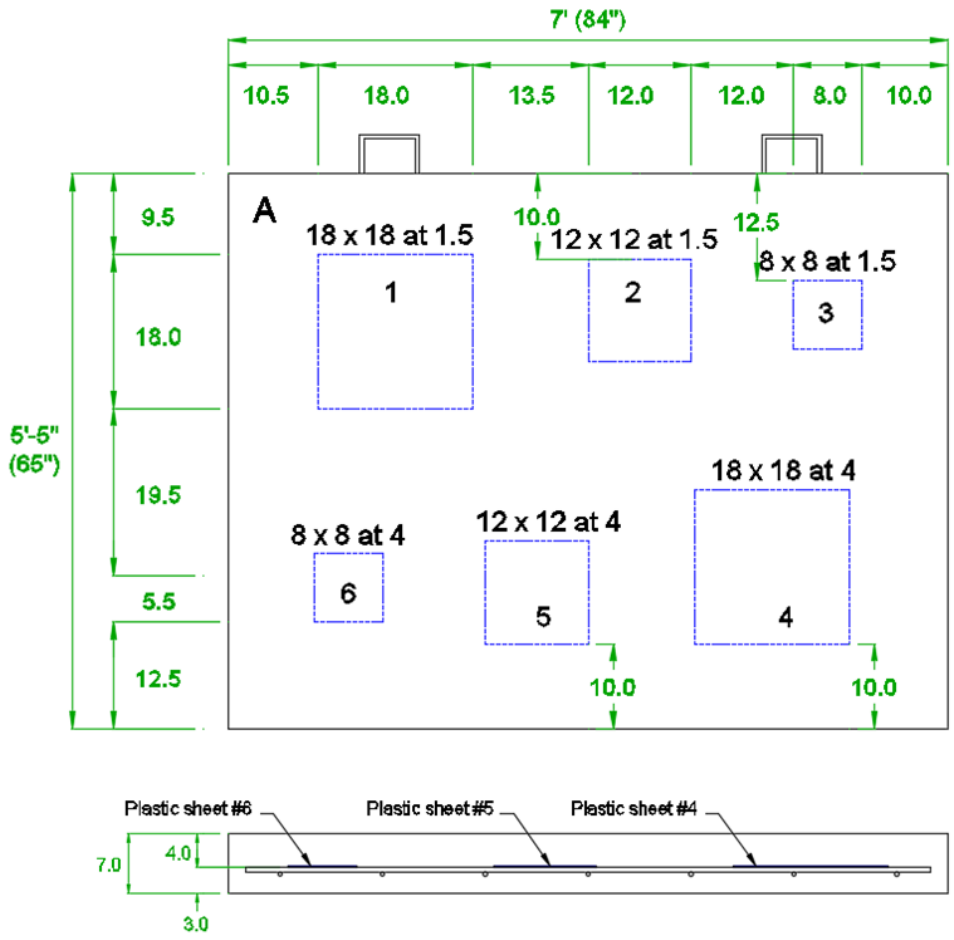
7' (84")
10.5
18.0
13.5
12.0
12.0
8.0
10.0
A
18 x 18 at 1.5
1
10.0
12 x 12 at 1.5
2
12.5
8 x 8 at 1.5
3
9.5
18.0
5'-5"
(65")
19.5
5.5
12.5
8 x 8 at 4
6
12 x 12 at 4
5
18 x 18 at 4
4
10.0
10.0
Plastic sheet #6
Plastic sheet #5
Plastic sheet #4
7.0
4.0
3.0

(a)

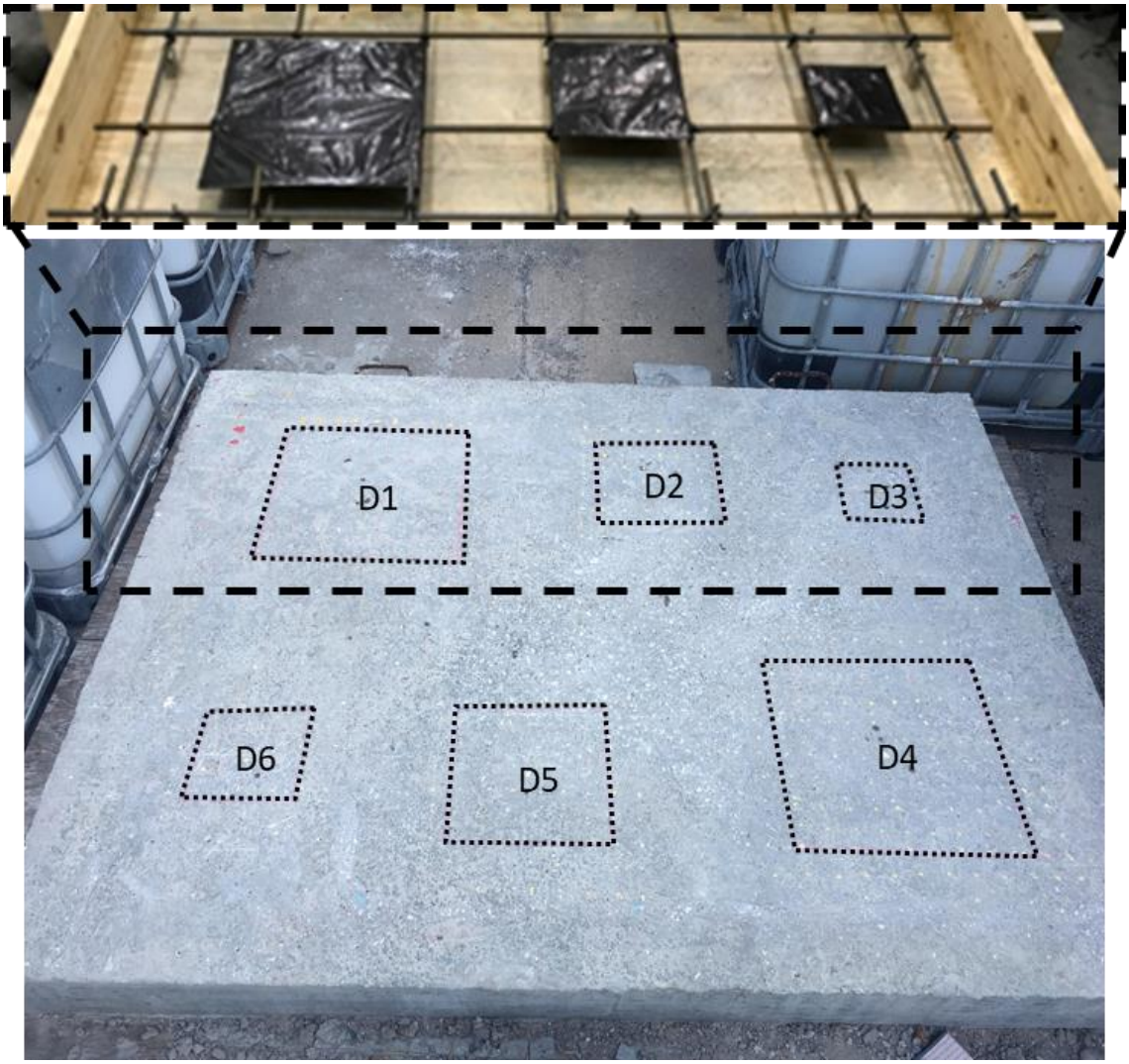

(b)

Figure 5.11. Prepared bridge deck sample for the laboratory delamination detection: (a) detailed design of the sample and (b) prepared bridge deck sample and artificial delamination image before casting. Three different sizes and two different depths are designed to produce the artificial delaminations (1 in. = 25.4 mm).

The impact-echo test is performed with the different parameters that might influence the flexural vibration detection operated by the DSBI system: impacting angle, impacting ball size, impacting condition, delamination size, and delamination depth.

The purpose of the impact angle and height variation test is to find a proper angle and height for the DSBI system to obtain a reliable flexural vibration mode. The height represents the distance between the DSBI

system and the concrete surface. The height is possibly changed in the field due to the gradient and surface damage (e.g., potholes). The impact angle is the angle between the impactor and surface at the impacting moment. Consequently, the various angles occur when the height is changed.

The impact-echo test is conducted on D3 delamination with three different heights, 7.6 cm (3 in.), 12.7 cm (5 in.), and 17.8 cm (7 in.), which have impact angles of 30, 60, and 90 degrees, respectively. The results of the high variation test are presented in the frequency-domain response, as shown in Figure 5.12. All three cases show the proper measurement of the flexural vibration mode around 4 kHz. However, the significant magnitude decrease occurs in the 90 degrees of impact angle test since 90 degrees impact cannot show a proper DSBI by just scratching the surface. Since the magnitude of flexural vibration mode at 30- and 60-degrees are impacting shows similar, the ACE scanning platform is designed to secure the height in lesser than 12.7 cm to deploy the DSBI system.

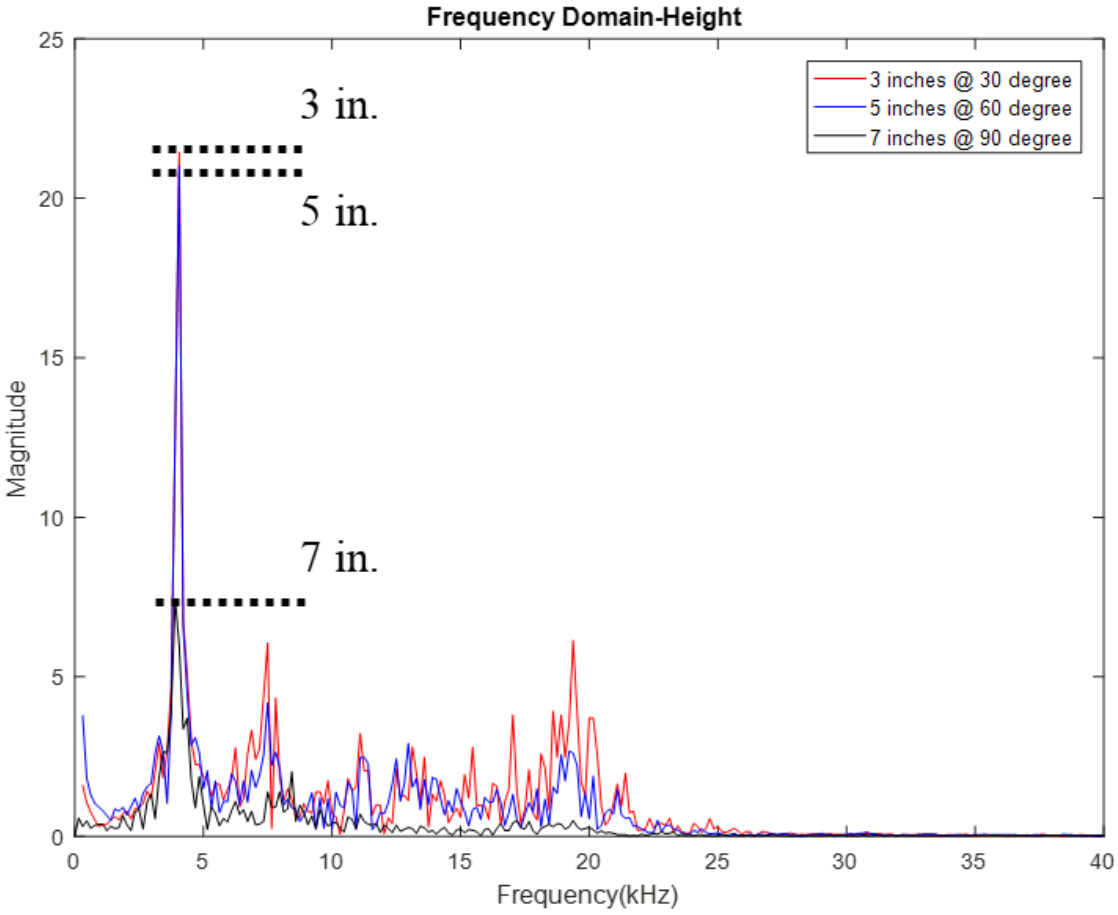
Frequency Domain-Height
3 inches @ 30 degree
5 inches @ 60 degree
7 inches @ 90 degree
3 in.
5 in.
7 in.
Magnitude
Frequency(kHz)
0
5
10
15
20
25
30
35
40

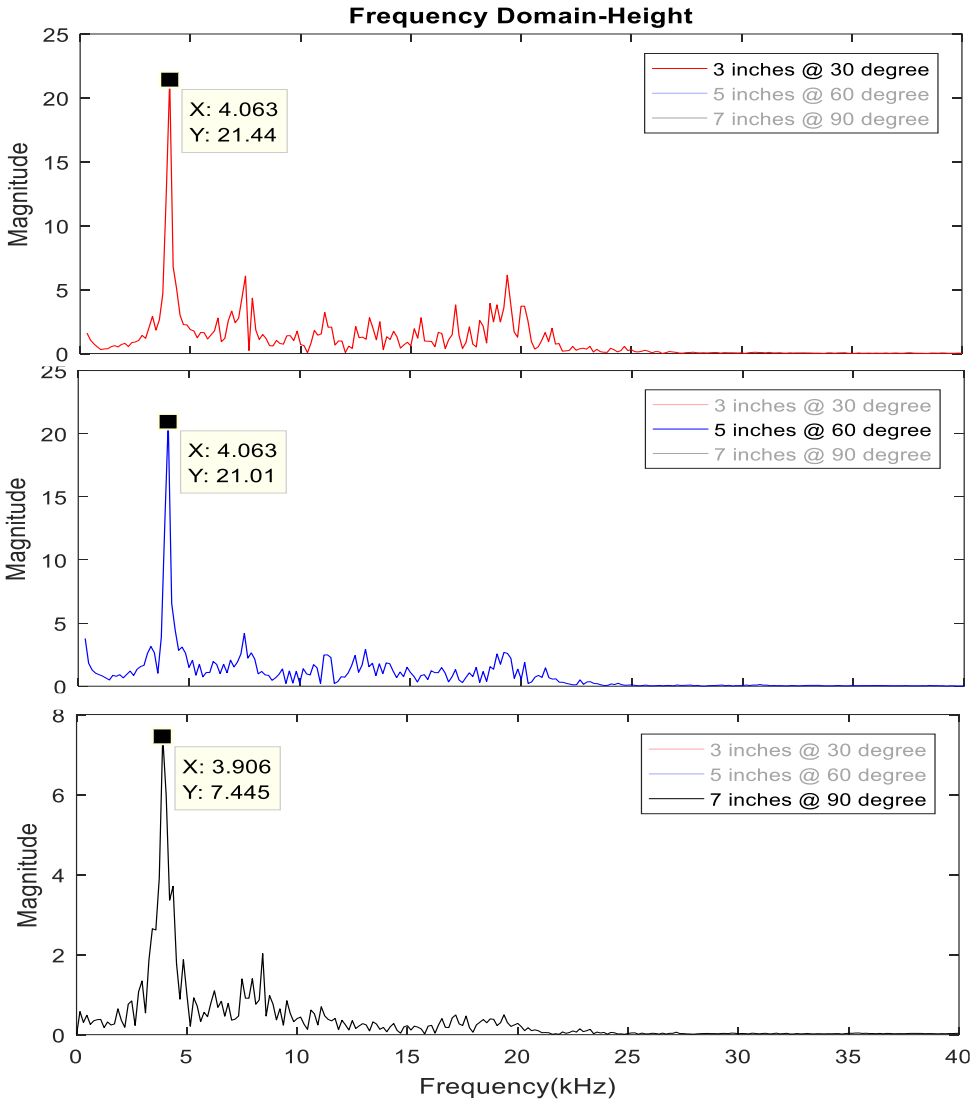

Figure 5.12. Laboratory test results of delamination detection with different impacting angles and height in DSBI system (1 in. = 25.4 mm). All angles can detect delamination. Lesser than 60 degrees of impacting angle shows an appropriate DSBI system and reliable impacting force.

To understand the relation between excitation frequency and damage detection accuracy on the flexural vibration mode, various excitation frequency, 8 to 11 kHz incident waves are generated. Different ball sizes are considered from the relation between ball size and wave frequency (Sansalone and Streett 1997). Thus, various frequencies, 8, 8.5, 9.3, 10, and 11 kHz, are generated by different ball sizes, 14, 12, 10, 8, and 6 mm. The impact-echo tests are conducted on the intact concrete and D3 delamination with five different sizes of ball impactors, 6, 8, 10, 12, and 14 mm. For the intact concrete sample, a large concrete block size

is selected to avoid any thickness mode or flexural mode of vibration. The obtained normalized frequency responses from the intact concrete impact-echo test are shown in Figure 5.13 (a). The results of an impact-echo test conducted on D3 delamination are shown in Figure 5.13 (b). Based on the intact concrete test, the ball size and incident wave frequency relation is verified. Since the induced range of incident wave frequency is not in the flexural vibration mode range, mostly below 6 kHz, all ball sizes are applicable for delamination detection. The delamination detection result indicates that all selected balls can detect flexural vibrations. The bigger ball size shows a higher magnitude of the flexural vibration mode. Based on the results of two impact-echo tests with different impact ball sizes, the ACES choose the 12 mm ball size to have the proper impacting force and distinguishable frequency range from the flexural vibration on the delamination.

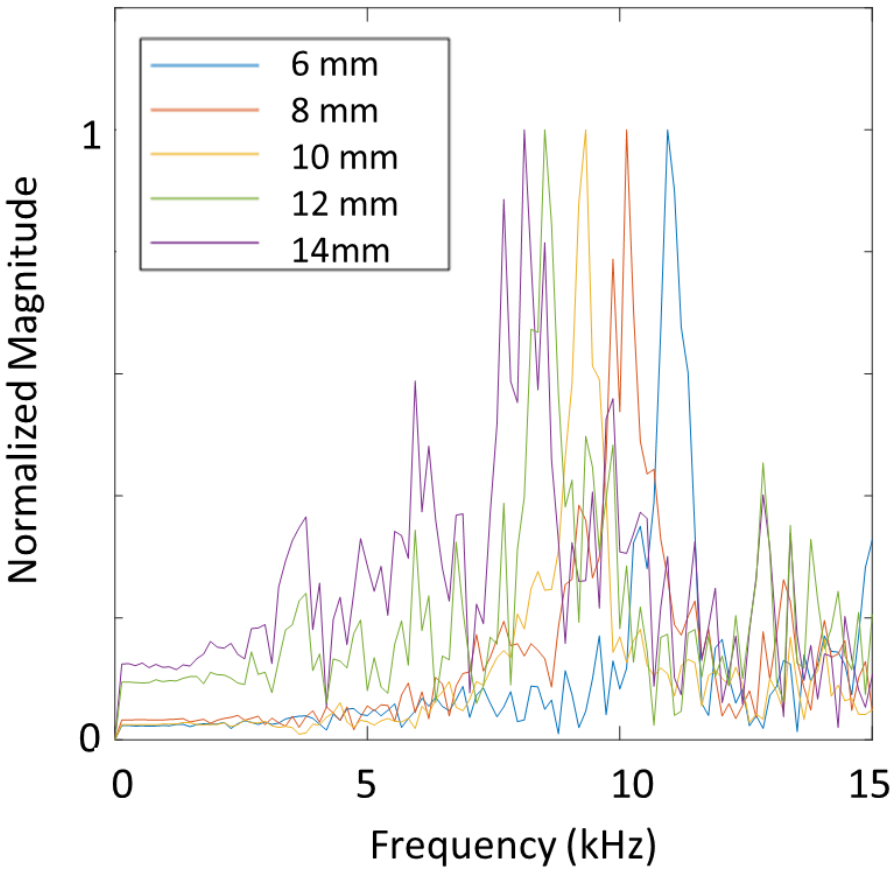
6 mm
8 mm
10 mm
12 mm
14mm
Normalized Magnitude
1
0
0
5
10
15
Frequency (kHz)

(a)

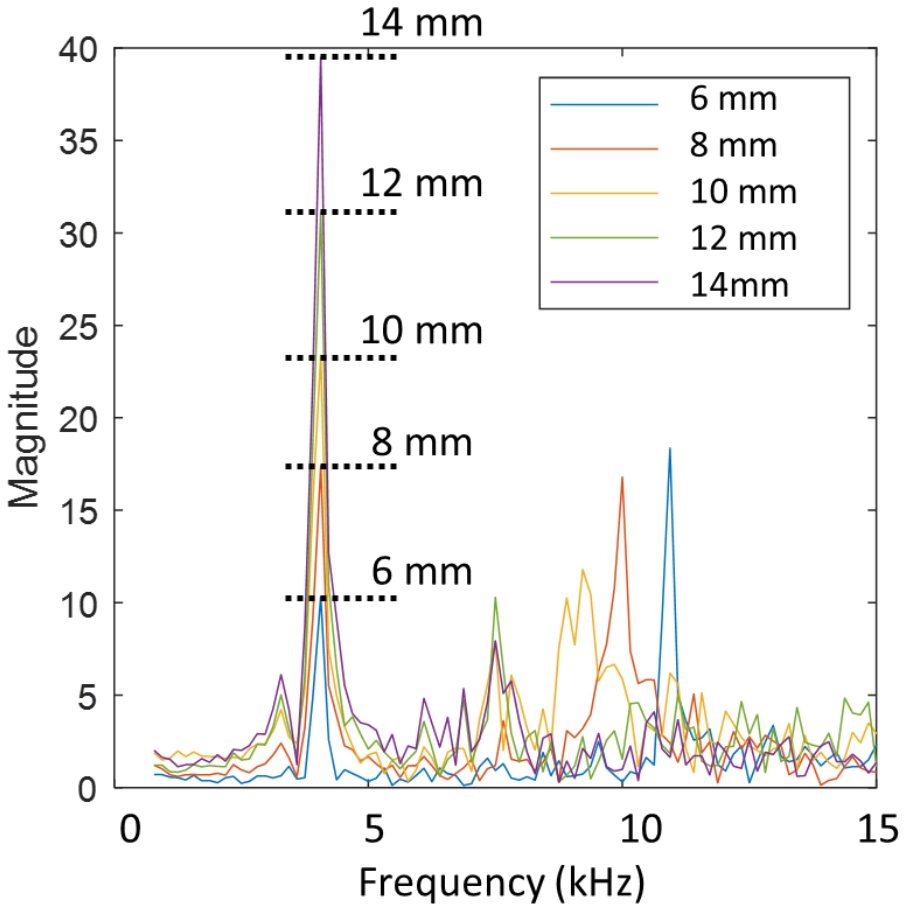

(b)

Figure 5.13. A laboratory test result of delamination detection with different ball sizes, 6, 8, 10, 12, and 14 mm: (a) frequency response from the deep concrete impact-echo test and (b) frequency response of the flexural vibration mode from the impact-echo test on the D3 delamination. A bigger size impact ball shows a higher magnitude of flexural vibration mode. All the impact-echo test results provide the detected flexural vibration mode at 4 kHz on D3 delamination.

As the laboratory test of the impact condition, the impact-echo test in double impacts condition is conducted because this could happen due to field environment conditions, such as surface conditions. The purpose of this Laboratory test is to understand the influence of the double-impact condition on delamination detection. The double-impact is generated by impacting two balls at the same location to have a short-time distance for two impacts. The effect of the double impacts in one impact intended is investigated, as shown in Figure 5.14. The frequency responses from the double-impact test in Figure 5.14 (b) and the single-impact test in

Figure 5.14 (d) show a similar magnitude of the flexural vibration mode on D3 delamination. It implies that the DSBI system can detect delamination even in the double-impacting condition.

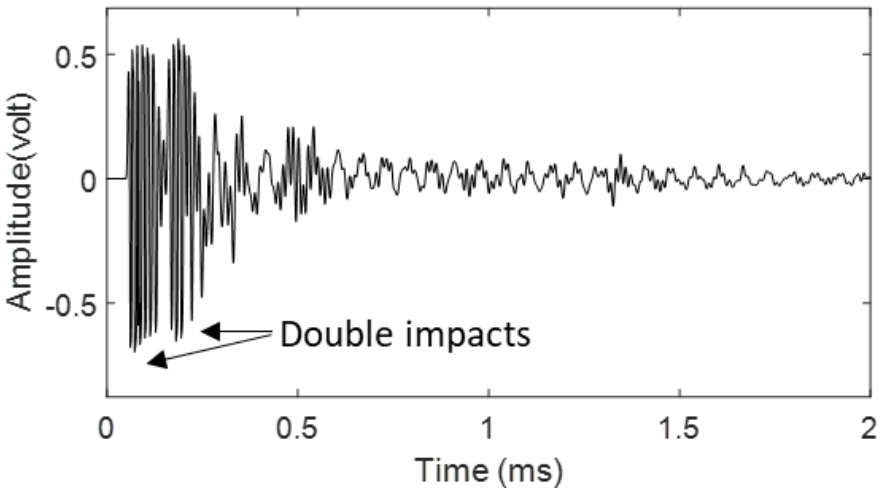
0.5
0
-0.5
Amplitude(volt)
Double impacts
0
0.5
1
1.5
2
Time (ms)

(a)

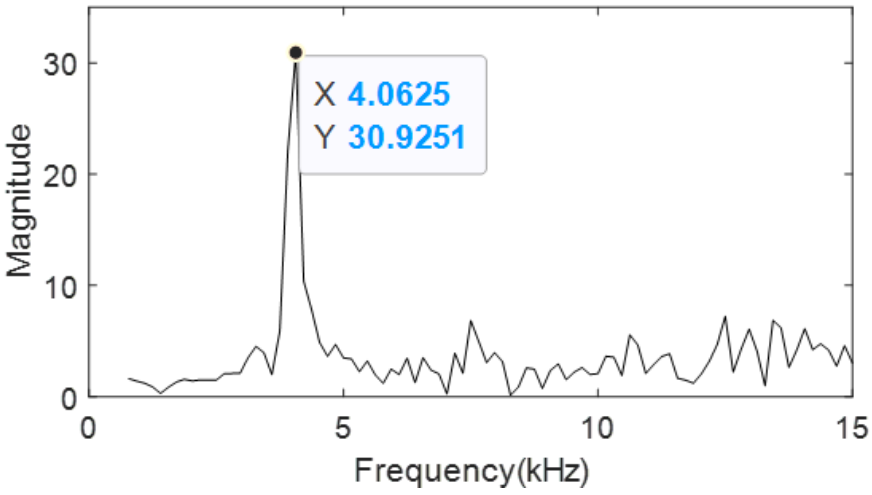
30
20
10
0
Magnitude
X 4.0625
Y 30.9251
0
5
10
15
Frequency(kHz)

(b)

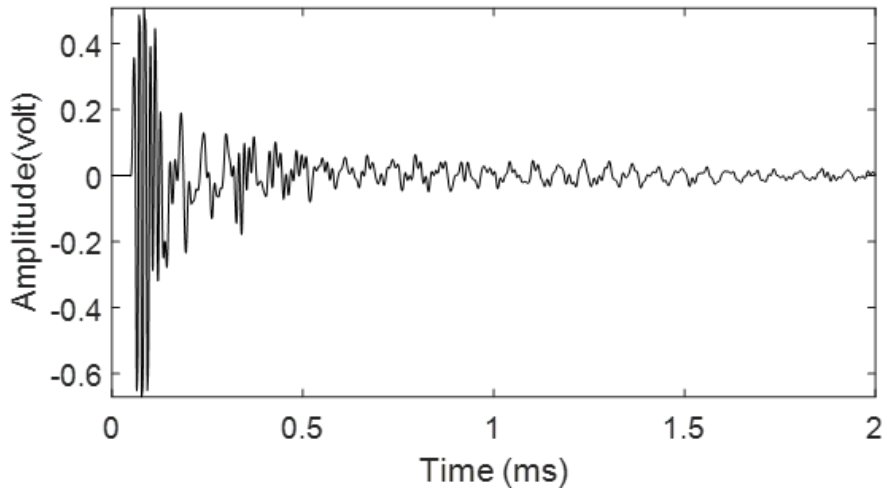

(c)

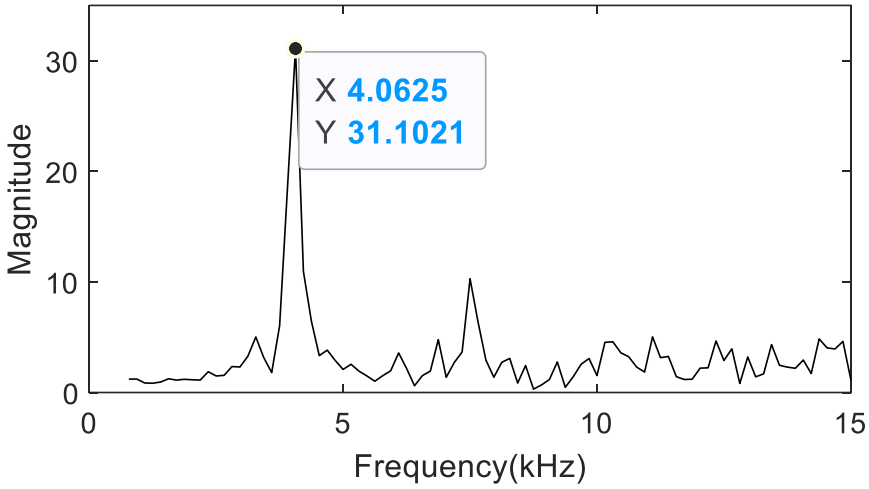

(d)

Figure 5.14. Laboratory test result of delamination detection in double-impact condition: (a) wave signal of the double-impact test, (b) frequency-domain signal of double-impact test, (c) wave signal of the single-impact test, and (d) frequency-domain signal of the single-impact test. Double impacts also show a proper flexural vibration mode at 4 kHz with a similar magnitude to the single-impact test. It implies the DSBI system can detect delamination even in the double-impacting condition.

To verify the DSBI system in different delamination geometry, the impact-echo tests are performed with different sizes and depths. The size and depth of delaminations are described in the bridge deck sample

design (see Figure 5.2). The test results with the prepared artificial delaminations are shown in Figure 5.15. Based on the results, the DSBI system can detect delamination of different sizes and different depths.

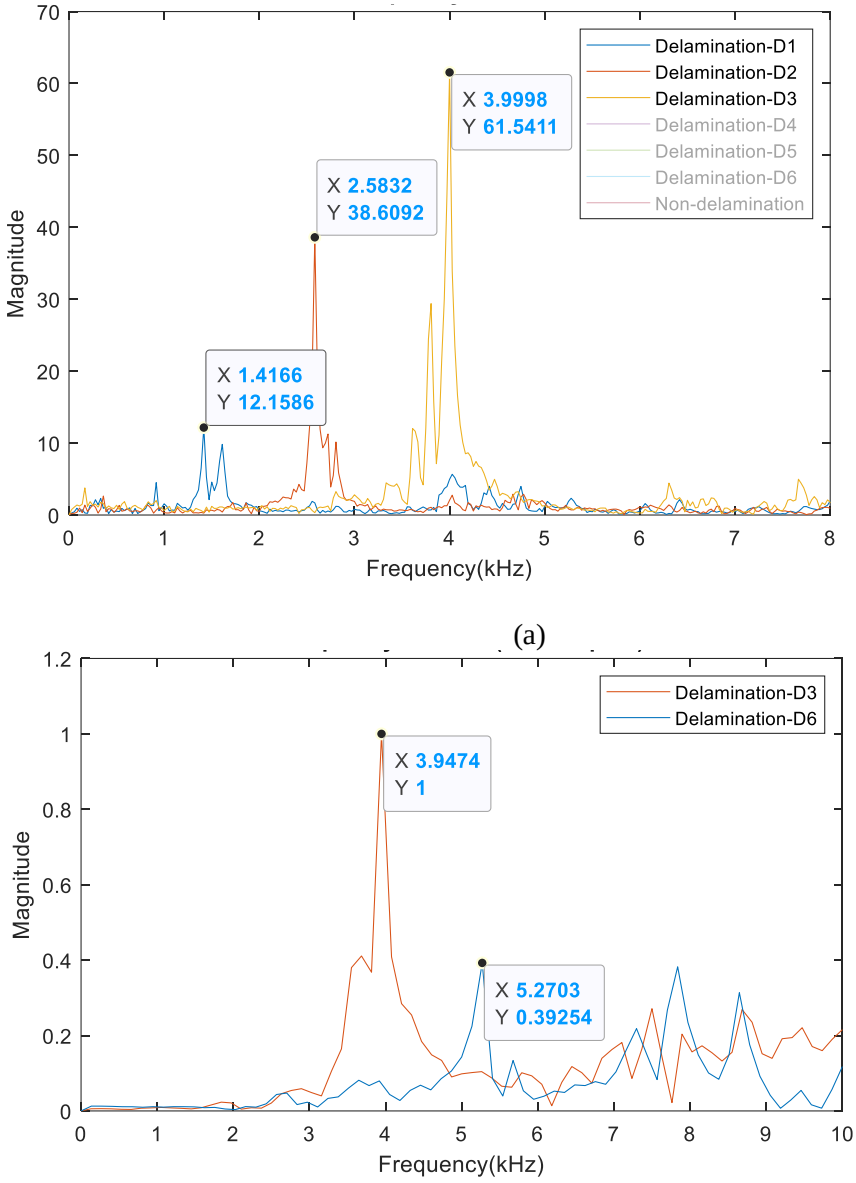

Figure 5.15. A laboratory test result of delamination detection in different delamination geometries: (a) flexural vibration mode in different delamination sizes and (b) flexural vibration mode in different delamination depths. The DSBI system can detect the artificial delaminations of the bridge deck sample in different sizes and depths.

DSBI system is modified and verified through laboratory tests. The results of the laboratory test present: lower than 12.7 height and 12 mm impact ball size are appropriate for the DSBI system; DSBI system can provide a reliable measurement of the flexural vibration mode even in double impact condition and different size and depth of delamination. The final impact-echo test to detect delamination in the entire area of the bridge deck sample is performed with the modified DSBI system. The test is conducted with a 5 cm × 5 cm resolution of the data measurement. Two post-processings are conducted to create two colormaps: 2-D interpolation colormap and 2-D transparent interpolation colormap. The 2-D interpolation colormap is obtained by interpolating for the 2-D matrix in a spatial meshed grid, as shown in Figure 5.16 (a). The 2-D matrix for the colormap is the EI matrix calculated by Eq. (5.3). The 2-D transparent interpolation colormap is created to present the magnitude in a certain frequency range without calculating the EI. The transparency value, referred to as alpha value, is between 0 (fully transparent) and 1 (fully opaque). The obtained 2-D transparent interpolation colormap with 0.1 alpha value is shown in Figure 5.16 (b). The additional ultrasonic tomography scanning is conducted to verify the impact-echo test result using the DSBI system, as shown in Figure 5.16 (c). The three detection results show a significant agreement with the actual configuration of the artificial delaminations. The 2-D interpolation map with the EI matrix clearly presents the delamination than the transparent colormap presenting the magnitude of frequency components.

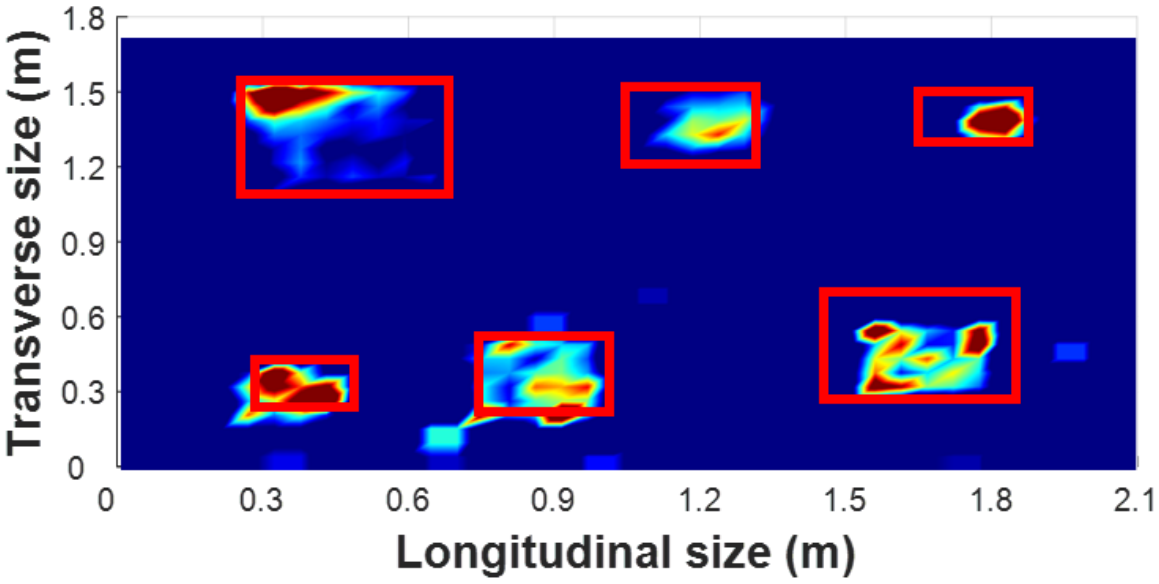
Transverse size (m)
1.8
1.5
1.2
0.9
0.6
0.3
0
0
0.3
0.6
0.9
1.2
1.5
1.8
2.1
Longitudinal size (m)

(a)

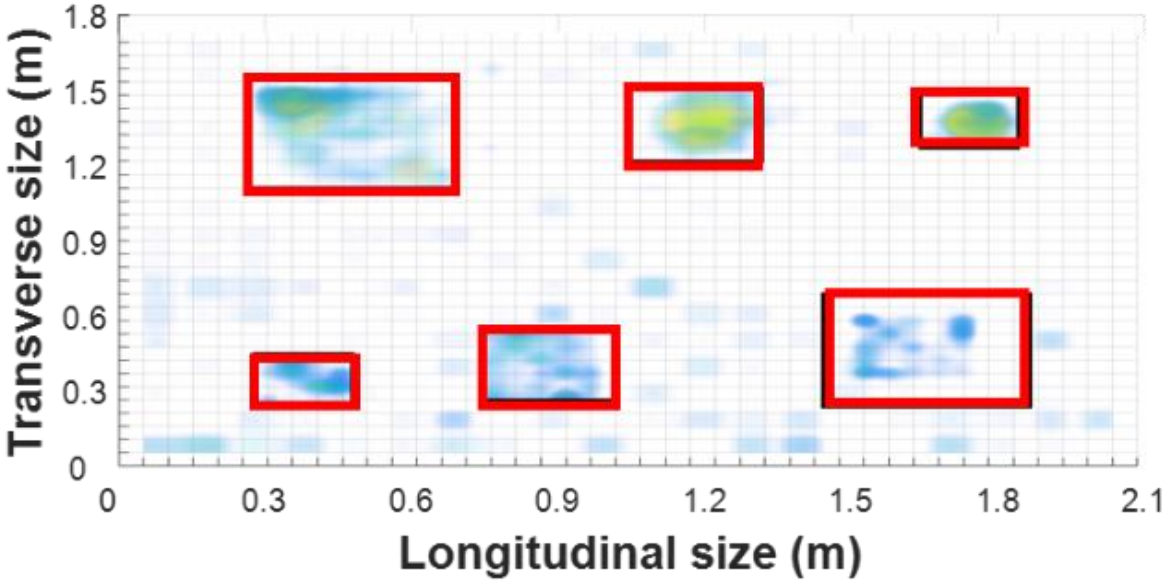
Transverse size (m)
1.8
1.5
1.2
0.9
0.6
0.3
0
0
0.3
0.6
0.9
1.2
1.5
1.8
2.1
Longitudinal size (m)

(b)

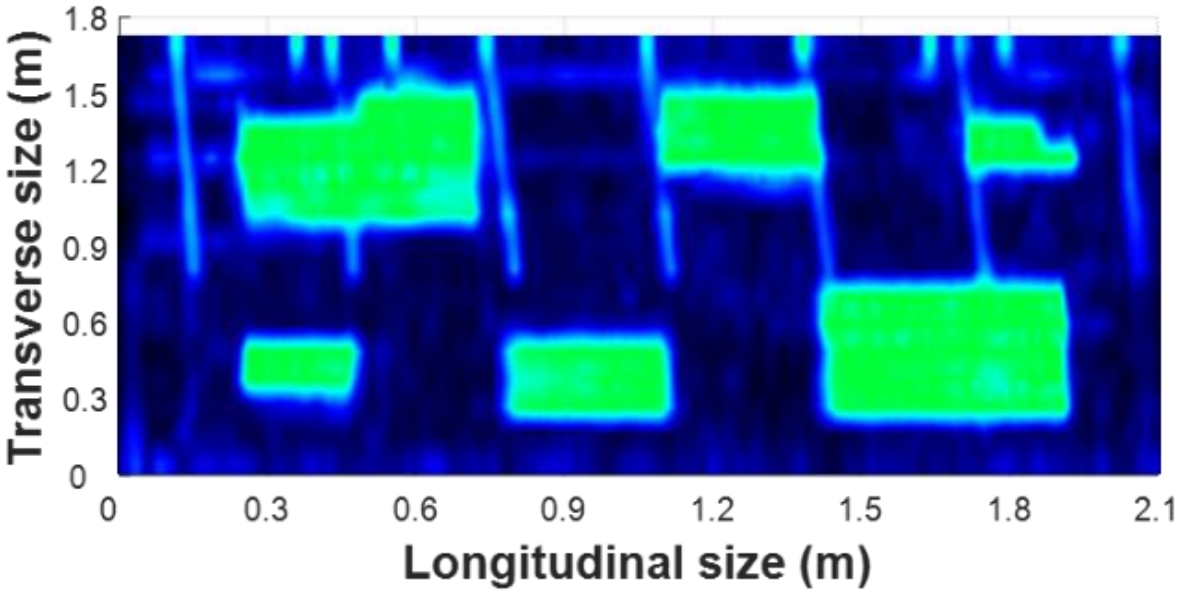

(c)

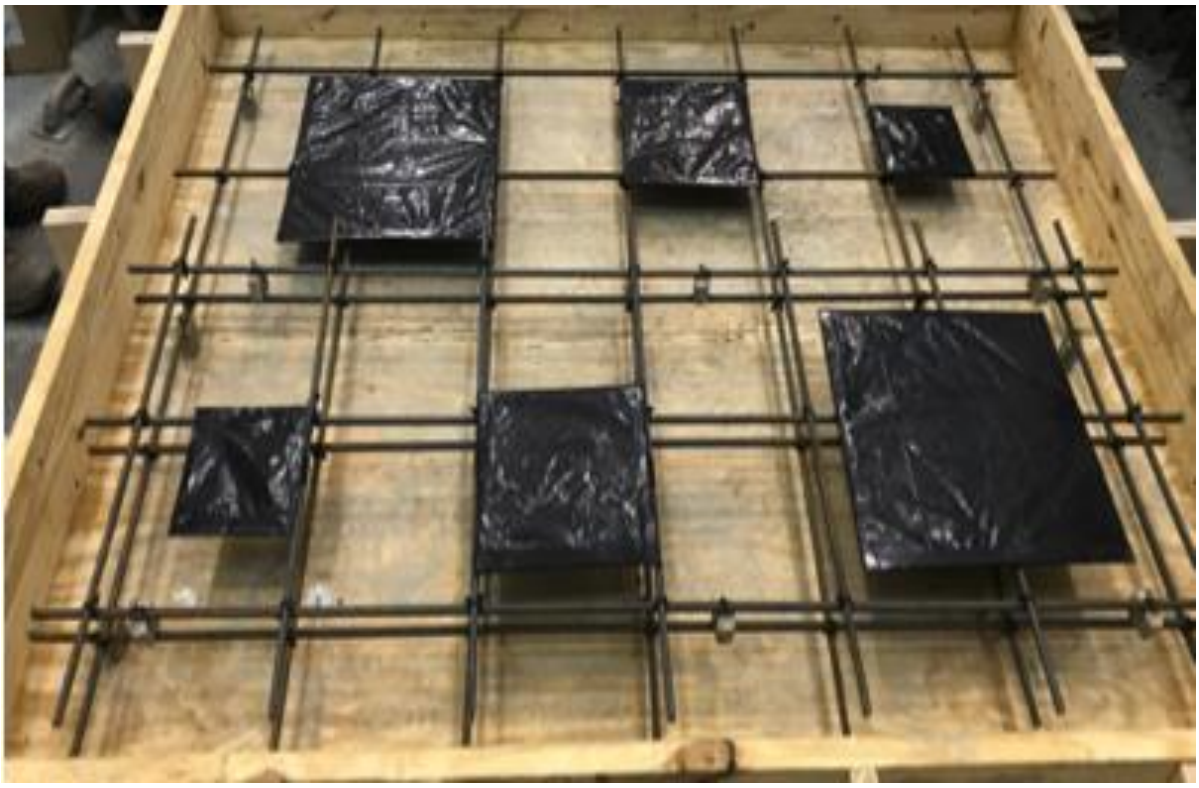

(d)

Figure 5.16. Delamination detection result using DSBI system and ultrasonic tomography: (a) 2-D interpolation map from the impact-echo testing with DSBI system, (b) 2-D transparent interpolation colormap from the impact-echo testing with DSBI system (c) sample scanning image by ultrasonic tomograph device, and (d) artificial delaminations in the bridge deck sample. All the placed artificial

delaminations are detected by the DSBI system and verified by the ultrasonic tomography device and sample design. 2-D interpolation colormap (b) shows a clear delamination image than cloud plot (a). The ultrasonic tomography shows the artificial delamination (green) by obtaining a strong reflection on the delamination.

A laboratory test was conducted to detect vertical cracks using the DSBI system and multiple MEMS sensors. The purpose of this test was to verify the surface wave attenuation method for detecting vertical cracks. Based on the wavelength of the incident wave (see the frequency in Figure 5.13 (a)), the effective depth is 10 cm. Thus, the internal subsurface crack, which has the top crack tip in 10 cm depth, is detectable. Three tests are conducted with intact concrete pavement and cracked concrete pavement, including 1 mm and 3 mm wide of crack. The four MEMS sensors are located on the crack as described in Figure 5.17 (a). The wave energy, *E*, is obtained from each sensor's wave response, which is represented by the shaded areas in Figure 5.17 (b) and (c). The surface wave attenuation on the intact concrete pavement follows the typical wave attenuation tendency (red dashed line, R^2=0.9445 in exponential regression curve). However, the 3mm cracked test shows a significant energy decrease between MEMS 2 and MEMS 3 signals. The obtained wave energy is presented in Figure 5.17 (d). The obtained energy loss, *EL*, from the laboratory test is presented in Figure 5.17 (e). The tests performed with the 1 mm and 3 mm wide crack show significant energy losses as 71.6 % and 91.2 % (red dashed circle), respectively.

On the other hand, the intact concrete pavement shows 50.8 %. In the case of $EL_{3\text{-}4}$ of 3 mm cracked concrete, another high energy loss is detected. This indicates that the attenuated wave energy by 3 mm crack is insufficient to perform the additional vertical crack detection. Thus, we consider the two-directional wave propagations in the ASCE system using the additional surface wave propagation (e.g., MEMS 4 to MEMS 1 surface wave by MEMS 4 impact). Figure 5.17 (e) describes the case of two cracks are in different sections. All cases are detected by using two directional wave propagation. Based on the laboratory test results, the vertical cracks can be detected by DSBI and MEMS.

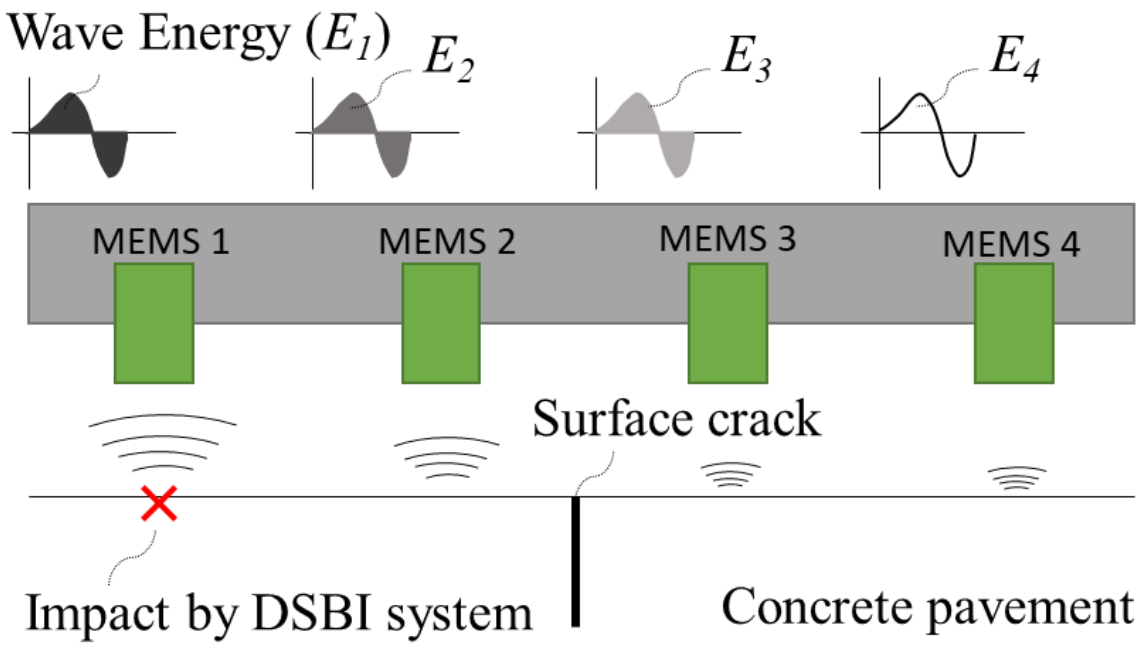
Wave Energy (E_1)
E_2
E_3
E_4
MEMS 1
MEMS 2
MEMS 3
MEMS 4
Surface crack
Impact by DSBI system
Concrete pavement

(a)

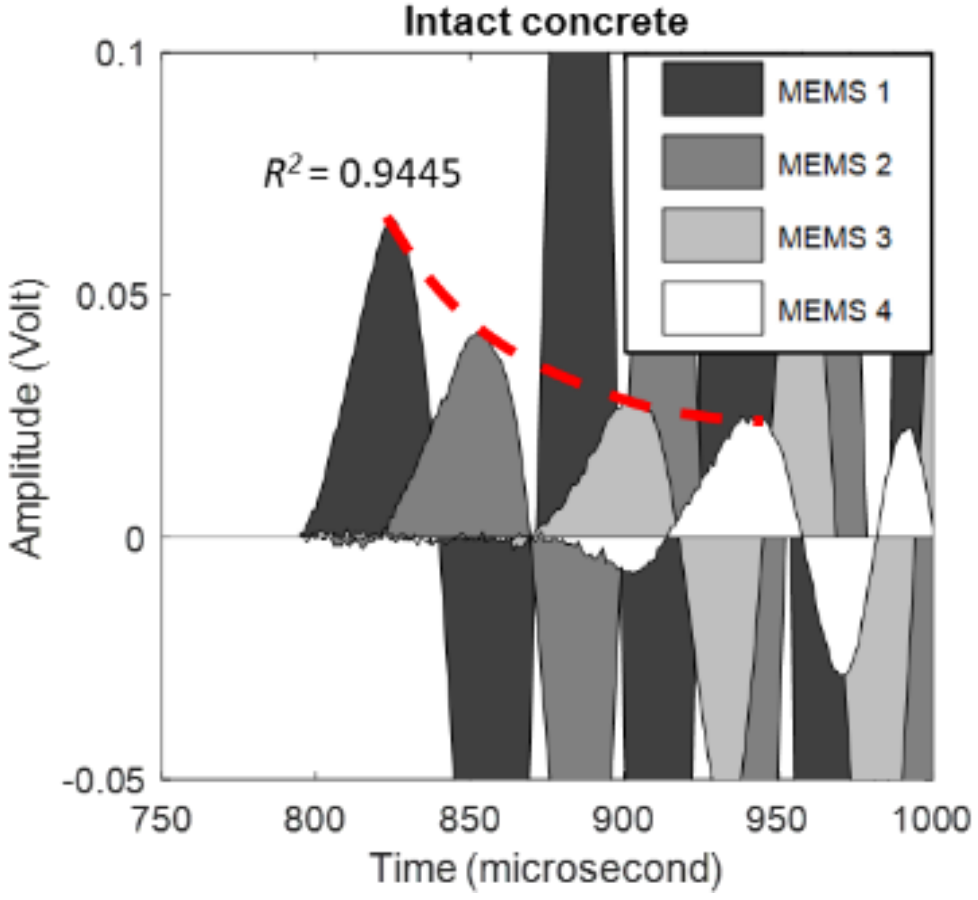
Intact concrete
R^2 = 0.9445
MEMS 1
MEMS 2
MEMS 3
MEMS 4
Amplitude (Volt)
0.1
0.05
0
-0.05
750
800
850
900
950
1000
Time (microsecond)

(b)

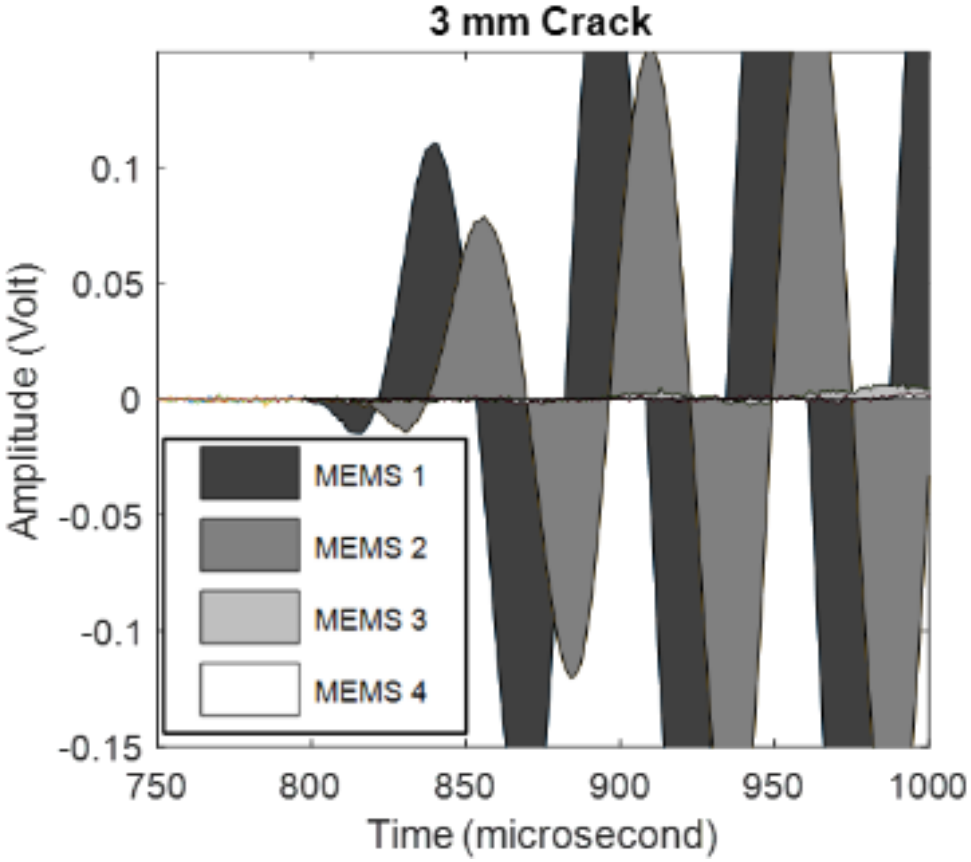
3 mm Crack
Amplitude (Volt)
0.1
0.05
0
-0.05
-0.1
-0.15
750
800
850
900
950
1000
Time (microsecond)
MEMS 1
MEMS 2
MEMS 3
MEMS 4

(c)

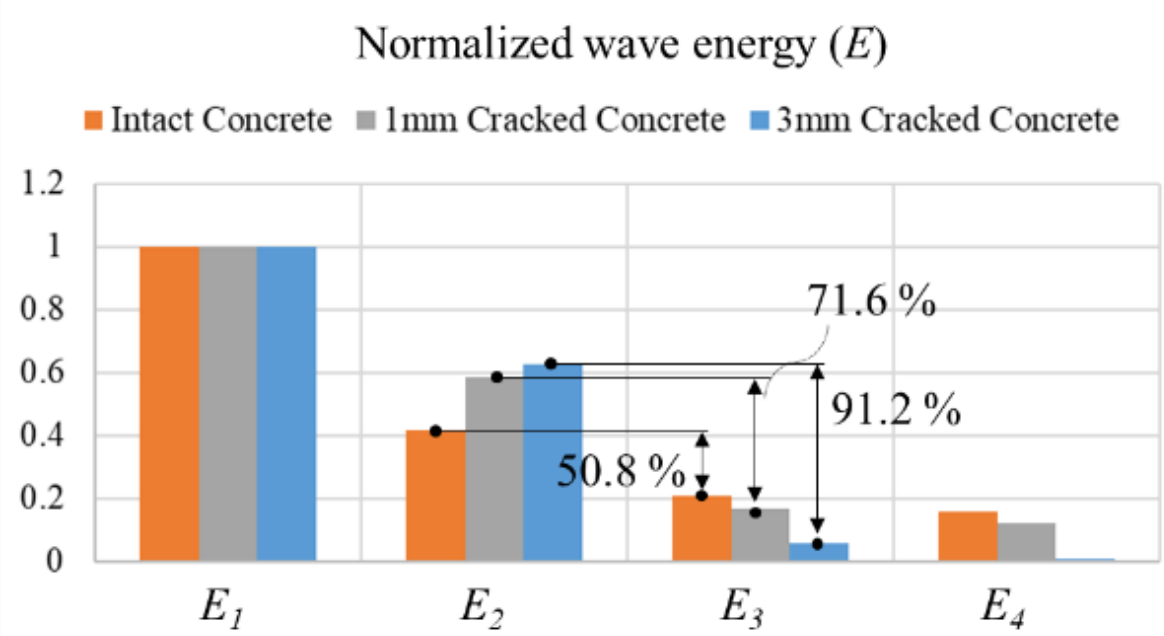
Normalized wave energy (E)
Intact Concrete
1mm Cracked Concrete
3mm Cracked Concrete
1.2
1
0.8
0.6
0.4
0.2
0
71.6 %
91.2 %
50.8 %
E1
E2
E3
E4

(d)

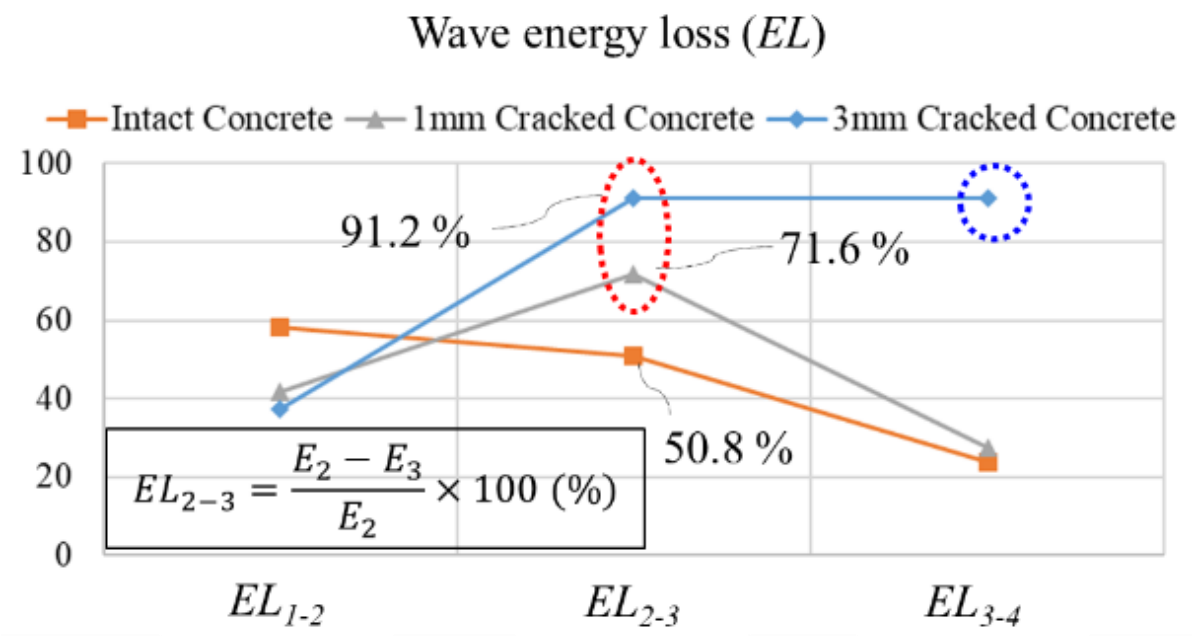
Wave energy loss (EL)
Intact Concrete
1mm Cracked Concrete
3mm Cracked Concrete
100
80
60
40
20
0
91.2 %
71.6 %
50.8 %
$EL_{2-3} = \frac{E_2 - E_3}{E_2} \times 100\ (\%)$
EL_{1-2}
EL_{2-3}
EL_{3-4}

(e)

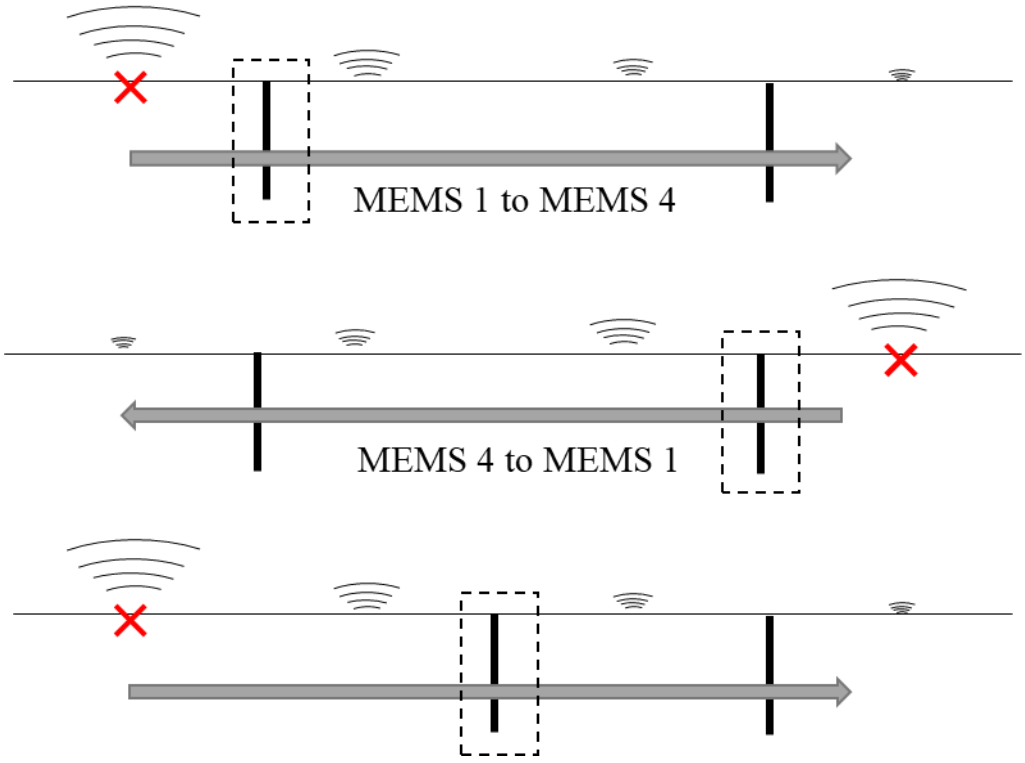
MEMS 1 to MEMS 4
MEMS 4 to MEMS 1

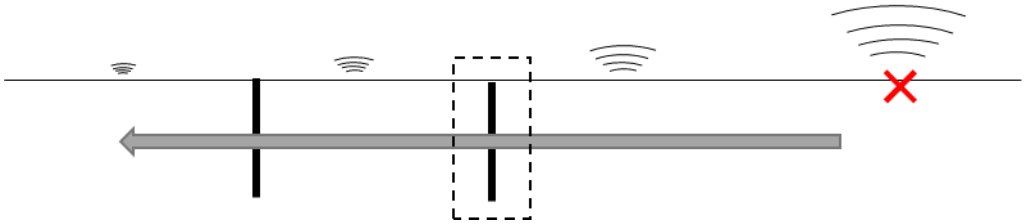

(f)

Figure 5.17. Laboratory tests of vertical crack detection with different crack sizes: (a) conceptual figure of the test setup, (b) obtained signal from an intact concrete test, (c) obtained signal from 3 mm cracked concrete test (d) 0.3-millisecond time-windowed energy (E), (e) energy loss with 0.3-millisecond time-windowed energy (EL), and (f) crack detection in different cases. The cracked concrete show higher energy loss in the cracked section (red dashed circle) and unexpected energy loss in EL_{3-4}.

5.5 Field Demonstration of Automated Crack Evaluation System

5.5.1 *Inspection of Bridge A*

A 95 m long and 13.5 wide concrete bridge in Texas, United States, was selected for field inspection using the new high-speed ACE system. The inspection was performed in May, 2020. This bridge was constructed in 1972 and has two lanes that carry two-way traffic. The ACE system scanned 95 m long and 8 m wide (each scanning path has 2 m wide). Four scans (P1 – P4 in Figure 5.18 (a)) were conducted with 16 km/h speed. The virtual inspection was performed after bridge scanning with the recorded video. 33 spellings, 23 patch-repaired areas, and two longitudinal cracks were identified in the visual inspection. Figure 5.18 (b) shows several surface defects from the recorded video image. The 3-D ultrasonic tomography scanning was performed in 10 different locations.

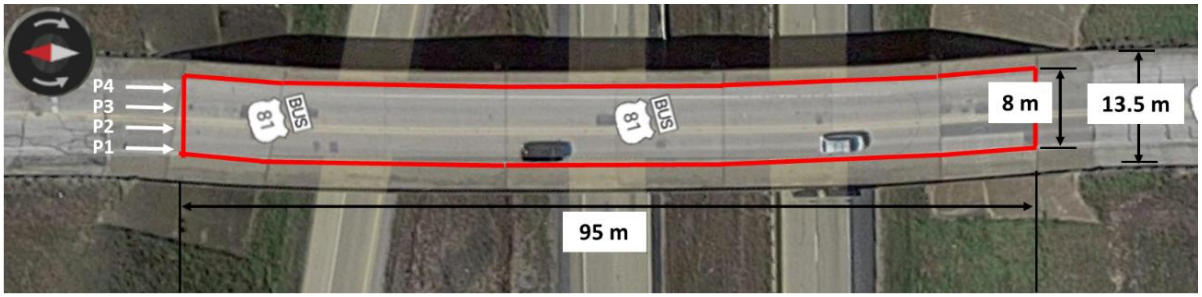

(a)

(b)

Figure 5.18. Scanned bride and surface defects. The ACES system scans 95 m long and 8 m wide area with four paths scanning (P1, P2, P3, and P4). The bridge deck has many surface damages (e.g., spalling).

The inspection results provide information on the severity of delamination, vertical crack, reinforcement corrosion by presenting 2-D interpolation maps. The result maps are described in Figure 5.19. For path scanned data is combined to one colormap by using the positioning system (see Figure 5.5). The severity of damages is presented in jet colormap: red area indicates severe damage: blue area indicates intact area. The delamination colormap presents the energy intensity (EI) of the flexural vibration mode by summing the energy of spectral magnitude between 1 to 6 kHz, as shown in Figure 5.19 (a). The surface image of high energy intensity area is shown in Figure 5.19 (a), red circle. The approximate 1.2 m × 2 m delamination is detected in the area. The recoded surface image shows no surface damage at the delamination location. It indicates that the internal delamination is presented on the energy intensity colormap of delamination detection. The reinforcement corrosion map presents the depth-corrected normalized amplitude (NA) data by the post-processing procedure in Figure 5.10. The corrosion map is displayed with depth-corrected normalized amplitude (*NA*). Some delamination areas are in the same location as the corroded reinforcement (e.g., Area 1 - 3). These areas can be developed to the critical damage (e.g., potholes) due to the negative interaction as mentioned above. The vertical crack map displays the higher energy loss (EL) in the red area. A comparative study is performed between the crack map and visual inspection results. Based on the study, the vertical crack map shows surface-opening cracks in a high energy loss area. The high energy loss area without a surface-opening crack can present the internal crack.

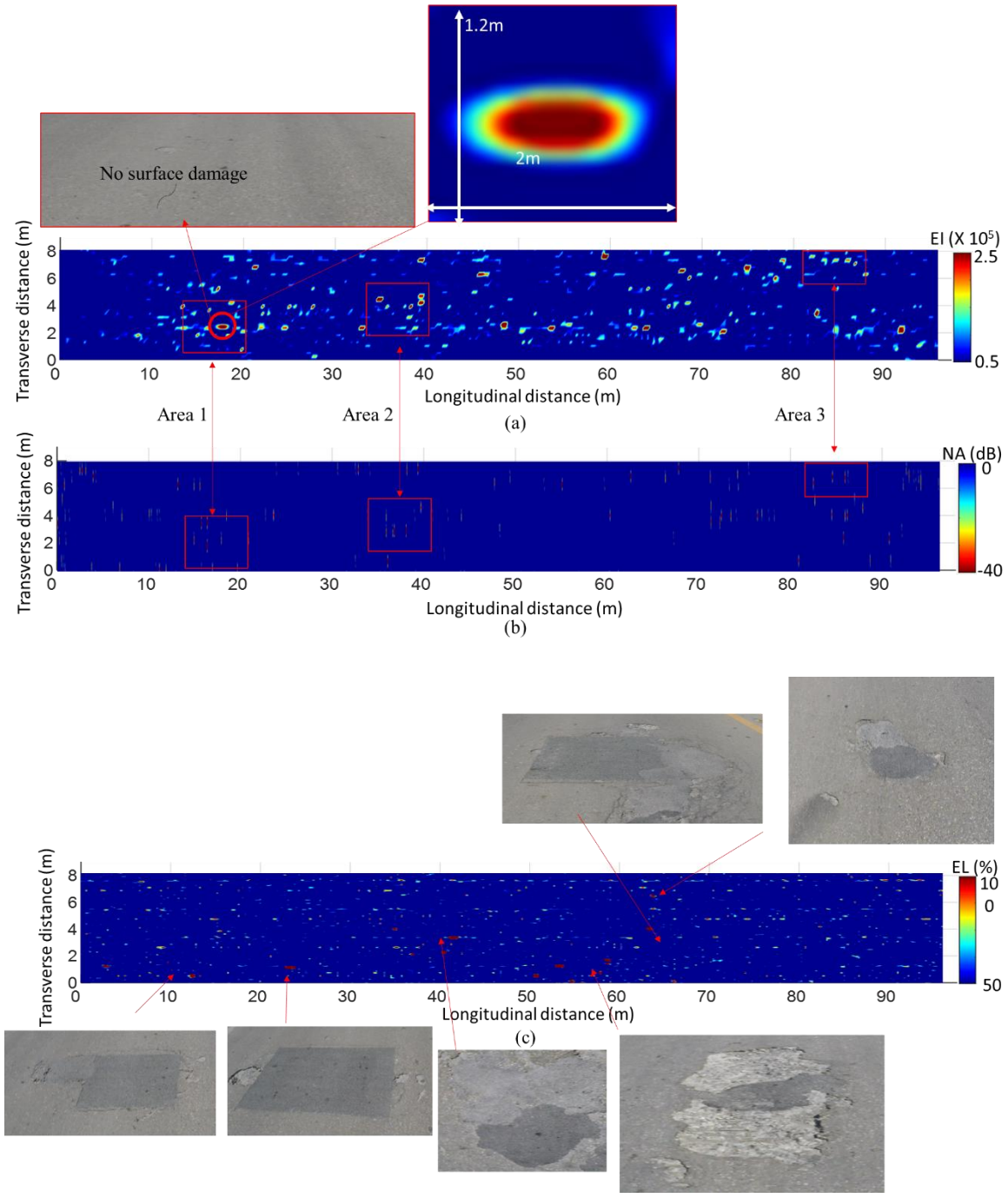

Figure 5.19. Inspection result of the first bridge: (a) delamination map, (b) corrosion map, and (c) vertical crack map. 2-D interpolated colormap representing the detected crack by the automated crack evaluation system

The red circle in Figure 5.19 (a) indicates one delamination area. The 3-D ultrasonic tomograph device measures the location to verify the delamination map obtained from the ACE system, as shown in Figure

5.20. The scanned tomography image shows delamination and bridge deck thickness as the strong wave reflection (red). In addition, near the delaminated area shows scattered waves (green and yellow). It indicates that the void or degraded concrete is near the delamination.

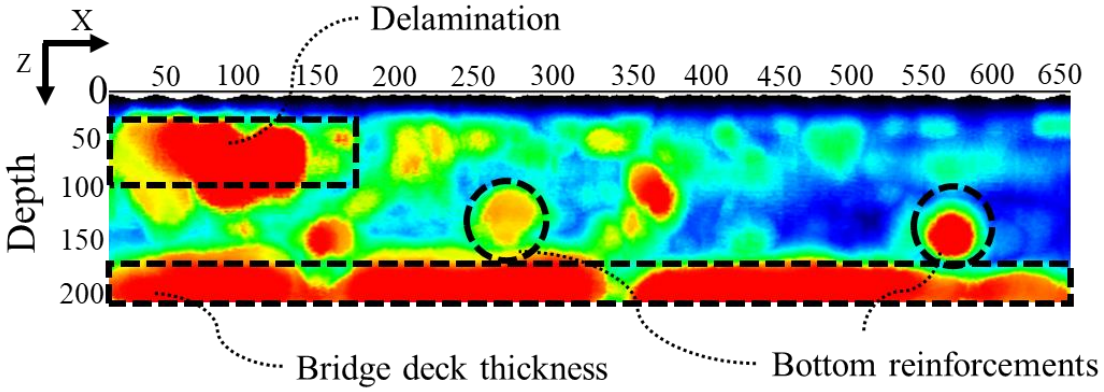

(a)

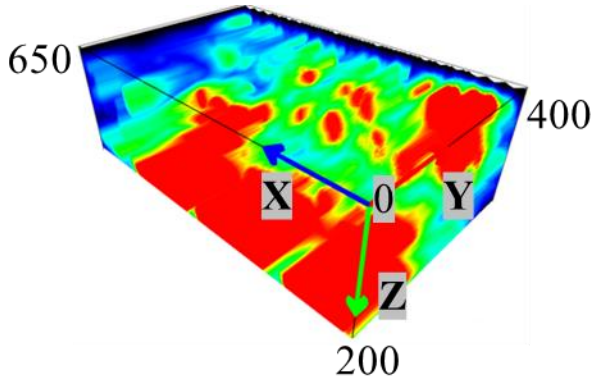

(b)

Figure 5.20. Ultrasonic tomography scanning result of the red circle in *Error! Reference source not found.* ***(a) delamination map: (a) concrete pavement B-scan image (cross-section view) and (b) 3-D tomography image. The delamination area obtained by the delamination map of ACES is verified by the ultrasonic tomography device.***

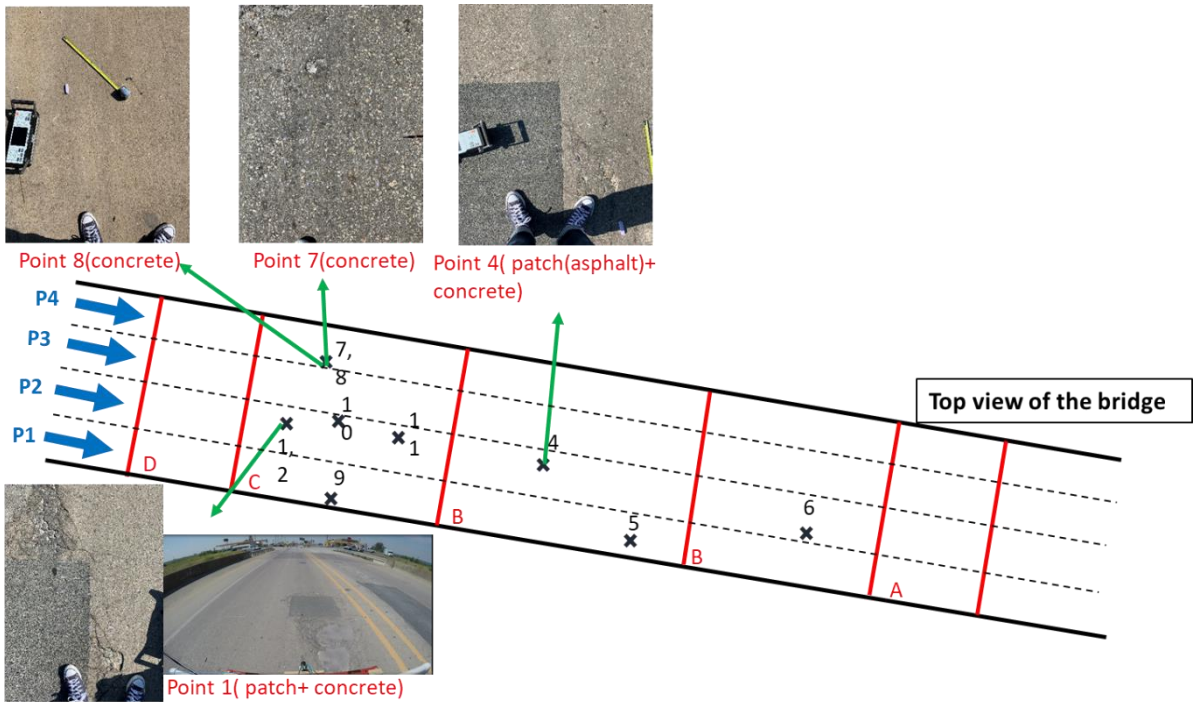
Point 8(concrete)
Point 7(concrete)
Point 4(patch(asphalt)+ concrete)
P4
P3
P2
P1
D
C
B
B
A
Top view of the bridge
Point 1(patch+ concrete)

(a)

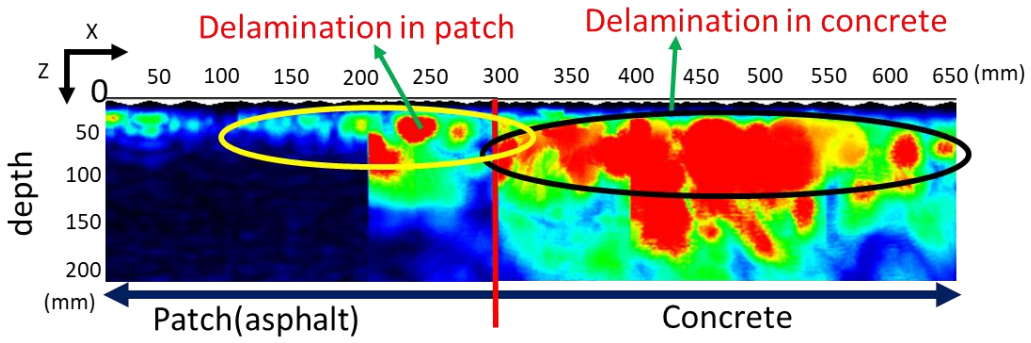
Delamination in patch
Delamination in concrete
X
Z
0
50 100 150 200 250 300 350 400 450 500 550 600 650 (mm)
depth
50
100
150
200
(mm)
Patch(asphalt)
Concrete

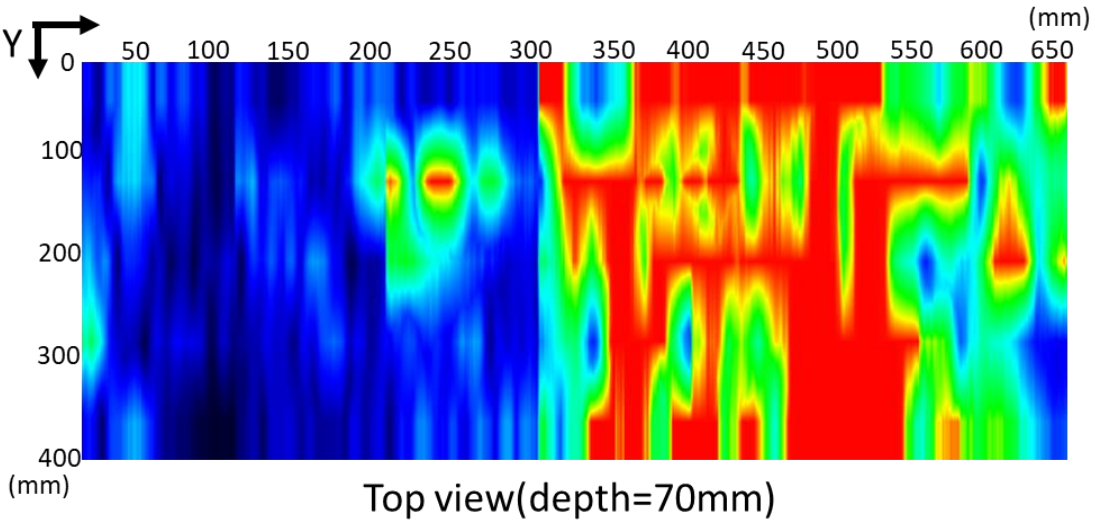
Y
0
50
100
150
200
250
300
350
400
450
500
550
600
650
(mm)
100
200
300
400
(mm)
Top view(depth=70mm)

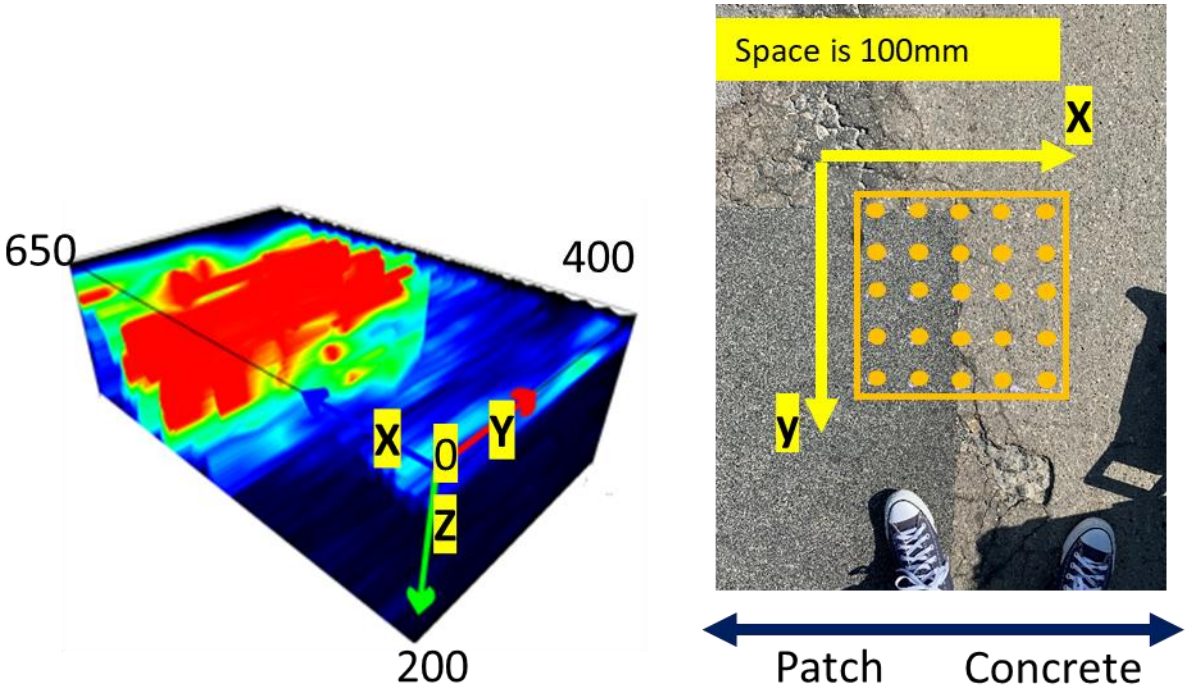
650
400
X
0
Y
Z
200
Space is 100mm
X
y
Patch
Concrete

(b)

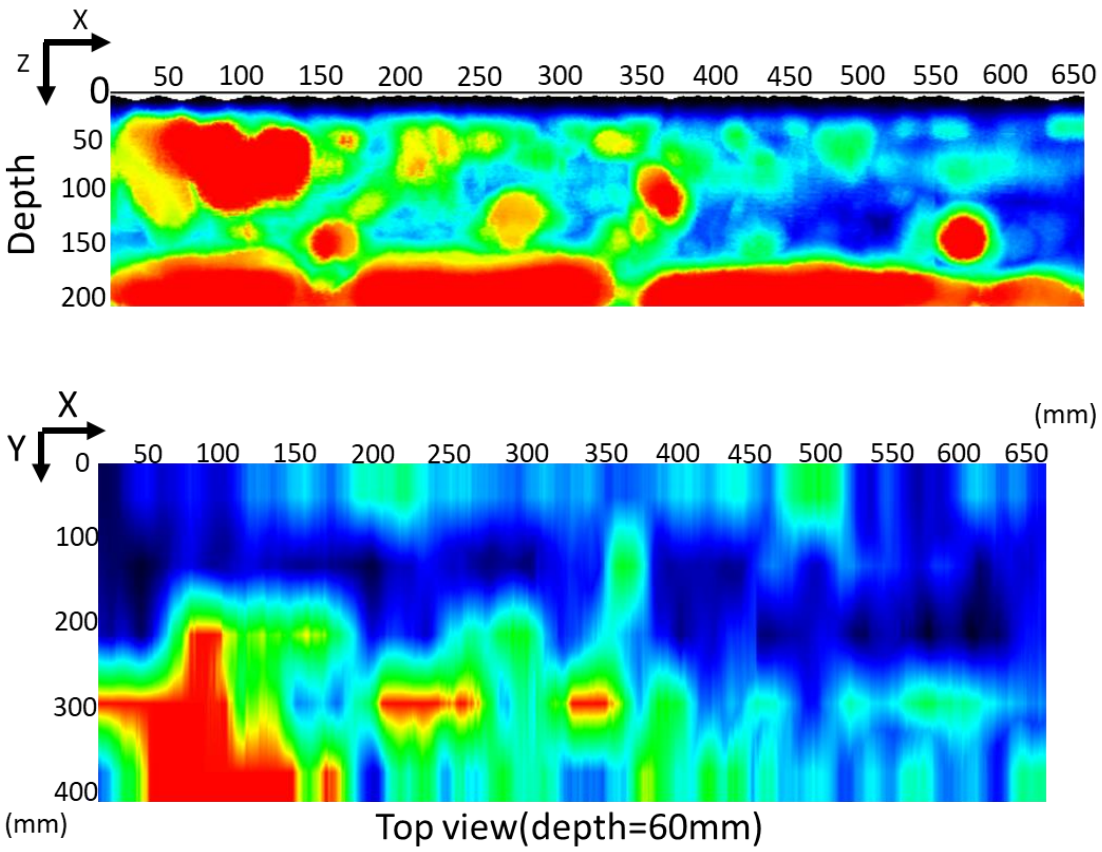
X
Z
0
50 100 150 200 250 300 350 400 450 500 550 600 650
Depth
50
100
150
200
X
Y
(mm)
0
50 100 150 200 250 300 350 400 450 500 550 600 650
100
200
300
400
(mm)
Top view(depth=60mm)
650
400
X
0
Y
Z
200
Space is 100mm
X
y
Concrete

(c)

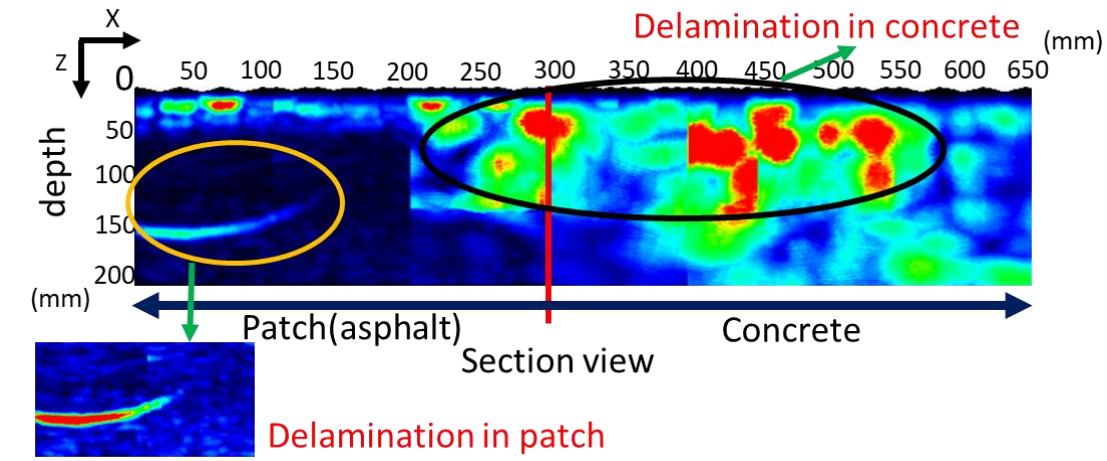
X
Z
0
50 100 150 200 250 300 350 400 450 500 550 600 650
(mm)
Delamination in concrete
depth
50
100
150
200
(mm)
Patch(asphalt)
Concrete
Section view
Delamination in patch

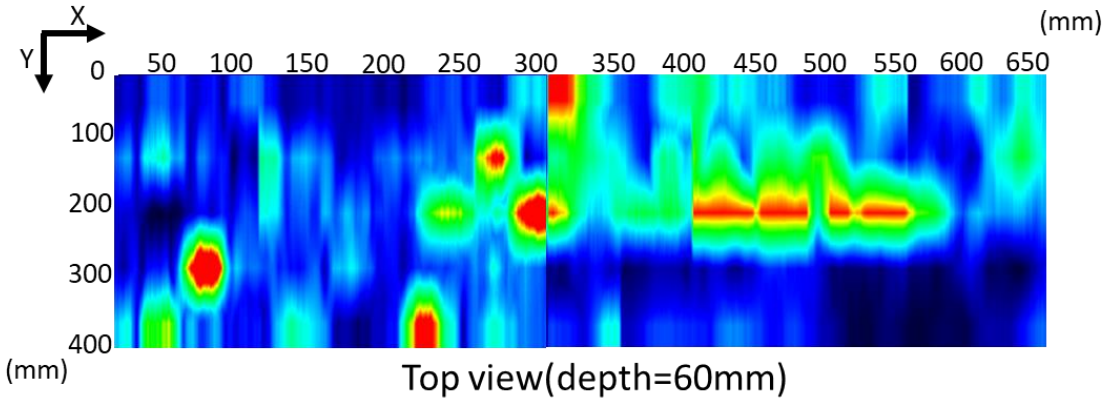
X
Y
0
50 100 150 200 250 300 350 400 450 500 550 600 650
(mm)
100
200
300
400
(mm)
Top view(depth=60mm)

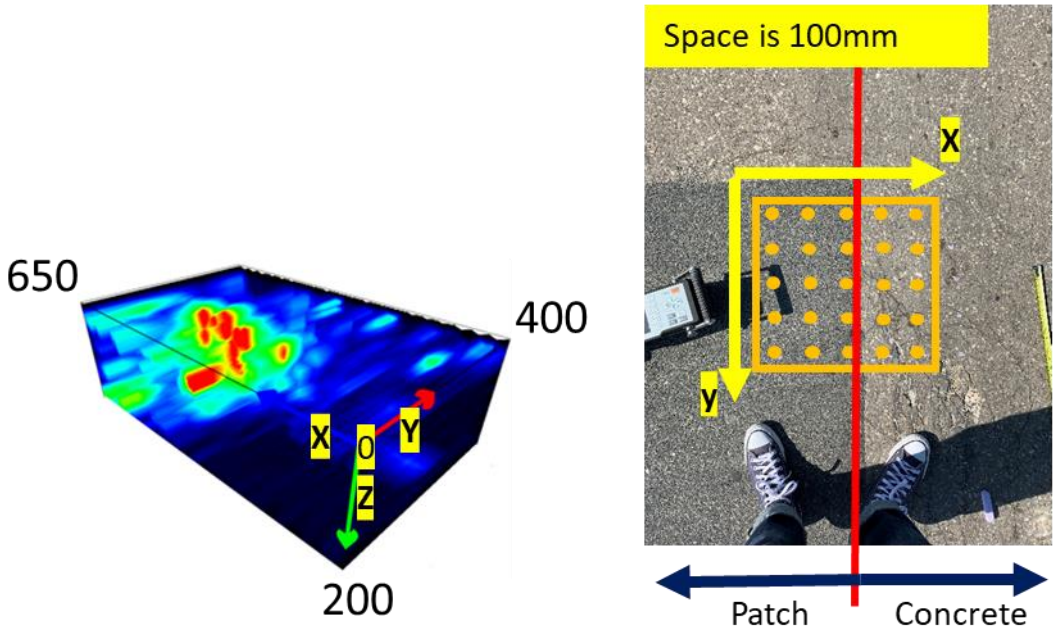
650
400
200
X
Y
Z
0
Space is 100mm
X
y
Patch
Concrete

(d)

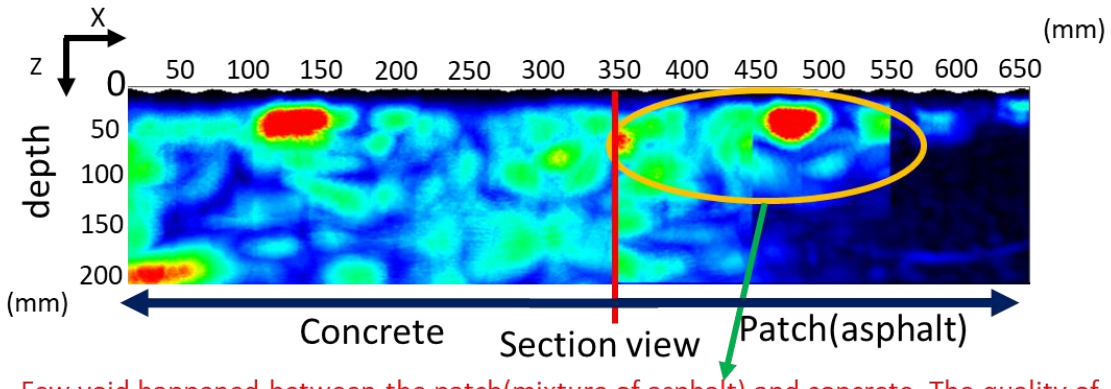

Few void happened between the patch(mixture of asphalt) and concrete. The quality of connection between patch and concrete become worse by time and loading.

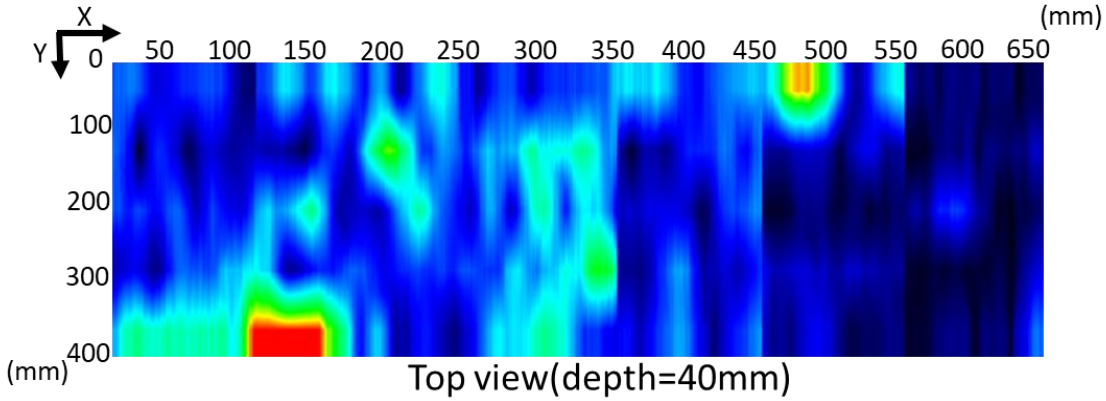

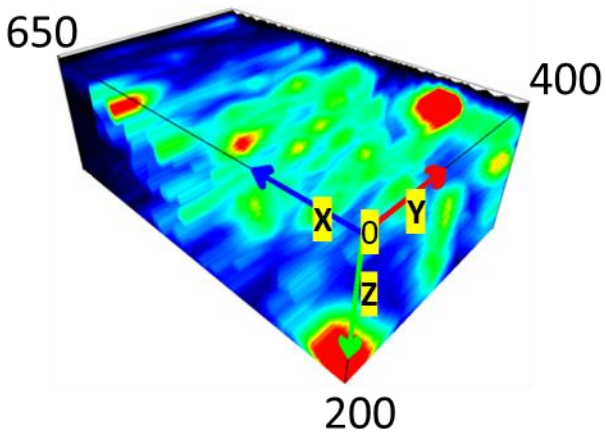

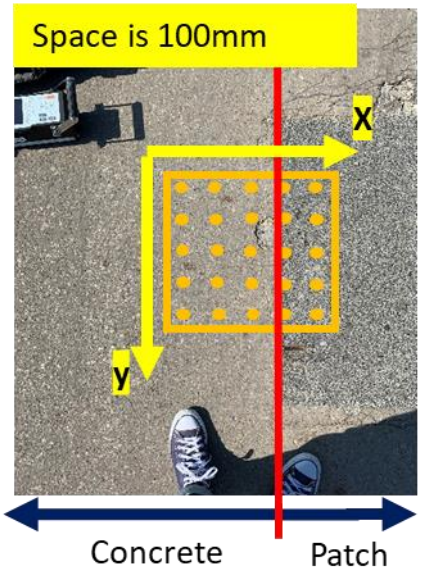

(e)

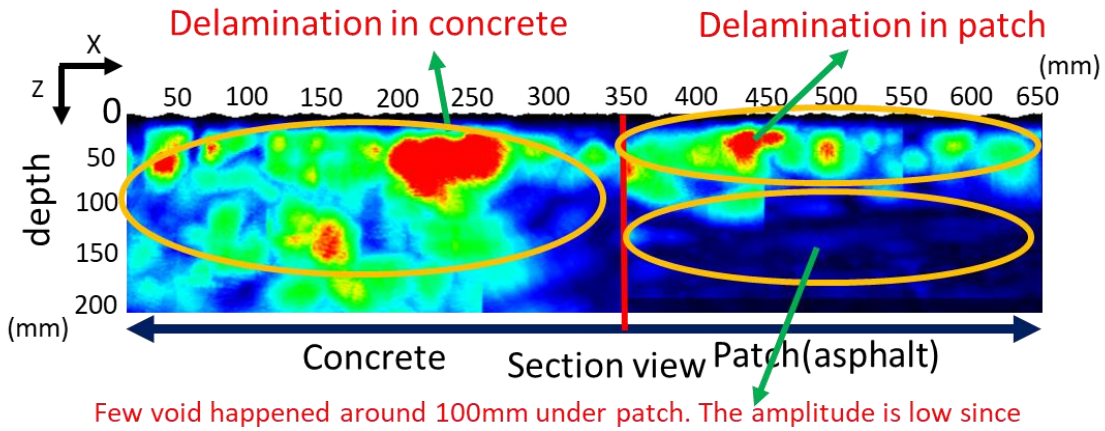

Few void happened around 100mm under patch. The amplitude is low since the energy scattered in patch.

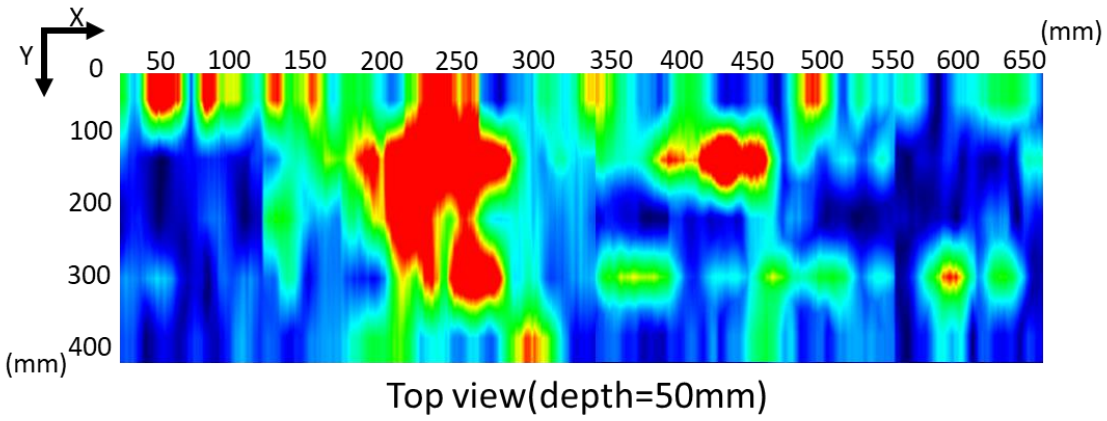

Top view(depth=50mm)

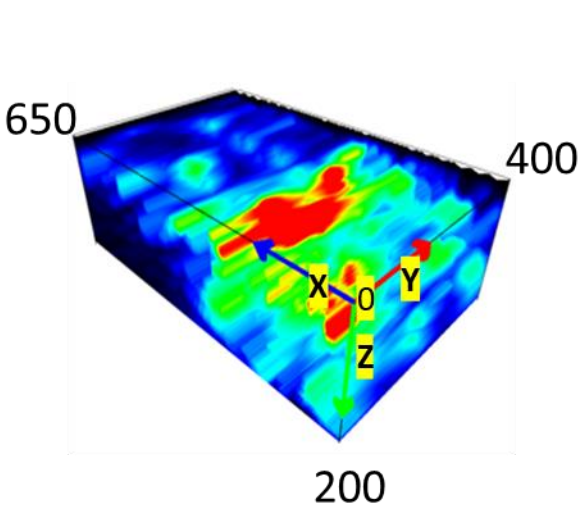

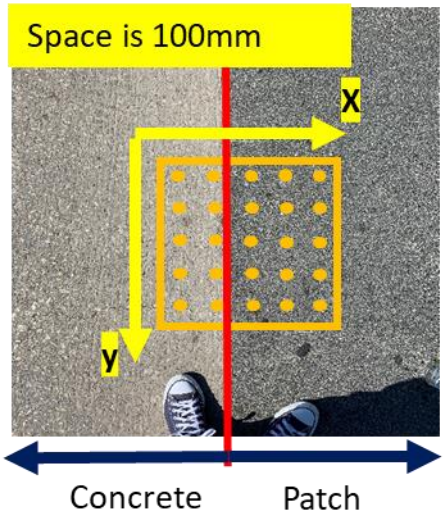

(f)

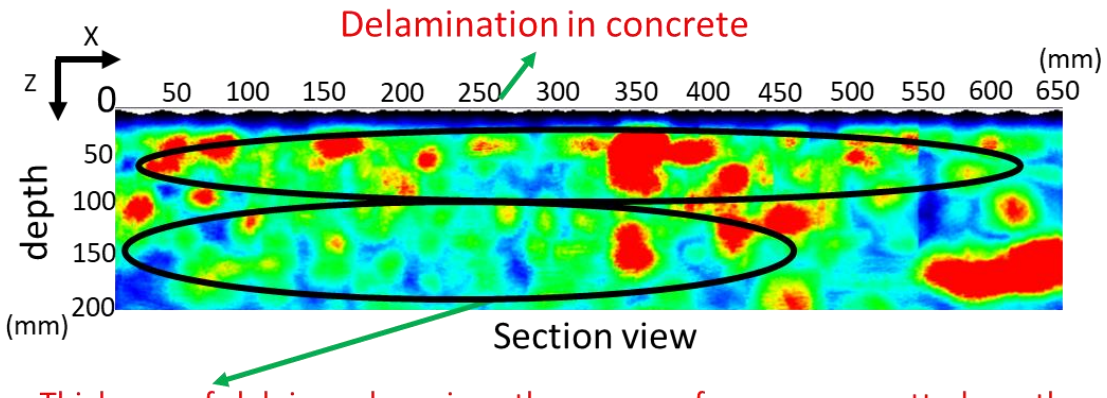
Delamination in concrete
X
Z
0
50 100 150 200 250 300 350 400 450 500 550 600 650
(mm)
depth
50
100
150
200
(mm)
Section view
Thickness of slab is unclear since the energy of waves are scatted mostly

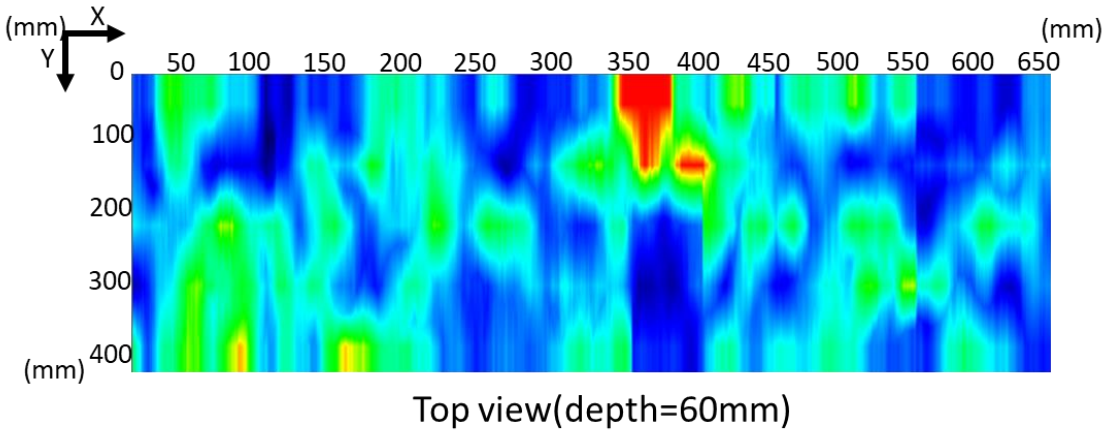
(mm)
X
Y
0
50 100 150 200 250 300 350 400 450 500 550 600 650
(mm)
100
200
300
400
(mm)
Top view(depth=60mm)

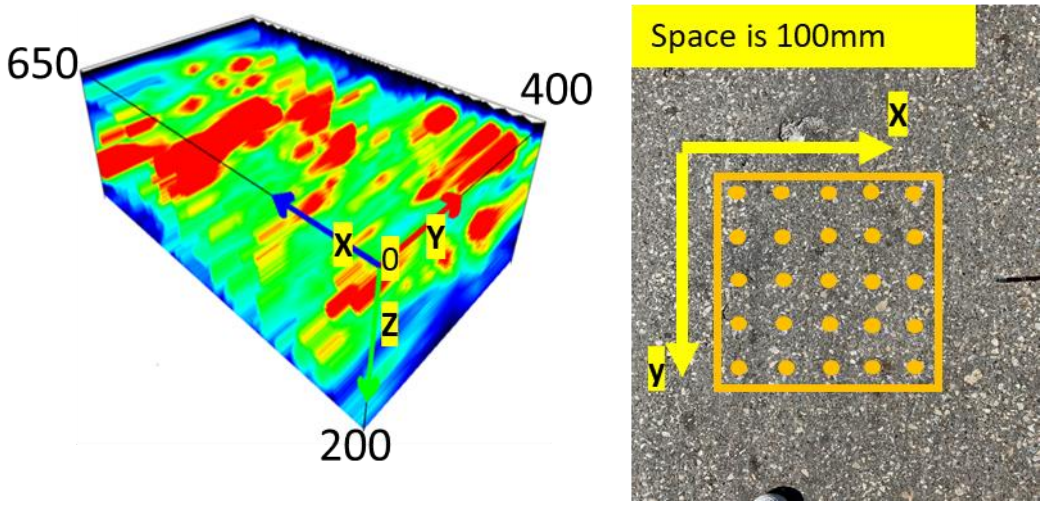
650
400
200
X
Y
Z
0
Space is 100mm
X
Y

(g)

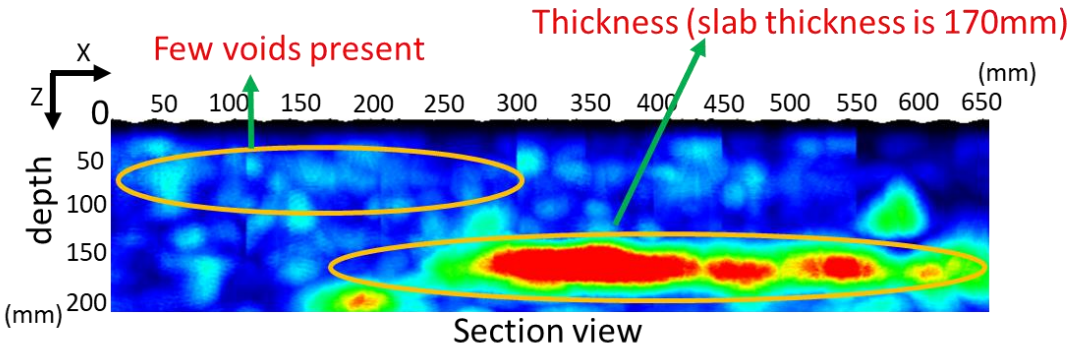

Section view

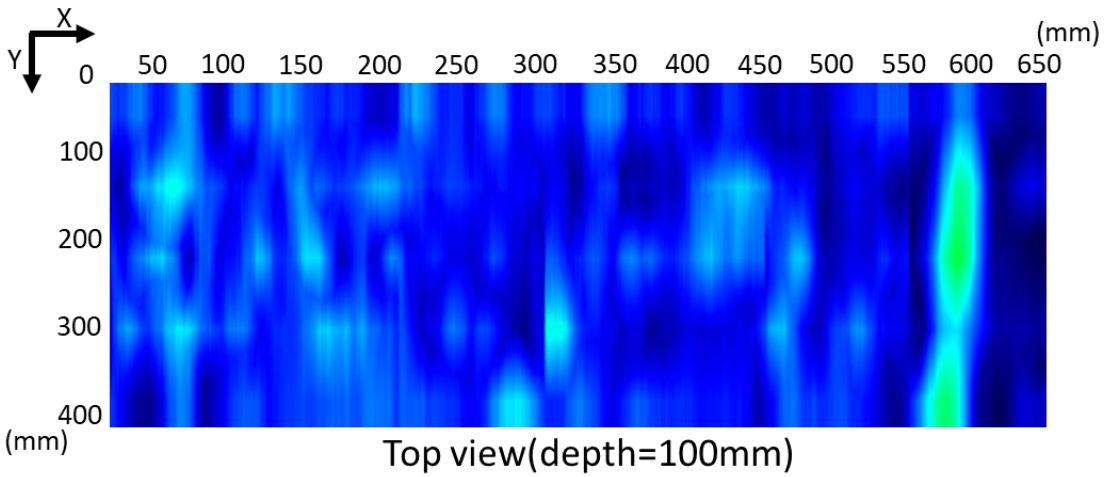

Top view(depth=100mm)

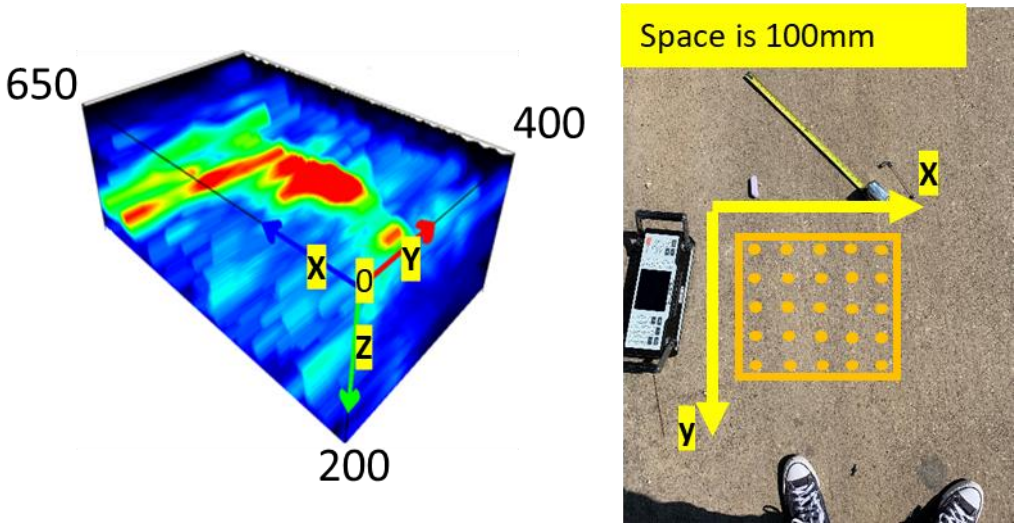

(h)

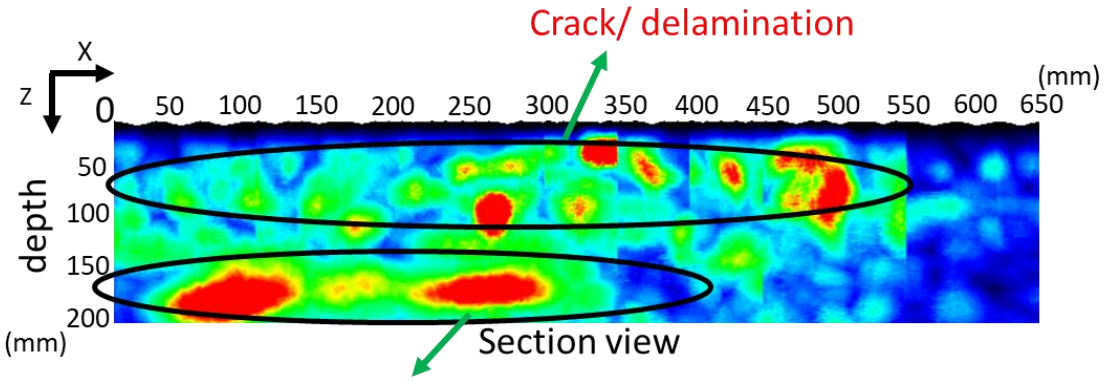

Thickness(slab thickness is 170mm). The thickness seems discontinuous since the energy scattered at the crack/delamination above.

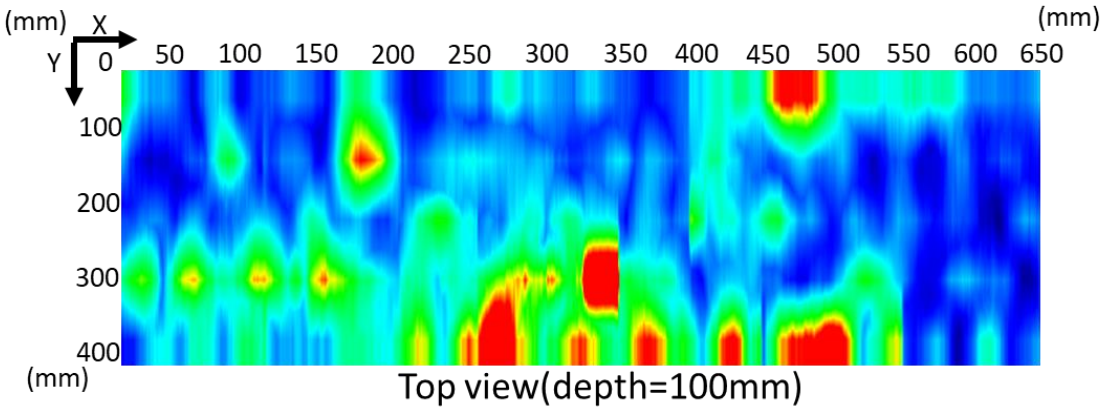

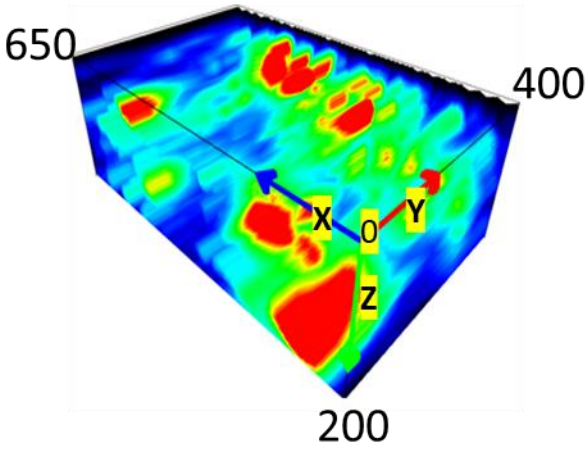

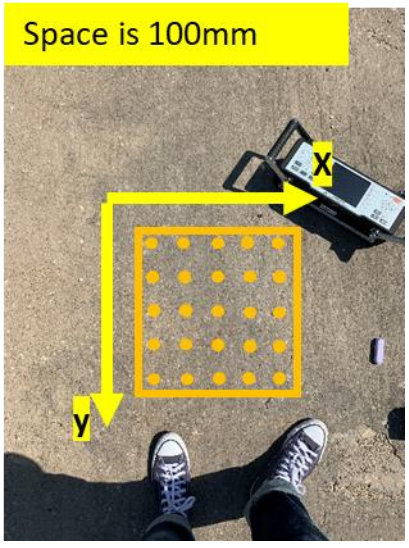

(i)

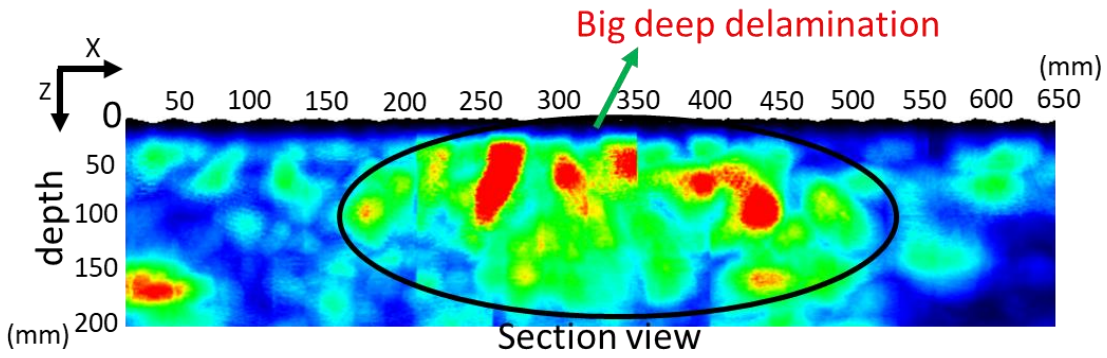
Big deep delamination
X
Z
0
50 100 150 200 250 300 350 400 450 500 550 600 650
(mm)
depth
50
100
150
200
(mm)
Section view

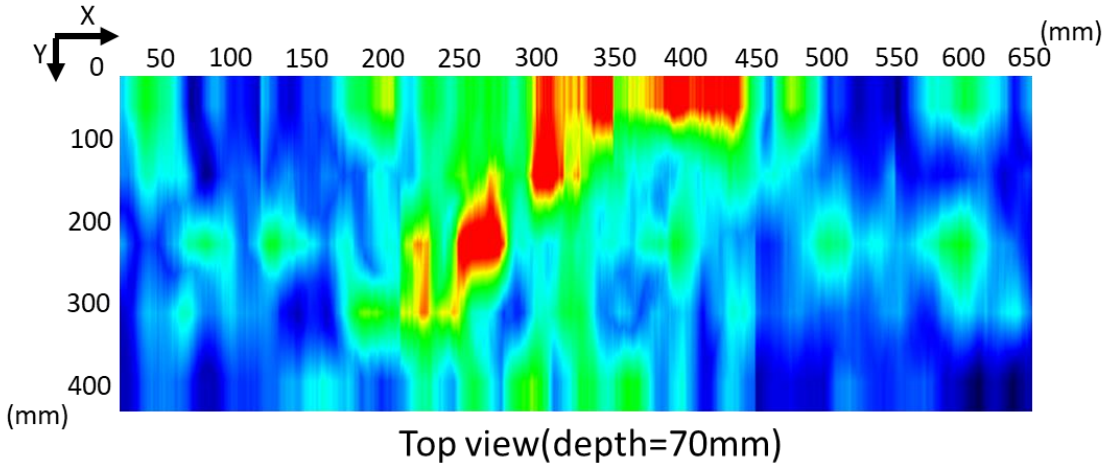
X
Y
0
50 100 150 200 250 300 350 400 450 500 550 600 650
(mm)
100
200
300
400
(mm)
Top view(depth=70mm)

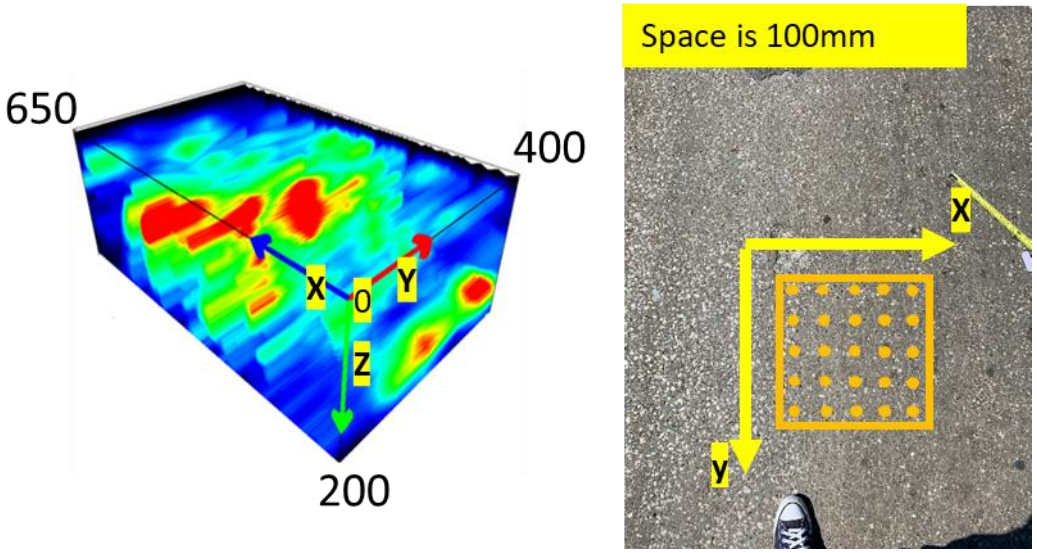
650
400
200
X
0
Y
Z
Space is 100mm
X
y

(j)

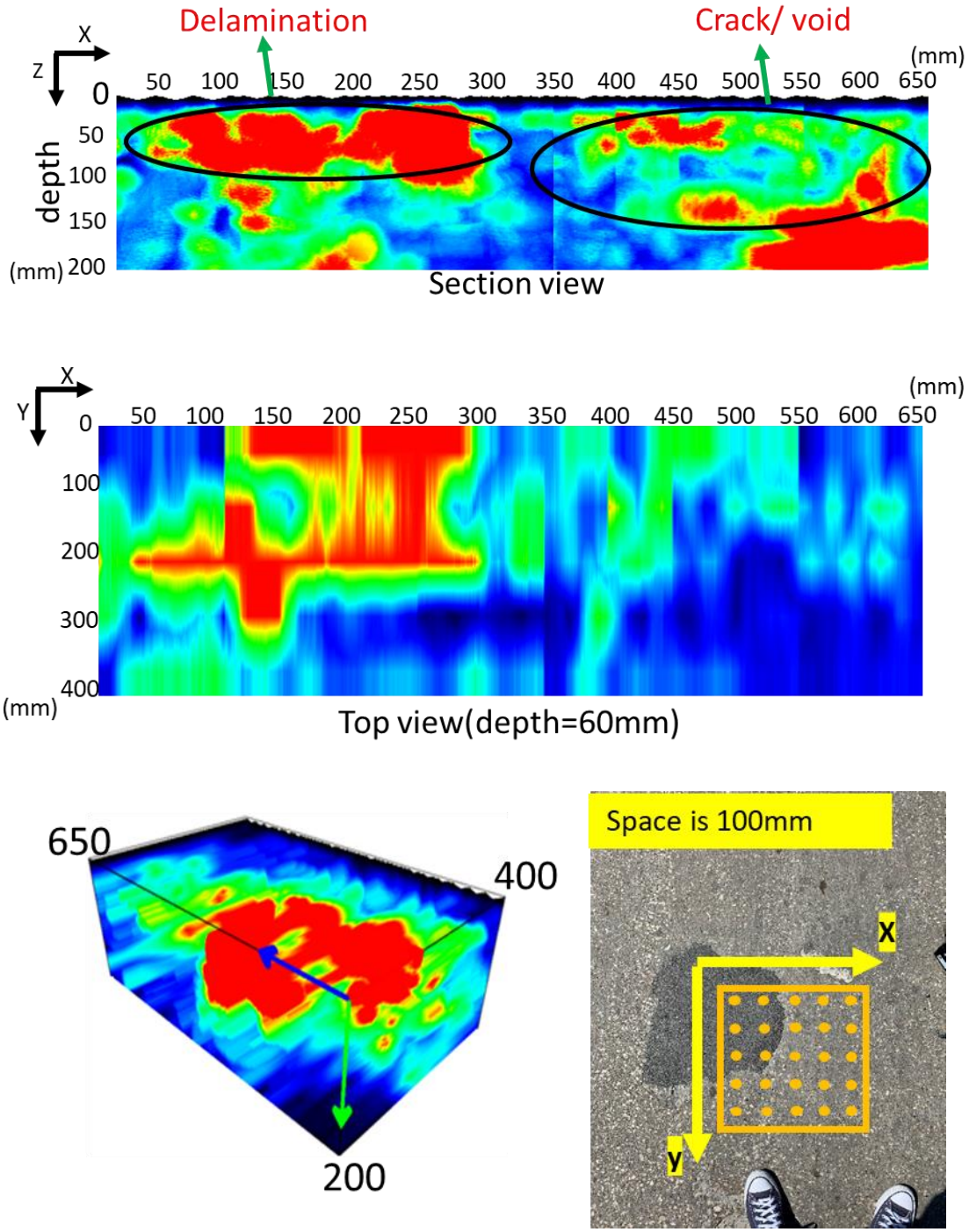

(l)

Figure 5.21 3-D ultrasonic tomography scanning: (a) Scanning points (b) 2-D, 3-D, and surface image of Point 1, (c) 2-D, 3-D, and surface image of Point 2, (d) 2-D, 3-D, and surface image of Point 4, (e) 2-D, 3-D, and surface image of Point 5, (f) 2-D, 3-D, and surface image of Point 6, (g) 2-D, 3-D, and surface image of Point 7, (h) 2-D, 3-D, and surface image of Point 8, (i) 2-D, 3-D, and surface image of Point 9, (k) 2-D, 3-D, and surface image of Point 10, and (l) 2-D, 3-D, and surface image of Point 11,

5.5.2 *Inspection of Bridge 2*

A 195 m long and 16 m wide concrete bridge in Texas, United States, was investigated in September 2020. This bridge was the newly constructed bridge in 2020. Eight-path (P1-P8) scans are designed to inspect the entire width of the bridge as shown in Figure 5.22 (a). Thus, the scanning area is the same as the bridge size, 195 m long and 16 m wide. The inspection was performed before the bridge carries traffic, as shown in the bridge image Figure 5.22 (b). Thus, no major surface defect is found in the visual inspection. There are a few surface-opening cracks, as shown in Figure 5.22 (c).

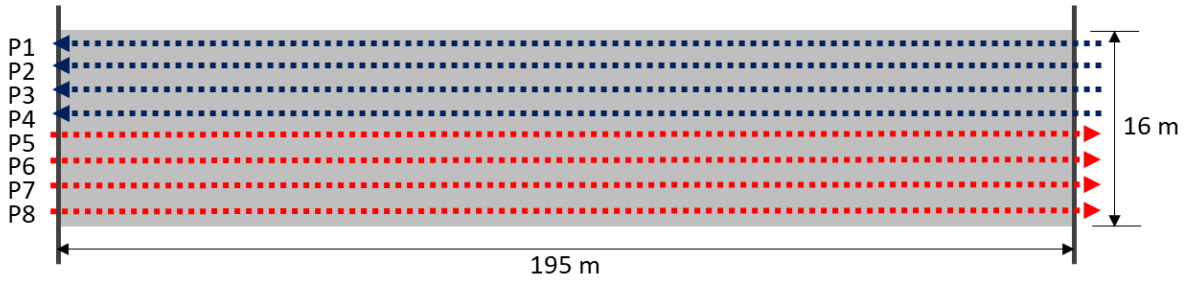

(a)

(b)

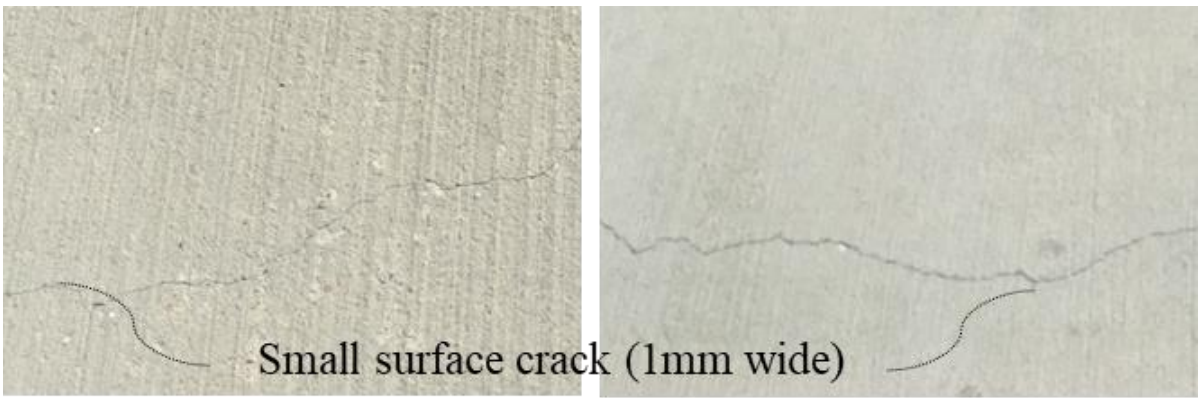

(c)

Figure 5.22. Bridge inspection paths and bridge images. Eight-path scans are performed to inspect 195 m × 16 m area before the bridge carries traffic. 1mm surface-opening cracks are detected on the bridge surface through the visual inspection.

No delamination and corroded reinforcement are detected from the bridge inspection as shown in Figure 5.23. Three vertical cracks are detected on the vertical crack map. The detected areas are identified to the surface-opening crack in the comparative study of the vertical crack map and video image.

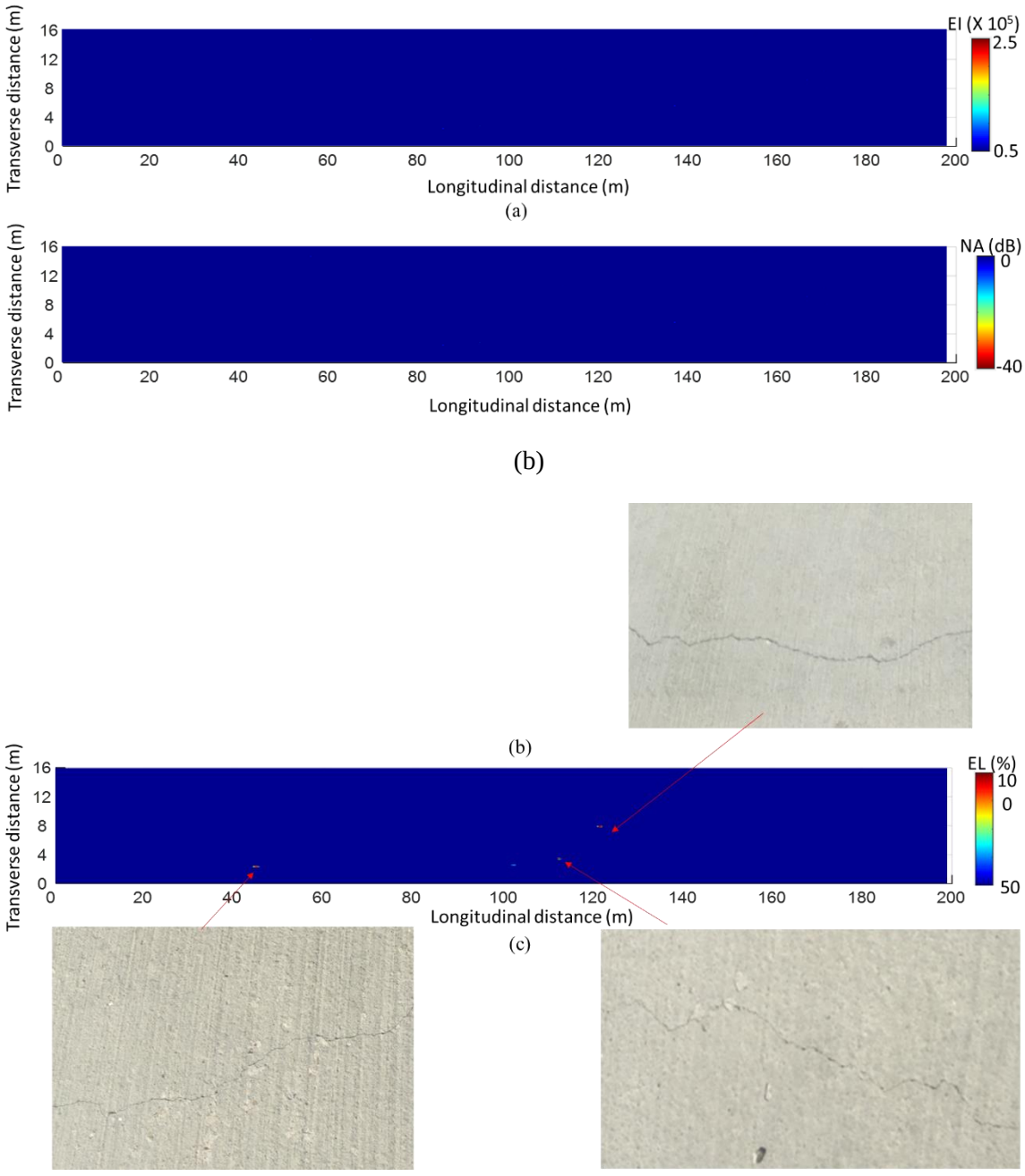

Figure 5.23. Inspection result of the second bridge: (a) delamination map (b) corrosion map. The inspection result indicates the bridge is in intact condition. Three surface-opening cracks are detected.

The 3-D ultrasonic tomography device scans the second bridge. The B-scan image indicates that the concrete and reinforcement of the second bridge are in an intact condition. The ultrasonic wave reflection on the bottom of the bridge deck shows about 200 mm depth.

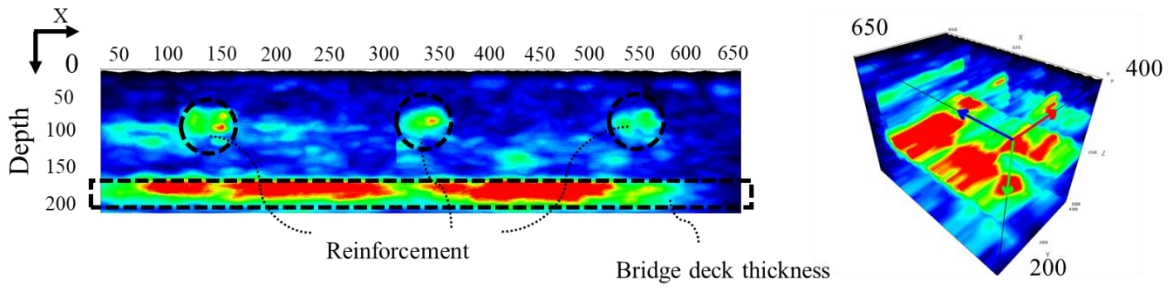

Figure 5.24. Ultrasonic tomography scanning result of second bridge: (a) concrete pavement B-scan image (cross-section view) and (b) 3-D tomography image. The scanned image shows precise thickness and reinforcement.

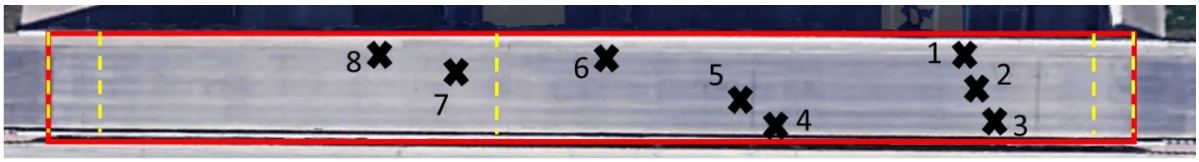
8
7
6
5
4
1
2
3

(a)

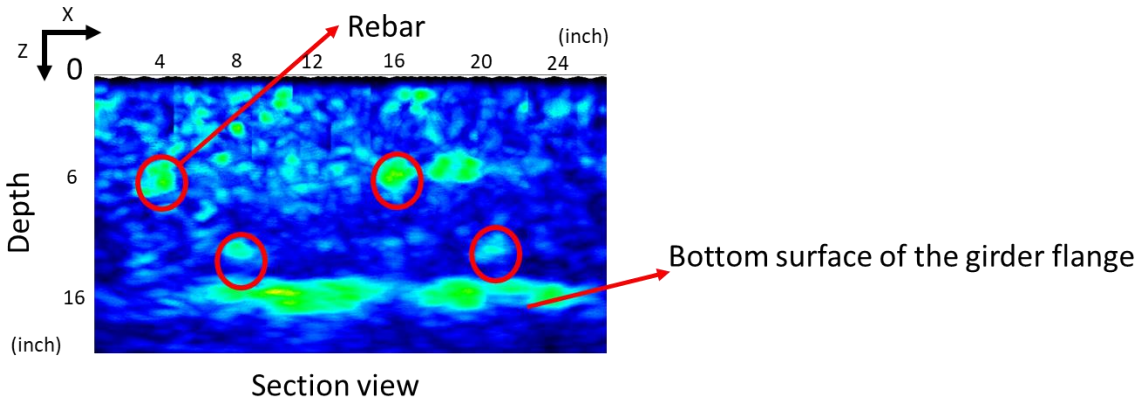
X
Z
0
4
8
12
16
20
24
(inch)
Rebar
Depth
6
16
(inch)
Bottom surface of the girder flange
Section view

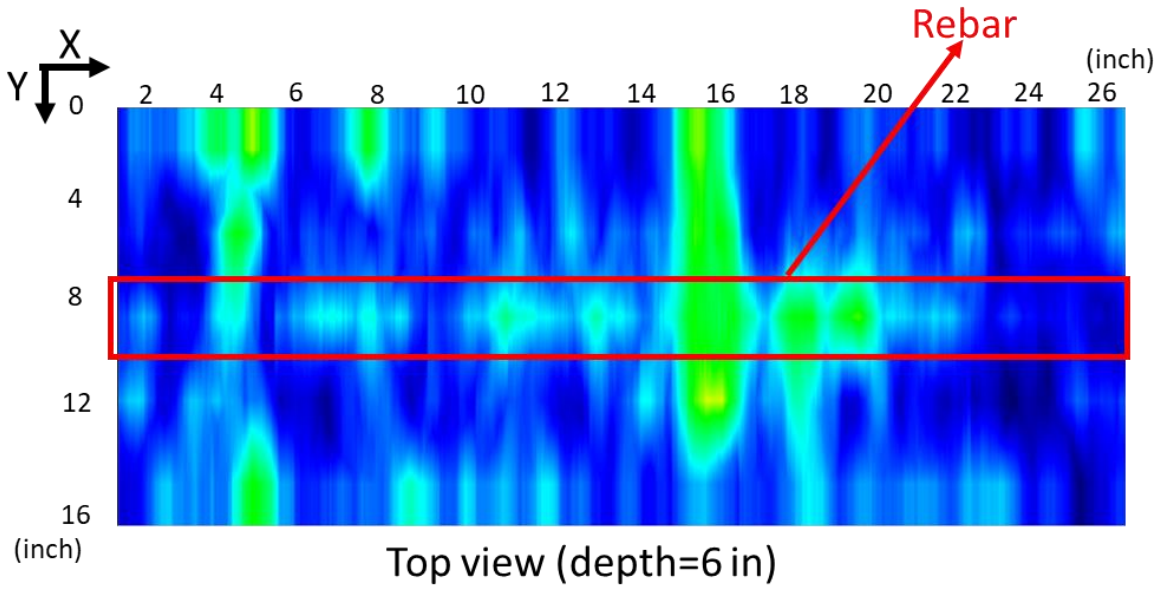
Rebar
X
Y
0
2
4
6
8
10
12
14
16
18
20
22
24
26
(inch)
4
8
12
16
(inch)
Top view (depth=6 in)

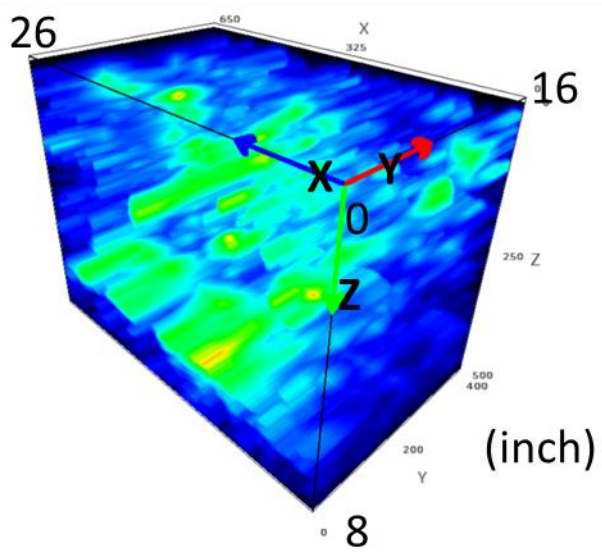
26
16
X
Y
0
Z
(inch)
8

(b)

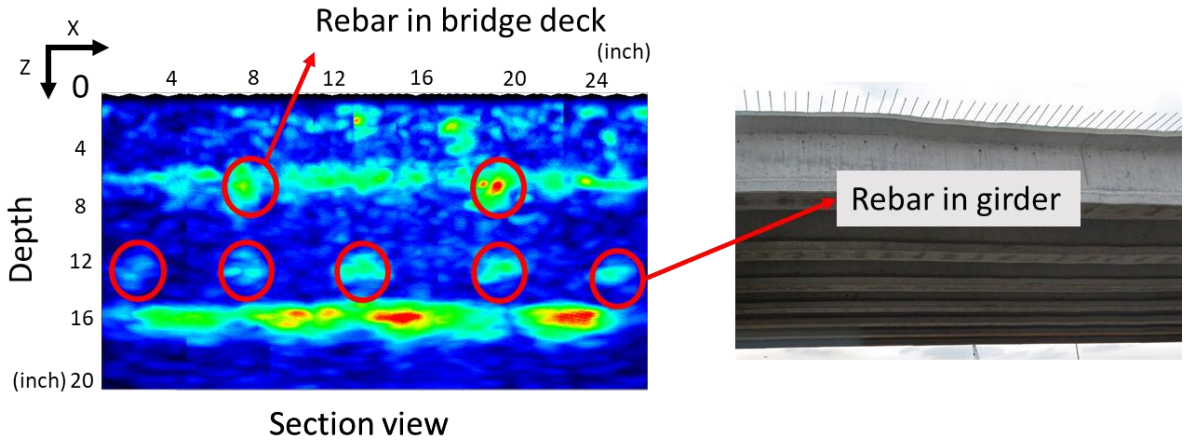
Rebar in bridge deck
(inch)
Depth
Section view
Rebar in girder

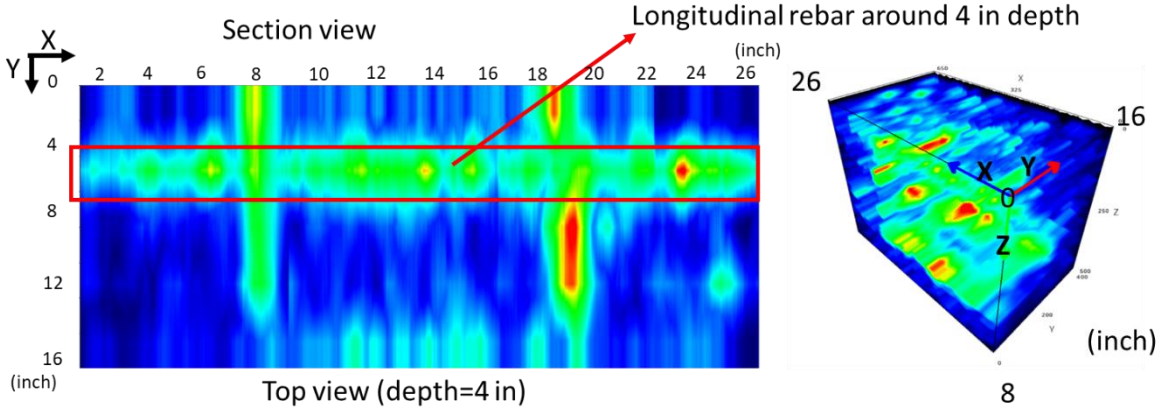
Section view
Longitudinal rebar around 4 in depth
(inch)
Top view (depth=4 in)
26
16
(inch)
8

(c)

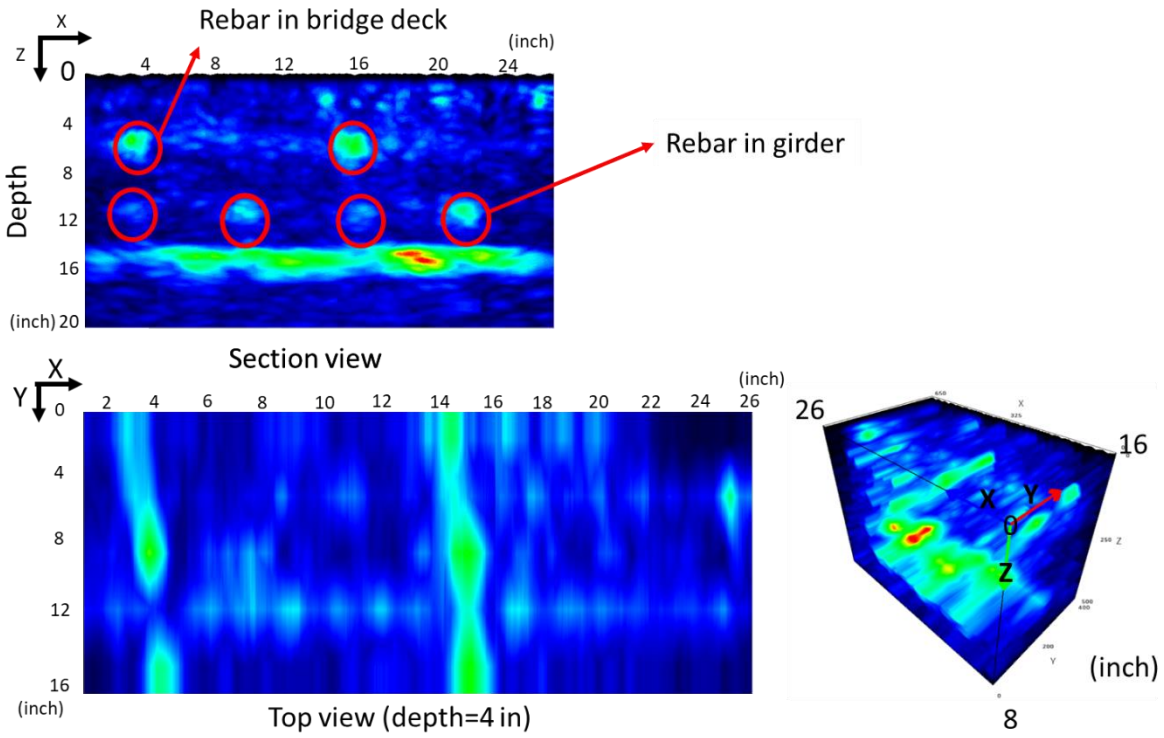
Rebar in bridge deck
Rebar in girder
Depth
(inch)
Section view
Top view (depth=4 in)
(inch)

(d)

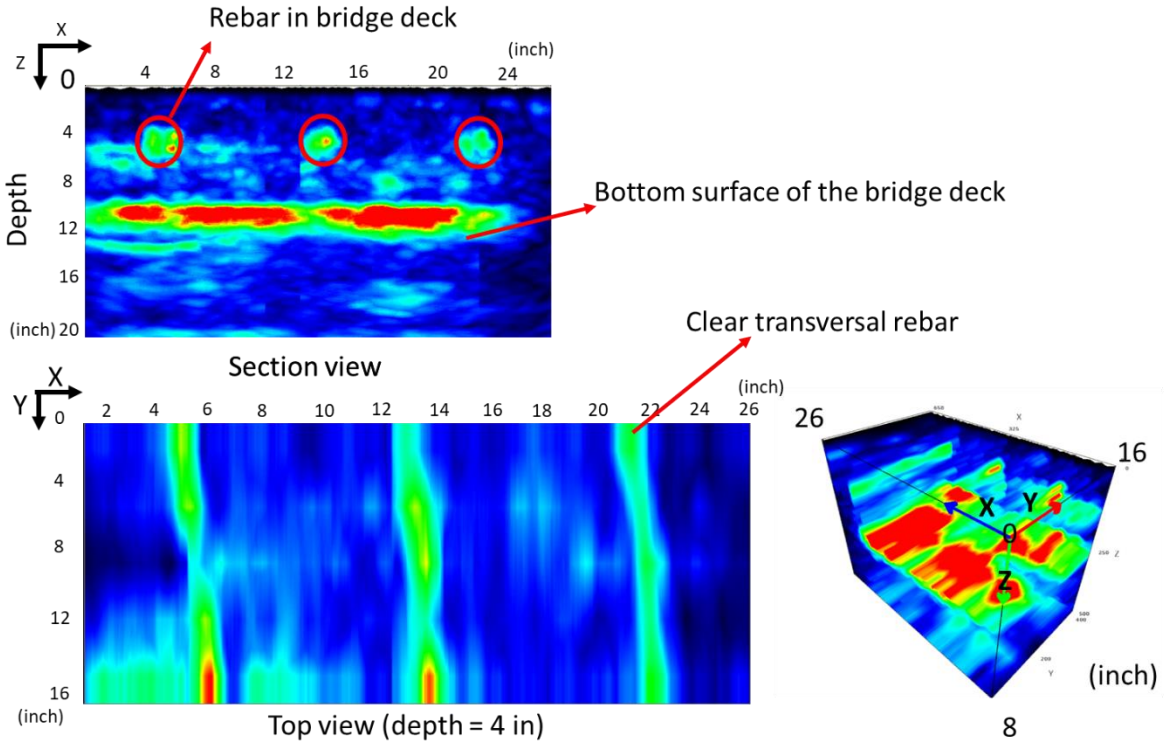
Rebar in bridge deck
Bottom surface of the bridge deck
Clear transversal rebar
Depth
(inch)
Section view
Top view (depth = 4 in)
(inch)

(e)

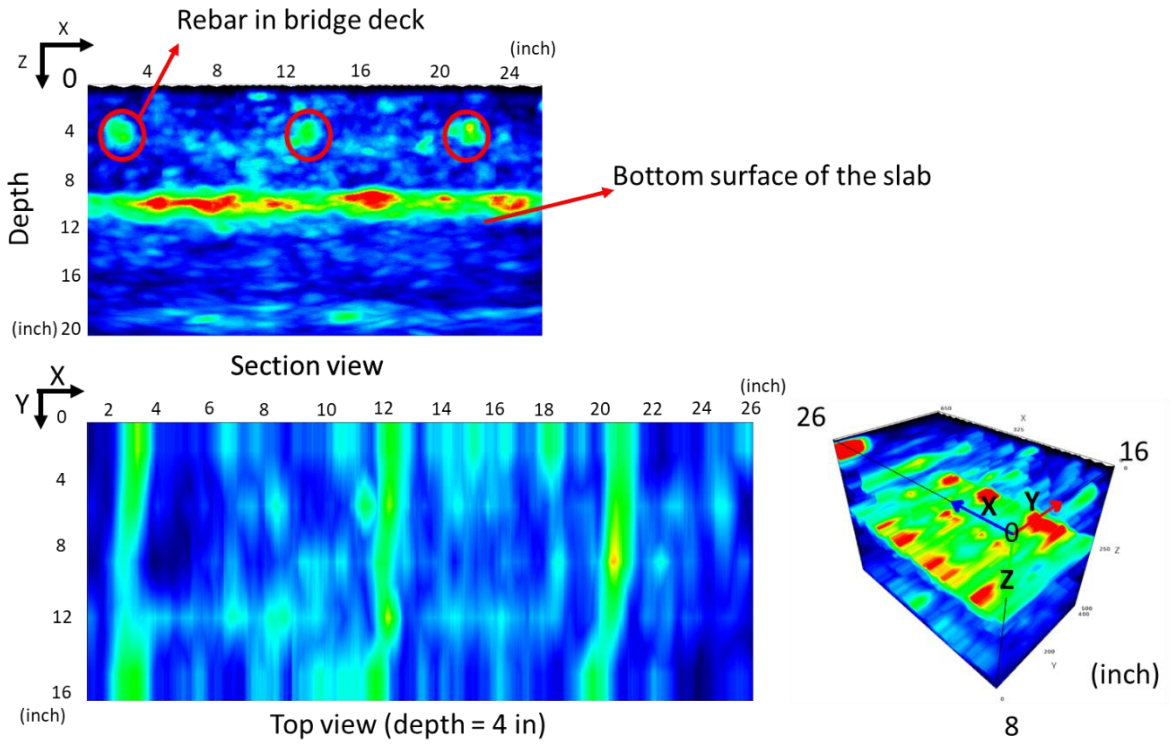
Rebar in bridge deck
Bottom surface of the slab
Depth
(inch)
Section view
Top view (depth = 4 in)
X
Y
Z
0
2 4 6 8 10 12 14 16 18 20 22 24 26
4 8 12 16 20
26
16
8

(f)

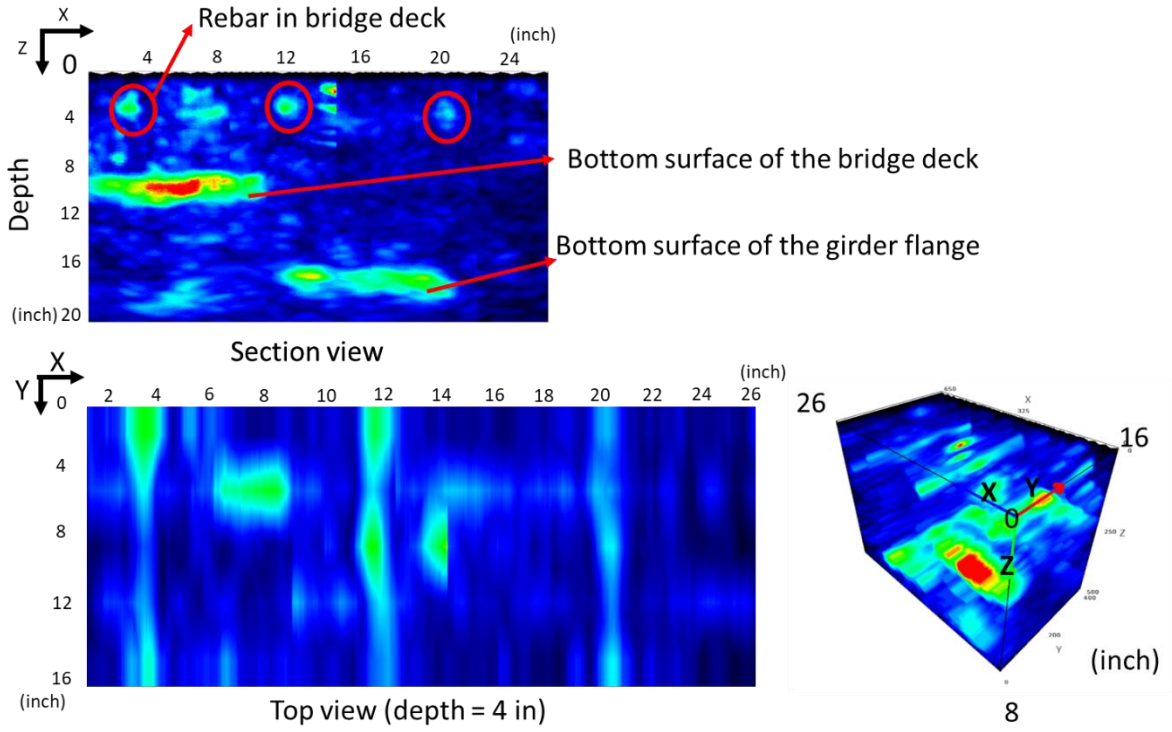
Rebar in bridge deck
Bottom surface of the bridge deck
Bottom surface of the girder flange
Depth
(inch)
Section view
Top view (depth = 4 in)
X
Y
Z
0
2 4 6 8 10 12 14 16 18 20 22 24 26
4 8 12 16 20
26
16
8

(g)

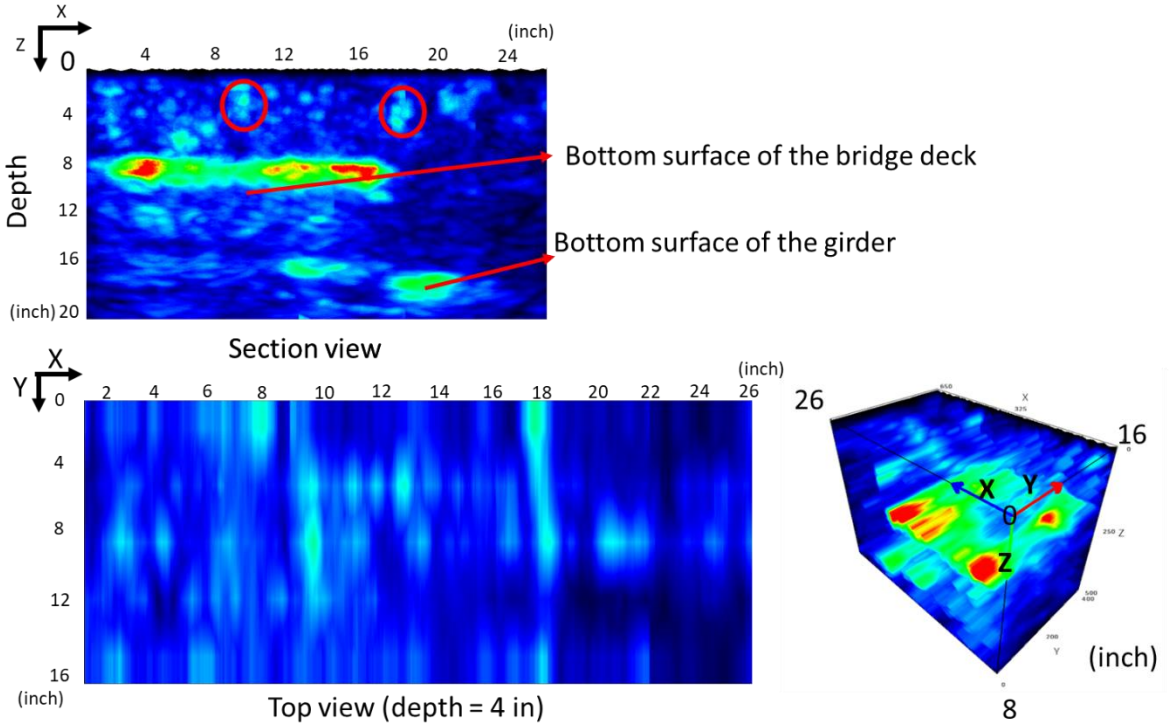
X
Z
0
(inch)
4 8 12 16 20 24
Depth
4
8
12
16
(inch) 20
Bottom surface of the bridge deck
Bottom surface of the girder
Section view
Y
X
0
(inch)
2 4 6 8 10 12 14 16 18 20 22 24 26
4
8
12
16
(inch)
Top view (depth = 4 in)
26
16
X
Y
0
Z
(inch)
8

(h)

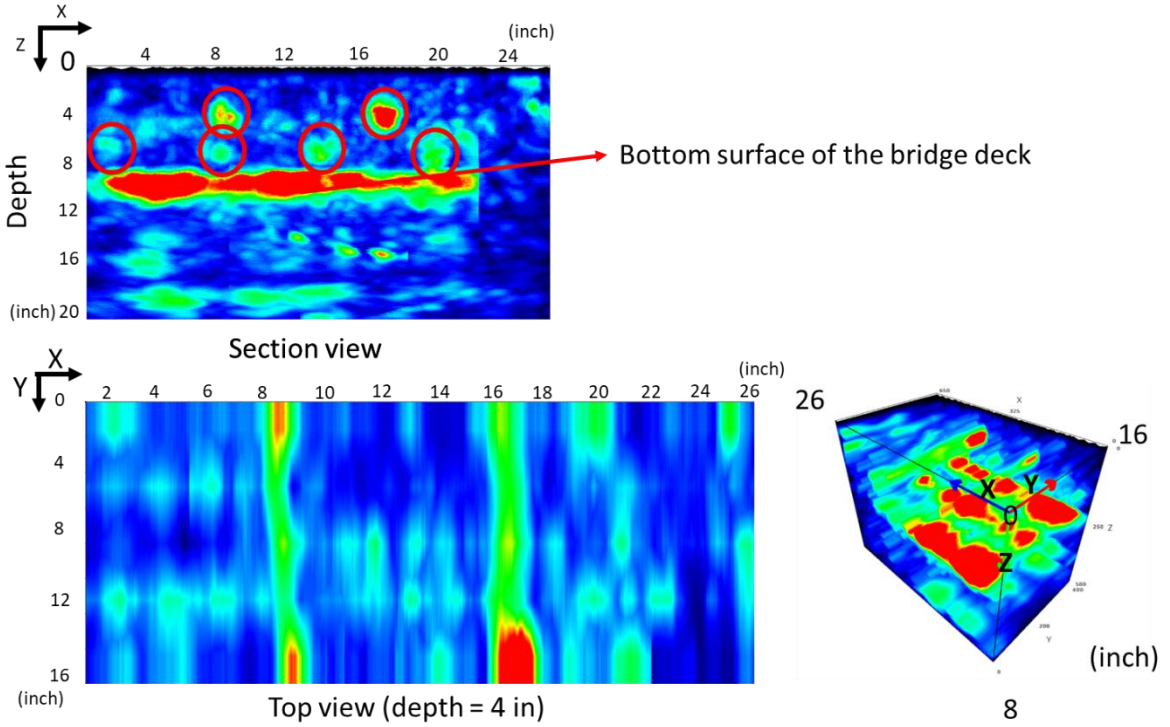
X
Z
0
(inch)
4 8 12 16 20 24
Depth
4
8
12
16
(inch) 20
Bottom surface of the bridge deck
Section view
Y
X
0
(inch)
2 4 6 8 10 12 14 16 18 20 22 24 26
4
8
12
16
(inch)
Top view (depth = 4 in)
26
16
X
Y
0
Z
(inch)
8

(i)

Figure 5.25. 3-D ultrasonic tomography scanning: (a) scanning points with GPS coordination, (b) 2-D and 3-D result of point 1, (c) 2-D and 3-D result of point 2, (d) 2-D and 3-D result of point 3, (e) 2-D and 3-D result of point 4, (f) 2-D and 3-D result of point 5, (g) 2-D and 3-D result of point 6, (h) 2-D and 3-D result of point 7, and (i) 2-D and 3-D result of point 9.

CHAPTER 6 CONCLUSION

The presented study mainly focuses on singular integral solutions to investigate the existing analytical model and to provide a new analytical solution. The study also presents an efficient dynamic FE analysis with an optimized model configuration for wave separation. The simulation that uniquely offers the wave scattering phenomena is designed to obtain the displacement value under the same given conditions as with the analytical model. The data from the simulation results are used to demonstrate the viability of the wave scattering model. The obtained analytical solutions with displacement variation curves are investigated by defining Pearson's correlation of the FE results. Finally, the result shows the significantly correlated displacement variation of the proposed model with the FE results. The obtained results are discussed in terms of the curved shape and the correlation coefficient between the analytical model and FE simulation. The following conclusions are drawn based on the analytical solutions and FE simulation results, and discussion presented in the paper.

- The computation time of the analytical model is much shorter than the FE simulation. In the paper, 177 FE models are created and simulated in order to provide an adequate resolution of the displacement variation curves. Each simulation computing time is about 20 minutes, and post-processing is required, while the numerical solution for the analytical model takes a few seconds without designing and post-processing time.
- Regardless of crack depth and size, a similar amount of wave scattering energy occurs in the same *a/b* ratio.
- The smaller crack sized model has a peak value at the relatively higher $k_R a$. Since the lower frequency waves can pass through the smaller length of the crack, it shows lesser wave scattering in the lower $k_R a$. Therefore, the peak displacement variation is formed in the higher $k_R a$ in the case of the smaller crack model.

- The Gauss-Legendre quadrature integration method shows the highest correlation coefficient values, with an averaged value of 0.94 compared to all considered models, between its analytical model and the FE simulation.
- The analytical model can provide an efficient and reliable approach to solving the parametric relationship of wave scattering. Further studies are needed to investigate the limits of applicability of the developed analytical formulation, such as nonlinearity.

We demonstrate the internal vertical crack evaluation approach using the SWS-IVC model. Analytical, numerical, and experimental studies are performed to verify the approach by presenting reliable response variation curves. The analytical study for RVA is performed by solving five different singular integration methods. The FE simulations are designed by applying various incident wave frequencies with cracked concrete pipe properties. In addition, two different experimental analyses, the RVA method and the MSA, are investigated for practical crack estimation. The RVA method is based on wave response variation curves that influenced by $k_R a$. The experimental data in MSA performed to provide the relative wave energy loss influenced by internal vertical crack geometry. The following conclusions about the verification and comparison study in the RVA approach and crack evaluation concept using both RVA and MSA are presented in this paper:

- In the analytical study of the SWS-IVC model, the model using the Gauss-Legendre quadrature integration method shows the highest correlation coefficient, 0.97, with a response variation from the FE simulation result and 0.9 with the experiment result.
- Response variations obtained from experiments by the same crack but on the opposite side of receiving point show a significant similarity (correlation coefficient of 0.85). It implies that the same response variation tendency can be obtained with an in-situ experiment with ensured impact and receive distances from the existing crack.

- The analytical SWS-IVC model is verified with the obtained response variations from FE simulations and experiments with a correlation coefficient of 0.97 and 0.9, respectively.
- The crack evaluation by the depth-to-crack estimation can be performed with RVA using surface wave scattering and MSA influenced by the internal vertical crack. If feasible, the degree of the energy loss obtained from the MSA test can help to decide one of the depth-to-cracks from the RVA result by finding two matched depth-to-cracks with response variation from the single in-situ experiment.
- Further research of RVA from the SWS-IVC model and experiment can be considered by applying guided wave and multiple surface wave detections with different parameters (e.g., concrete thickness, sensor, crack, impact distances). In addition, the supplementary factors of the analytical model in terms of wave attenuation by the material homogeneity of the medium can reinforce the analytical SWS-IVC model. In further research, the proposed internal crack evaluation system can deeply investigate the concrete pavement (e.g., airport runway, unreinforced road pavement, or pedestrian walkway), which mostly shows the internal vertical crack at the middle of pavement length.

In the third, the ACE system is developed for rapid inspection of the bridge deck to detect delamination, vertical crack, and corroded reinforcement. The ACES deploys the DSBI system, MAS unit, and AHAS platform to obtain high inspection quality in terms of data collection resolution, wave energy, consistent wave source. The high inspection quality can be obtained by providing higher PRF, proper impact design, and high-resolution sensor deployment. The developed system is modified and verified by laboratory tests. In addition, two highway bridge field inspections are performed with the developed ACE system. The following conclusions are presented from the laboratory and field test using the ACE system:

- Based on the laboratory test results, the developed DSBI system shows the high PRF and impact energy to detect delamination of different sizes by providing a sufficient incident wave to generate

the flexural vibration mode. In addition, the sufficient incident wave allows to detect the vertical crack by providing a proper surface wave propagation for measuring the wave attenuation.

- The MAS unit design allows for 30 cm resolution for delamination detection and 10 cm resolution for vertical crack detection. These data collection resolution helps to obtain a high inspection quality and reliable inspection result by presenting the high resolution of the colormaps.
- The developed ACE system using the DSBI system and AHAS platform achieves the faster scanning speed and nonstop inspection system. These achievements significantly decrease the inspection time and increase safety by reducing the exposure of inspectors to live traffic. In addition, the proposed post-processing algorithm allows to eliminate the subjectivity associated detection with traditional sounding methods,
- The chargeable and adjustable frame design allows to the installation of the additional MAS unit. The additional MAS unit increases the data collection resolution by providing the additional MAS to impact and receive.

REFERENCES

Achenbach, J. D. (2000). "Quantitative nondestructive evaluation." *International Journal of Solids and Structures*, 37(1–2), 13–27.

Achenbach, J. D., and Brind, R. J. (1981). "Scattering of surface waves by a sub-surface crack." *Journal of Sound and Vibration*, 76(1), 43–56.

Achenbach, J. D., Brind, R. J., and Norris, A. (1981). "Scattering by Surface-Breaking and Sub-Surface Cracks." *Proceedings of the DARPA/AFWAL Review of Progress in Quantitative NDE*, (January).

Achenbach, J. D., Lin, W., and Keer, L. M. (1983). "Surface Waves due to Scattering by a Near-Surface Parallel Crack." *IEEE Transactions on Sonics and Ultrasonics*, 30(4), 270–276.

Achenbach, J. D., Sotiropoulos, D. A., and Zhu, H. (1987). "Characterization of cracks from ultrasonic scattering data." *Journal of Applied Mechanics, Transactions ASME*, 54(4), 754–760.

Aggelis, D. G., Kordatos, E. Z., Soulioti, D. V., and Matikas, T. E. (2010). "Combined use of thermography and ultrasound for the characterization of subsurface cracks in concrete." *Construction and Building Materials*, Elsevier Ltd, 24(10), 1888–1897.

Aggelis, D. G., Kordatos, E. Z., Strantza, M., Soulioti, D. V., and Matikas, T. E. (2011). "NDT approach for characterization of subsurface cracks in concrete." *Construction and Building Materials*, Elsevier Ltd, 25(7), 3089–3097.

Ávila-Carrera, R., Rodríguez-Castellanos, A., Valle-Molina, C., Sánchez-Sesma, F. J., Luzón, F., and González-Flores, E. (2016). "Numerical simulation of multiple scattering of P and SV waves caused by near-surface parallel cracks." *Geofisica Internacional*, 55(4), 275–291.

Barnes, C. L., Trottier, J. F., and Forgeron, D. (2008). "Improved concrete bridge deck evaluation using GPR by accounting for signal depth-amplitude effects." *NDT and E International*, 41(6), 427–433.

Brockhaus, S., Ginten, M., Klein, S., Teckert, M., Stawicki, O., Oevermann, D., Meyer, S., and Storey, D. (2014). *In-line inspection (ILI) methods for detecting corrosion in underground pipelines*. *Underground Pipeline Corrosion: Detection, Analysis and Prevention*, Woodhead Publishing Limited.

Çam, E., Orhan, S., and Lüy, M. (2005). "An analysis of cracked beam structure using impact echo method." *NDT and E International*, 38(5), 368–373.

Cao, L., and Sendur, K. (2019). "Surface roughness effects on the broadband reflection for refractory metals and polar dielectrics." *Materials*, 12(19).

Committee224 ACI. (2007). *224.1R-07: Causes, Evaluation, and Repair of Cracks in Concrete Structures*. Farmington Hills, MI :American Concrete Institute.

Dinh, K., Gucunski, N., and Zayed, T. (2019). "Automated visualization of concrete bridge deck condition from GPR data." *NDT and E International*, Elsevier Ltd, 102(June 2018), 120–128.

Dorafshan, S., and Azari, H. (2020). "Deep learning models for bridge deck evaluation using impact echo." *Construction and Building Materials*, Elsevier Ltd, 263, 120109.

Egghe, L., and Leydesdorff, L. (2009). "The Relation Between Pearson's Correlation Coefficient r and Salton's Cosine Measure Leo." *Journal of the American Society for Information Science and Technology*, 60(5), 1027–1036.

Erdogan, F., Gupta, G. D., and Cook, T. S. (1973). "Numerical solution of singular integral equations." *Methods of analysis and soultions of crack problems*, Springer, Dordrecht, 368–425.

Farwig, R., Kozono, H., and Sohr, H. (2007). "On the Helmholtz decomposition in general unbounded domains." *Archiv der Mathematik*, 88(3), 239–248.

Giurgiutiu, V. (2012). *Structural Health Monitoring with Piezoelectric waffer active sensors*.

Gooch, D. J. (2007). "5.07 - Remnant creep life prediction in ferritic materials." *Comprehensive Structural*

Integrity, 5, 309–359.

Gregory, R. D. (1975). "The non-existence of standing modes in certain problems of linear elasticity." *Mathematical Proceedings of the Cambridge Philosophical Society*, 77(2), 385–404.

Guthrie, W. S., Larsen, J. L., Baxter, J. S., and Mazzeo, B. A. (2019). "Automated air-coupled impact-echo testing of a concrete bridge deck from a continuously moving platform." *Journal of Nondestructive Evaluation*, Springer US, 38(1), 1–8.

Ham, S., and Popovics, J. S. (2015a). "Application of contactless ultrasound toward automated inspection of concrete structures." *Automation in Construction*, Elsevier B.V., 58, 155–164.

Ham, S., and Popovics, J. S. (2015b). "Application of micro-electro-mechanical sensors contactless NDT of concrete structures." *Sensors (Switzerland)*, 15(4), 9078–9096.

Ham, S., and Popovics, J. S. (2015c). "Contactless ultrasonic scanning approach toward automated inspection of concrete structures." *Automation in Construction*.

Ham, S., Song, H., Oelze, M. L., and Popovics, J. S. (2017). "A contactless ultrasonic surface wave approach to characterize distributed cracking damage in concrete." *Ultrasonics*, Elsevier B.V., 75, 46–57.

Harrer, A., and Gaudette, P. (2019). "Challenges of preserving modernist concrete." *MATEC Web of Conferences*, 289, 07003.

Hassan, W., and Veronesi, W. (2003). "Finite element analysis of Rayleigh wave interaction with finite-size, surface-breaking cracks." *Ultrasonics*, 41(1), 41–52.

Hendricks, L. J., Baxter, J. S., Chou, Y., Thomas, M., Boekweg, E., Guthrie, W. S., and Mazzeo, B. A. (2020). "High-Speed acoustic impact-echo sounding of concrete bridge decks." *Journal of Nondestructive Evaluation*, Springer US, 39(3), 1–12.

Hévin, G., Abraham, O., Pedersen, H. A., and Campillo, M. (1998). "Characterisation of surface cracks

with rayleigh waves: A numerical model." *NDT and E International*, 31(4), 289–297.

In, C. W., Arne, K., Kim, J. Y., Kurtis, K. E., and Jacobs, L. J. (2017). "Estimation of crack depth in concrete using diffuse ultrasound: validation in cracked concrete beams." *Journal of Nondestructive Evaluation*, Springer US, 36(1), 1–9.

Jang, K., and An, Y. K. (2018). "Multiple crack evaluation on concrete using a line laser thermography scanning system." *Smart Structures and Systems*, 22(2), 201–207.

Ji, X., Hou, Y., Chen, Y., and Zhen, Y. (2019). "Attenuation of acoustic wave excited by piezoelectric aggregate in asphalt pavement and its application to monitor concealed cracks." *Construction and Building Materials*, Elsevier Ltd, 216, 58–67.

Kandil, K. S., Nemir, M. T., Ellobody, E. A., and Shahin, R. I. (2014). "Strain Rate Effect on the Response of Blast Loaded Reinforced Concrete Slabs." *World Journal of Engineering and Technology*, 02(04), 260–268.

Kang, S., Wu, Y. C., and Ham, S. (2020). "Singular integral solutions of analytical surface wave model with internal crack." *Applied Sciences (Switzerland)*, 10(9).

Karathanasopoulos, N., Reda, H., and Ganghoffer, J. F. (2019). "The role of non-slender inner structural designs on the linear and non-linear wave propagation attributes of periodic, two-dimensional architectured materials." *Journal of Sound and Vibration*, Elsevier Ltd, 455, 312–323.

Kee, S.-H., and Gucunski, N. (2016). "Interpretation of flexural vibration modes from impact-echo testing." *Journal of Infrastructure Systems*, 22(3), 04016009.

Kee, S. H., Fernández-Gómez, E., and Zhu, J. (2011). "Evaluating surface-breaking cracks in concrete using air-coupled sensors." *ACI Materials Journal*, 108(5), 558–565.

Kee, S. H., Lee, J. W., and Candelaria, M. D. (2020). "Evaluation of delamination in concrete by IE testing using multi-channel elastic wave data." *Sensors (Switzerland)*, 20(1).

Lapwood, E. R. (1949). “The Disturbance Due to a Line Source in a Semi-Infinite Elastic Medium.” *Philosophical Transactions of the Royal Society A: Mathematical, Physical and Engineering Sciences*, 242(841), 63–100.

Larsen, J. L., McElderry, J., Baxter, J. S., Guthrie, W. S., and Mazzeo, B. A. (2020). “Automated sounding for concrete bridge deck inspection through a multi-channel, continuously moving platform.” *NDT and E International*, Elsevier Ltd, 109, 102177.

Leissa, A. W. (1973). “The free vibration of rectangular plates.” *Journal of sound and vibration*, 31(3), 257–293.

Li, H., Pan, Q., Zhang, X., and An, Z. (2020). “An approach to size sub-wavelength surface crack measurements using Rayleigh waves based on laser ultrasounds.” *Sensors*, 20(5077).

Lou, X., Luo, R., and Yu, J. (2019). “Attenuation law of stress waves in cracked rock mass under different confining pressures.” *Advances in Civil Engineering*, 2019.

Mazzeo, B. A., Patil, A. N., Hurd, R. C., Klis, J. M., Truscott, T. T., and Guthrie, W. S. (2014). “Air-coupled impact-echo delamination detection in concrete using spheres of ice for excitation.” *Journal of Nondestructive Evaluation*, 33(3), 317–326.

Medak, M., Skazlic, M., Radic, J., Kucer, A., and Jambresic, M. (2019). “Assessment of cultural heritage using non destructive methods in view of material and structure properties.” *In International Conference Heritage protection-construction aspects: proceedings*, 95.

Mendelsohn, D. A., Achenbach, J. D., and Keer, L. M. (1980). “Scattering of elastic waves by a surface-breaking crack.” *Wave Motion*, 2(3), 277–292.

Miller, G. F., and Pursey, H. (1955). “On the partition of energy between elastic waves in a semi-infinite solid.” *Proc. Roy. Soc. A.*, 233(1192), 55–69.

Oh, T., Kee, S.-H., Arndt, R. W., Popovics, J. S., and Zhu, J. (2013). “Comparison of NDT methods for

assessment of a concrete bridge deck." *Journal of Engineering Mechanics*, 139(3), 305–314.

Oh, T., Popovics, J. S., Ham, S., and Shin, S. W. (2012). "Practical finite element based simulations of nondestructive evaluation methods for concrete." *Computers and Structures*, Elsevier Ltd, 98–99, 55–65.

Pao, Y. H., and Chen, W. Q. (2009). "Elastodynamic theory of framed structures and reverberation-ray matrix analysis." *Acta Mechanica*, 204(1–2), 61–79.

Park, Y., Abolmaali, A., Attiogbe, E., and Lee, S.-H. (2014). "Time-Dependent Behavior of Synthetic Fiber-Reinforced Concrete Pipes Under Long-Term Sustained Loading." *Transportation Research Record: Journal of the Transportation Research Board*, 2407, 71–79.

Pashoutani, S., and Zhu, J. (2020). "Ground penetrating radar data processing for concrete bridge deck evaluation." *Journal of Bridge Engineering*, 25(7), 1–20.

Popovics, J. S., Song, W. J., Ghandehari, M. Subramaniam, K. V. Achenbach, J. D., and Shah, S. P. (2000). "Application of surface wave transmission measurements for crack depth determination in concrete." *Materials Journal*, 92(2), 127–135.

Reda, H., Karathanasopoulos, N., Ganghoffer, J. F., and Lakiss, H. (2018). "Wave propagation characteristics of periodic structures accounting for the effect of their higher order inner material kinematics." *Journal of Sound and Vibration*, Elsevier Ltd, 431, 265–275.

Robison, T. W., Barnes, C. L., Tinkey, Y., and Tanner, J. E. (2020). "Evaluating concrete damage in bridge decks with and without overlays using nondestructive testing procedures." *Journal of Testing and Evaluation*, 48(1), 352–367.

Sansalone, M. J., and Streett, W. B. (1997). *Impact-echo: Nondestructive evaluation of concrete and masonry*. Bullblier Press, Jersey Shore, PA.

Scherr, J. F., and Grosse, C. U. (2020). "Delamination detection on a concrete bridge deck using impact

echo scanning." *Structural Concrete*, 1–7.

Schmerr, L. W. (2001). "Nondestructive testing | Ultrasonic." *Encyclopedia of Vibration*, 906–918.

Sun, H., Pashoutani, S., and Zhu, J. (2018a). "Nondestructive evaluation of concrete bridge decks with automated acoustic scanning system and ground penetrating radar." *Sensors (Switzerland)*, 18(6).

Sun, H., Zhu, J., and Ham, S. (2018b). "Automated acoustic scanning system for delamination detection in concrete bridge decks." *Journal of bri*, 23(6), 1–9.

Tsai, Y.-C. (James), and Chatterjee, A. (2018). "Pothole detection and classification using 3D technology and watershed method." *Journal of Computing in Civil Engineering*, 32(2), 04017078.

Visscher, W. M. (1985). "Elastic wave scattering by a surface-breaking or subsurface planar crack. II. Three-dimensional geometry." *Journal of Applied Physics*, 57(5), 1538–1550.

Wang, G., Tse, P. W., and Yuan, M. (2018). "Automatic internal crack detection from a sequence of infrared images with a triple-threshold Canny edge detector." *Measurement Science and Technology*, IOP Publishing, 29(2).

Wang, X., Shen, S., Huang, H., and Zhang, Z. (2020). "Quantitative assessment of the pavement modulus and surface crack using the Rayleigh wave dispersion curve." *Transportation Research Record*, 2674(5), 259–269.

Wickham, G. R. (1977). "The forced two dimensional oscillations of a rigid strip in smooth contact with a semi—infinite elastic solid." *Mathematical Proceedings of the Cambridge Philosophical Society*, 81(2), 291–311.

Xia, J., Miller, R. D., Park, C. B., Ivanov, J., Tian, G., and Chen, C. (2004). "Utilization of high-frequency Rayleigh waves in near-surface geophysics." *The Leading Edge*, 23(8), 753–759.

Zhu, J., and Popovics, J. S. (2005). "Non-contact imaging for surface-opening cracks in concrete with air-coupled sensors." *Materials and Structures/Materiaux et Constructions*, 38(283), 801–806.

Zhu, J., Popovics, J. S., and Schubert, F. (2004). “Leaky Rayleigh and Scholte waves at the fluid–solid interface subjected to transient point loading.” *The Journal of the Acoustical Society of America*, 116(4), 2101–2110.

Zhu, Z., and Popovics, J. S. (2007). “Imaging concrete structures using air-coupled impact-echo.” *J. Eng. Mech.*, 133(6), 628–640.